UNIVERSIDAD DE GRANADA

DEPARTAMENTO DE FÍSICA TEÓRICA Y DEL COSMOS
PROGRAMA OFICIAL DE POSGRADO EN FÍSICA Y MATEMÁTICAS

TESIS DOCTORAL
Octubre 2013

Nuevos Métodos Observacionales de Estrellas Post-AGB y Nebulosas Planetarias

[PhD THESIS]

Mónica W. Blanco Cárdenas
Instituto de Astrofísica de Andalucía - CSIC

Memoria de Tesis
presentada en la Universidad de Granada
para optar al grado de DOCTORA EN FÍSICA

Directores de tesis:
MARTÍN A. GUERRERO RONCEL
LUIS F. MIRANDA PALACIOS

.

El mejor guerrero no es el que triunfa siempre,
sino el que vuelve sin miedo a la batalla.
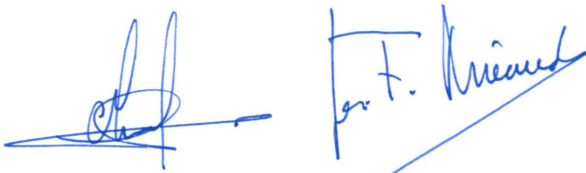
- Dolores Ibarruri -

Derechos de autor

El doctorando Mónica W. Blanco Cárdenas y los directores de la tesis Martín A. Guerrero Roncel y Luis Felipe Miranda Palacios, garantizamos, al firmar esta tesis doctoral, que el trabajo ha sido realizado por el doctorando bajo la dirección de los directores de la tesis y, hasta donde nuestro conocimiento alcanza, en la realización del trabajo se han respetado los derechos de los autores al ser citados, cuando se han utilizado sus resultados o publicaciones.

Granada, a 1 de octubre de 2013

Directores de la tesis

Doctorando

Fdo.: Martín A. Guerrero Roncel
Luis Felipe Miranda Palacios

Fdo.: Mónica W. Blanco Cárdenas

MARTÍN A. GUERRERO RONCEL, Investigador Científico del Instituto de Astrofísica de Andalucía, Consejo Superior de Investigaciones Científicas, y

LUIS FELIPE MIRANDA PALACIOS, Cientifico Titular del Instituto de Astrofísica de Andalucía, Consejo Superior de Investigaciones Científicas,

CERTIFICAN:

Que la presente tesis: *Nuevos Métodos Observacionales de Estrellas Post-AGB y Nebulosas Planetarias* ha sido realizada en el Instituto de Astrofísica de Andalucía, Consejo Superior de Investigaciones Científicas, por Mónica W. Blanco Cárdenas bajo nuestra dirección y constituye su Tesis Doctoral para optar al grado de Doctora en Física y Matemáticas.
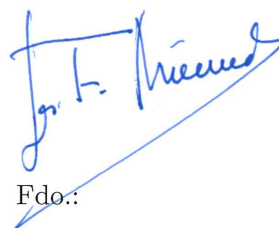
Granada, 1 de octubre de 2013

Martín A. Guerrero Roncel

Fdo.:

Luis Felipe Miranda Palacios

Fdo.:

.

- Y cada uno en su camino va cantando, ahuyentando sus penas.
Y cada cual en su destino va llenando de soles sus venas.

- en *Semilla en la tierra*, Carlos Chaouen -

.

A mis padres, por todo su amor y su apoyo.
A Jesus A. Castañeda, que dejó este
mundo pero se ha quedado en mi memoria.
Gracias por haber existido, Chuy.

Agradecimientos

Aunque resulte curioso, debo reconocer que escribir estas páginas era lo que más me motivaba a escribir la tesis, pues sabía que serían escritas poco antes de dar por finalizada la escritura de esta tesis que se desarrollo paralelamente a esta maravillosa experiencia de haber vivido en Granada para hacer el doctorado.

Hay tanto que agradecer que tengo temor de omitir a alguien, pues esta historia ha estado sembrada con tantas semillas de personas provenientes de múltiples historias y que han dejado en mi un trocito de su ser. He de comenzar con el profundo agradecimiento a mis padres que siempre han creido y confiado a en mi, a pesar de mis extravagancias y locuras. No podría estar más agradecida por haber tenido la fortuna de tenerlos como padres, por haberme enseñado a luchar cuando parecía que todo estaba perdido. Me lo enseñeron con su ejemplo, y con ese mismo ejemplo me ayudaron a hacer crecer las alas con las que he tenido el valor de iniciar la búsqueda de mis inquietudes. Mil gracias por todo su amor, por su cariño y por haberme enseñado a ser fuerte. A mis hermanos porque cada uno, a su manera, me ha demostrado su amor y su respeto, gracias por estar ahí para ayudarme como cada uno ha podido, con sus locuras, con sus risas, con sus consejos. Gracias, mis queridos "Gusana" y "Vinny", ustedes también están siempre a mi lado.

Es triste tener que escribir un agradecimiento a alguien que ya no puede leerlo. ¿Y ahora cómo puedo hacerte saber, Chuy, que te voy a echar de menos, que ya te echo de menos, que me hacen falta tus abominables comentarios y esos trozos que me compartías de tu compleja mente? De dónde saco un nuevo *troll* con tu peculiar forma de ver el mundo. Ya no estás, no sé si algún día volveré a verte, a escucharte, a reirme de tus tonterías. Espero que mientras estabas vivo haya podido demostrarte que eras importante para mi, que apreciaba tu opinión ya que nunca pensé que al regresar a México no estarías más entre nosotros. Gracias por todo, Chuy.

A querido profesor Roberto Vázquez Meza. Siempre apoyándome, siempre creyendo en mi, ayudándome a disipar la dureza con la que juzgo todos mis errores académicos. Gracias también por ese último esfuerzo que hiciste para ayudarme a llegar a Granada, sin ti, está historia probablemente no se habría podido escribir.

Mi mama siempre me dice que en sus oraciones por mi le pide a Dios que me cuide y que ponga ángeles en mi camindo que, ciertamente, como el de tantos becarios y posdocs, está a ratos inmerso en soledad. Yo no sé mucho de esas cosas, no soy realmente una persona religiosa, pero de alguna manera sé que las oraciones de mi madre han surtido efecto. Gracias a mis queridos Clara Cortijo Ferrero, Yoli Jiménez Teja, Vania Zanetti y Reinhard-Caos-Larcher, cada uno más diferente que el otro, con sus propias movidas y sus visiones tan particulares del mundo. Gracias a ti, mi Clarita, "la Schunga", por todo el cariño que me has hecho sentir, por haber estado a mi lado en momentos difíciles para mi, por

haberme escuchado y por haberme regalado aquel día de los zapatos guay el combustible para seguir adelante cuando más mal y perdida me sentía. Espero, mi bonita, que en tus momentos más difíciles tengas la bendición que yo he tenido al tenerte a mi lado. Te quiero muchísimo y un pedazo de ti se va conmigo a dondequiera que yo vaya (será un trozo de pierna, para que la personificación de la coja te quede a la perfección, ja ja). A ti, "Scholi", que con tu caracter tan amable y dulce también supiste apoyarme cuando estuve a punto de derrumbarme, por todos los momentos que hemos compartido entre risas y cotilleos, y por compartirme tu forma de pensar y ayudarme con ello a ver las cosas desde otro punto de vista. Gracias por todo, mi Scholi, te deseo lo mejor. A mi querida Vania "la pipistrella", la loca desquiciada más tierna que he conocido, por que tu me has ayudado a liberar buena parte de mis tonterias y juntas hemos recorrido la ruta de la muerte (y otras rutas) no sé cuantas veces. Loca, ven a verme pronto, yo te prometo que ese viaje a Italia sigue pendiente y voy a intentar que nos pongamos una buena borrachera en tu tierra y espero que en la mia también. A mi querido loco perdido "Caos", que con su llegada a mi vida me regresó el caos que había perdido. Tú no me crees, Reino, pero no me voy a cansar de repetirte que haberte conocido es una de las mejores cosas que me han pasado en mi vida y que siempre viajarás en un trocito de mi corazón, espero verte en algún otro lugar para hacer tonterias y reir como tontos, como tantas veces reimos. Gracias a estos 4 ángeles por haber estado a mi lado, gracias a la vida por haber cruzado sus trayectorias con la mia en Granada.

A esos amigos que me han acompañado durante estos 5 años aunque miles de kilometros nos separaran. Gracias Mónica "Gotita" Johnson, Pamela Meza, Patricia Arreola, Fermin Franco, Ramón Carrillo, Gerardo "El Dark", Luis Burgos, Manuel Sánchez, Heber Huizar "Pikito de poio", Laura Ocegueda. Nos vemos muy muy pronto para seguir escribiendo historias juntos, ¡eso espero!

Y Granada sigue llena de personas que me han apoyado y que han hecho de mi vida una experiencia fabulosa. Mi "baby William", engendro del demonio, gracias tambien por escucharme y por apoyarme, por ser tan sincero y decirme que dejara de complicarme la vida y mandara aquello que me dolía a dar una vuelta. A Joel Sánchez, por creer en mi, por su apoyo y porque, a pesar de todo, sé que de alguna manera estás aquí, con tu amistad y tu forma tan generosa de ser. Cree más en ti, loquillo, y ya lo sabes, te deseo lo mejor en esta vida. A Diana "Carito" por acompañarme aunque sea de vez en cuando en este viaje, por tu amistad y las conversaciones que hemos tenido. Cuidate mucho, mi Carito. También he de agradecer a esas personas que estuvieron involucradas en historias contrastantes, llenas de de alegría, de tristeza y cosas raras. A Rodo Torres, que aunque nuestra historia terminó de una manera abrupta e inesperada, nunca olvidaré aquellos años en los que fuimos amigos y estuviste ahí para ayudarme, para apoyarme, para hacerme reir y pasar un buen rato. A Monika Zielinska, arMonikita, que juntas vivimos meses tan extraños y tan contrastantes. Sé que ahora estás mejor y me da mucho gusto, espero que esa alegría te acompañe por mucho tiempo.

A toda la gente que ha compartido momentos conmigo en los que me lo he pasado genial. Nelleke, loca, gracias por compartirme tu peculiar forma de ver el mundo, siempre me señalas un camino o un concepto del cual no había meditado mucho o me das una nueva perspectiva. Pablo Santos, tan amable y tan "majo", ¡cuídate mucho, escuincle del demonio! A Ana González Soleto, por estar siempre con

"A mi modo he dado todo lo que soy" −en *Ahora*, E. Búnbury

Resumen

Las nebulosas planetarias (PNe del inglés "planetary nebulae") son la fase evolutiva posterior a las estrellas en la Rama Asintótica de las Gigantes (Asymptotic Giant Branch) con masas iniciales bajas e intermedias ($0.8M_\odot < M_i < 8M_\odot$). Uno de los aspectos más espectaculares y controvertidos de las PNe es su gran variedad de morfologías, como han mostrado en los últimos años observaciones obtenidas con la nueva generación de telescopios, p.e. *Hubble Space Telescope (HST), Very Large Telescope (VLT), Very Large Array (VLA)*, entre otros. Las PNe presentan morfologías que van desde las esféricas hasta las que presentan lóbulos bipolares (o multipolares) y estructuras compactas con simetría puntual, muchas veces con altas velocidades que llegan hasta los 600 km s^{-1}. Se ha estimado que aproximadamente el 80 % de las PNe no son esféricas, un resultado impactante ya que las PNe se forman a partir de la envoltura esférica eyectada durante la fase AGB y posteriormente ionizada por fotones UV producidos por la estrella central.

El mecanismo de formación de tan complejas estructuras es objeto de intenso debate. Las envolturas de las estrellas AGB presentan las primeras asimetrías en las etapas tardías de la fase AGB, así como en la fase post-AGB, de tal manera que cuando se ha formado una proto-PN frecuentemente ya presenta una morfología bipolar o multipolar, como es el caso de la proto-PN axialmente simétrica AFGL 915 (*"The Red Rectangle"*) o las PNe jóvenes M2-9 (*"The Butterfly Nebula"*) y Mz 3 (*"The Ant Nebula"*). Los escenarios propuestos capaces de esculpir dichas morfologías incluyen discos o estructuras toroidalesen en la zona equatorial de las PNe y flujos colimados con altas velocidades, los cuales no pueden ser generados únicamente por la presión de radiación estelar. La definición y caracterización clara y precisa del mecanismo de formación de las PNe más complejas requiere observaciones con la mayor resolución angular y espectral posible en las zonas centrales de fuentes post-AGB, proto-PNe y PNe jóvenes que, en general, están obscurecidas por polvo y no son detectables en el rango espectral óptico, pero sí en longitudes de onda infrarrojas y radio.

Esta tesis doctoral tiene como objetivo hacer uso de técnicas observacionales de alta resolución espacial utilizando telescopios de última generación, como es el caso del VLT de 8.2 m, para observar en el infrarrojo estrellas post-AGB, proto-PNe y PNe y obtener información sobre las regiones más internas de estos objetos. Basándonos en estudios previos, se han seleccionado diferentes muestras de objetos compactos en transición a PN o PNe jóvenes en los cuáles la falta de resolución no había permitido investigar las características morfológicas de las zonas centrales en las cuales subyace el mecanismo de formación. También se han seleccionado objetos representativos de PNe axialmente simétricas, los cuales cuentan con más información concerniente al mecanismo central que colima y esculpe sus morfologías. Ello permitirá hacer un análisis comparativo y probar la eficacia de una técnica basada en el análisis de espectros de alta resolución aplicada a la búsqueda de discos en las regiones centrales de PNe extremadamente asimétricas.

Dadas las características de las fases evolutivas de las estrellas concernientes a esta tesis, además del uso de instrumentos capaces de resolver estructuras compactas, éstos también deben ser capaces de observar estructuras que generalmente se encuentran inmersas en polvo, ya que las estrellas post-AGB se consideran las mayores productoras de polvo del medio interestelar. Así mismo, el polvo favorece la aparición de moléculas que emiten sobre todo en longitudes de onda infrarrojas y radio.

Motivados por lo expuesto anteriormente, se ha solicitado y obtenido tiempo de observación con los instrumentos VISIR (VLT *Imager and Spectrometer for the mid-IR*) y CRIRES (*Cryogenic high-resolution Infra-Red Echelle Spectrograph*). Se ha procedido a preparar las observaciones y, una vez adquiridos los datos, se han procesado y analizado.

Los objetos post-AGB más obscurecidos por el polvo pudieran estar sistemáticamente fuera de los criterios de selección de aquellos estudios previos que han detectado estructuras axialmente simétricas en PNe jóvenes. Considerando que dichos objetos post-AGB más obscurecidos probablemente descienden de progenitores de PNe más masivos, éstos deberían exhibir morfologías asimétricas. Observaciones a alta resolución de éste tipo de fuentes deberían ser capaces de revelar morfologías bipolares para corroborar la relación que existe entre progenitores masivos y la morfología de las PNe. Por ello, se han observado con VISIR-VLT cuatro candidatos a objetos post-AGB obscurecidos en el óptico cuya emisión extensa no había podido ser resuelta por el telescopio espacial infrarrojo *Spitzer* IRAC (*InfraRed Array Camera*). Ésto con el fin de estudiar con alta resolución angular en el infrarrojo medio (de 8 a 25 μm) las características morfológicas de los cuatro candidatos a post-AGB IRAS 15534−5422, IRAS 17009−4154, IRAS 18229−1127 e IRAS 18454+0001. Las imágenes han sido deconvolucionadas y calibradas en flujo y con ellas se han elaborado mapas de temperatura y profundidad óptica para estudiar la distribución espacial de las condiciones físicas de dichos objetos en longitudes de onda del infrarrojo medio. Se ha conseguido resolver la emisión extensa detectada por *Spitzer* IRAC resultando en la detección de asimetrías que han sido considerablemente enfatizadas en los mapas de temperatura y profundidad óptica en tres de los cuatro objetos. En en caso de IRAS 15534−5422, IRAS 17009−4154 e IRAS 18454+0001 estas asimetrías pudieran estar asociadas con estructuras toroidales compuestas por polvo así como con estructuras ligeramente bipolares. Mientras que la fuente post-AGB IRAS 18229−1127 presenta una envoltura romboidal. Se ha conseguido catalogar a los objetos IRAS 15534−5422, IRAS 17009−4154 e IRAS 18454+0001 como PNe jóvenes que parecen encontrarse en fases iniciales de asimetrías. Sin embargo, estas cuatro fuentes obscurecidas estudiadas con VISIR-VLT no presentan asimetrías marcadas, como es esperado para progenitores masivos según los resultados obtenidos para los estudios realizados en objetos post-AGB brillantes. Estas fuentes obscurecidas estudiadas con VISIR-VLT pudieran ser representativas de fases tempranas en la evolución de PNe que descienden de progenitores masivos, antes de que las asimetrías extremas sean desarrolladas.

Por otra parte, se ha estudiado la morfología en el infrarrojo cercano y medio de la PN K 3-35. Esta PN es extremadamente joven y forma parte de las pocas PNe que presentan emisión de máseres

de agua. K 3-35 es una PN bipolar que ha sido esculpida por un jet bipolar en precesión presuntamente colimado por un disco no alineado con el eje mayor de este objeto que, a su vez, está relacionado con un anillo compacto ($\sim$60 AU) y magnetizado de máseres de agua detectado en sus regiones centrales. Sus características morfológicas en el óptico son considerablemente diferentes a su morfología en radio. Este estudio se ha basado en la obtención de imágenes VISIR en la banda N (de 8 a 13 μm), el uso de imágenes de banda ancha en el infrarrojo cercano (bandas J,H y K), así como imágenes de banda estrecha en los filtros de la banda K que detectan la emisión de las líneas de Brγ y H$_2$. Adicionalmente, se ha hecho uso del espectro *ISO (Infrared Space Observatory)* para poder investigar la naturaleza de la emisión de K 3-35 en el IR medio. Como resultado, se ha podido hacer una comparación de las características morfológicas de esta peculiar PN. La morfología detectada en longitudes de onda en el infrarrojo medio se corresponde con la observada en el óptico, es decir, la estructura bipolar de K 3-35 es la que domina esta emisión, tanto para las bandas J, H y K , como para Brγ y H$_2$. Sin embargo, hemos detectado la primera evidencia de emisión débil de la región central de K 3-35 en la banda K. En cambio, la morfología en el infrarrojo medio está dominada por la región central de K 3-35, al igual que radio-contínuo. Además de la emisión central, hemos encontrado una correspondencia entre la emisión del jet en precesión en la banda infrarroja N y las longitudes de onda en radio-contínuo, siendo prácticamente idénticas. Lo anterior nos ha permitido deducir que la emisión central de K 3-35 se debe a gas ionizado envuelto por una envoltura de polvo que pudiera proteger y favorecer la existencia de moleculas de agua en esta PN. Respecto al jet, es muy probable que se trate de material ionizado con una pequeña contribución de polvo, tal como se ha podido inferir de la emisión detectada en el filtro ancho a 11.25 μm. Nuestros datos también sugieren que la emisión de H$_2$ es excitada por choques supersónicos en los lóbulos bipolares de K 3-35.

Respecto a los estudios espectroscópicos presentados en esta tesis, hemos utilizado y analizado espectros de alta-resolución de tiempo de prueba de CRIRES-VLT. Estos datos han sido usados para investigar la implementación de la técnica observacional conocida como espectro-astrometría de alta resolución, técnica no utilizada anteriormente en esta área de estudio. El uso de esta técnica ha sido motivado por las limitaciones de las técnicas interferométricas infrarrojas en el estudio de las asimetrías de PNe. Por sus características, se escogieron los objetos IRAS 17516-252 y SwSt1, una proto-PN y una PN joven, para desarrollar la metodología y las herramientas de procesamiento y análisis de los datos espectroscópicos que conducen a un análisis espectro-astrométrico. Para ambos objetos, sus características morfológicas no han podido ser del todo resueltas en previos estudios. Después del análisis espectro-astrométrico, hemos encontrado evidencias que sugieren la presencia de un disco detectado en Brγ y lóbulos bipolares detectados en la línea [Fe III] en SwSt 1 con tamaños de entre 130 mas y 230 mas, mientras que para la proto-PN IRAS 17516$-$2525, el análisis espectro-astrométrico sugiere la presencia de un par de lóbulos bipolares de $\sim$12 mas originándose en el centro de este objeto.

Los datos de alta resolución obtenidos específicamente para realizar el estudio espectro-astrométrico han sido cuidadosamente planeados con el fin de realizar el análisis que nos permita probar la eficacia de dichas observaciones para la búsqueda de discos y otras estructuras compactas en PNe extremadamente asimétricas. La muestra ha sido seleccionada considerando las observaciones que han

demostrado la existencia de discos y la química de los objetos. En esta tesis presentamos los resultados preliminares del estudio espectro-astrométrico realizado para la proto-PN AFGL 915. Esta proto-PN, con una química mixta de C-O, ha representado un reto observacional desde su descubrimiento debido a su peculiar aspecto que recuerda a un rectángulo. Mediante estudios espectroscópicos ha sido posible la detección de un disco masivo compuesto por cristales de silicio, mientras que estudios interferométricos han detectado la presencia de un disco Kepleriano de gas molecular (CO) en AFGL 915. Hemos obtenido observaciones de AFGL 915 utilizando CRIRES-VLT en el infrarrojo cercano de la banda fundamental a 4.99 μm de CO. Nuestro análisis espectro-astrométrico ha revelado los siguientes resultados preliminares. Las señales espectro-astrométricas detectadas son probablemente Keplerianas, así como los perfiles espectrales de la línea de $^{12}C^{16}O$ (λ4.99 μm). Así mismo, la presencia de un disco que se asemeja a un toroide orientado a 101°, el eje menor de esta PN, ha sido trazado por dicho análisis. Estos resultados preliminares están en concordancia con el disco de monóxido de carbono encontrado en longitudes de onda de radio pero, sobre todo, con un modelo que se ha realizado para explicar la morfología de AFGL 915, en el cual un sistema binario cercano experimentando una fase de envoltura común entre ambas componentes estelares da origen a un disco considerablemente grueso, masivo y probablemente acretando material. Finalmente, debemos hacer énfasis en que estos resultados deben ser corroborados ajustando un modelo apropiado a los resultados observacionales que hemos obtenido para esta proto-PNe.

Abstract

Planetary Nebulae (PNe) are the descendants of low- and intermediate-mass evolved stars ($0.8M_\odot < M_i < 8M_\odot$). Among the astrophysical phenomena, PNe display an impressive variety of complex morphologies, as has been demonstrated by observations obtained in the last years by the new generation of telescopes, e.g. *Hubble Space Telescope (HST), Very Large Telescope (VLT), Very Large Array (VLA).* PNe show morphologies from spherical to bipolar or multipolar, as well as knots and/or jets collimated at high velocities, reaching 600 $km\,s^{-1}$ in the most extreme cases. Furthermore, it has been estimated that nearly 80 % of the PNe are not spherical, a controversial result since PNe are formed from the spherical envelope ejected of an AGB (asymptotic giant branch) star and ionized afterwards by the UV photons produced by its central star.

The shaping of asymmetrical planetary nebulae (PNe) is yet under debate since these objects defy the standard models for the formation of spherical or elliptical PNe. The onset of the asymmetry of PNe is expected to occur during the short transition from the late asymptotic giant branch (AGB) and early post-AGB phase. Consequently, a proto-PN frequently displays a bipolar or multipolar morphology, like the proto-PN AFGL 915 ("The Red Rectangle") or the two young PNe M2-9 ("The Butterfly Nebula") and Mz 3 ("The Ant Nebula"). The existence of disks and/or torii in the equatorial regions and high velocity jets has been proposed to sculpt such morphologies in PNe, since the stellar radiation pressure is not able to collimate these extremely axisymmetric morphologies. The study of disks and jets as shaping agents of PNe requires the use of high-resolution observational techniques able to observe and resolve the innermost regions of post-AGB sources, proto-PNe, and young PNe. Furthermore, these innermost regions are often embedded in dust and are thus optically thick, nonetheless they emit copiously at infrared (IR) and radio wavelengths.

This PhD thesis aims to prove high-resolution observational techniques using new generation telescopes, as is the case of the 8.2 m VLT, to observe in the IR post-AGB, proto-PNe, and PNe at high-resolution. Based in previous studies, we have selected different samples of compact sources in transition to the PNe phase, as well as young PNe in which their innermost regions, where the shaping mechanism lays, were not resolved due to the lack of resolution. In addition, we have selected axisymmetric sources whose innermost zones have been observed and modeled. We aim to prove and compare previous results with the ones obtained using a spectroscopic high-resolution technique applied to the search of the shaping mechanism of extremely axisymmetric PNe.

Considering the characteristics of the evolved stars studied in this thesis, beside the use of powerful instruments capable to achieve high-resolutions, they must also be able to observe structures embedded in dusty environments, since post-AGB stars are important dust producers. These conditions also favour the apparition of molecules whose emission are mainly detected towards IR

and radio wavelengths.

Inspired by all these facts, we have requested and obtained observing time using two instruments of the VLT: VISIR (VLT Imager and Spectrometer for the mid-IR) and CRIRES (Cryogenic high-resolution Infra-Red Echelle Spectrograph). The results obtained with these observations are summarized in the following paragraphs.

Among all post-AGB objects, the most heavily obscured ones might have escaped the selection criteria of previous studies that detected extreme axisymmetric structures in young PNe. Since the most heavily obscured post-AGB sources can be expected to descend from the most massive PN progenitors, these should exhibit clear asymmetric morphologies. High-resolution observations of these sources should reveal marked bipolar morphologies, confirming the link between progenitor mass and nebular morphology. We have obtained VISIR-VLT mid-IR images of a sample of four heavily obscured post-AGB objects that are barely resolved in previous *Spitzer* IRAC observations in order to analyze their morphology and physical conditions across the mid-IR. The images obtained in four different mid-IR filters have been deconvolved, flux-calibrated, and used to construct RGB composite pictures as well as color (temperature) and optical depth maps that allow us to study the morphology and physical properties of the extended emission of the sources in our sample. We have detected the extended emission from the four objects in our sample and resolved it into several structural components that are greatly enhanced in the temperature and optical depth maps. The morphologies of the sample, as well as their physical conditions, reveal the presence of asymmetry in three young PNe (IRAS 15534−5422, IRAS 17009−4154, and IRAS 18454+0001), where the asymmetries can be associated with dusty torii and slightly bipolar outflows. The fourth source (IRAS 18229−1127), a possible post-AGB star, is better described as a rhomboidal detached shell. The heavily obscured sources in our sample do not show extreme axisymmetric morphologies. This is at odds with the expectation of highly asymmetrical morphologies in post-AGB sources descending from massive PN progenitors, which is otherwise supported by observations of bright mid-IR unobscured sources. The sources studied may be sampling critical early phases in the evolution of massive PN progenitors, before extreme asymmetries develop.

On the other hand, the young PN K 3-35 represents a unique case where a small-sized water maser ring has been linked to the launch of collimated outflows that would be shaping the nebula. The contrasting optical and radio continuum morphologies of K 3-35 indicate that they disclose different structural components which are apparently unconnected. To bridge the gap between optical and radio continuum observations, we present here new broad- and narrow-band near- and VISIR-VLT mid-IR images of K 3-35. These images, and their comparison with optical and radio continuum images, are revealing. The radio continuum and mid-IR images are dominated by a compact source at the core of K 3-35 whose emission gives evidence of very dense ionized material embedded within a dust cocoon. The emission from the core, obscured at optical wavelengths, is faintly detected in the K_s band. We suggest that the dust may shield the water molecules at the inner ring from the central star ionizing radiation. The precessing collimated outflows,

very prominent in radio continuum, are also detected in mid-IR, very particularly in the [S IV] image. The mid-IR emission from these outflows consists mostly of ionized material, although the broad-band filter at 11.85 μm seems to imply that a small amount of dust may be carried out by the outflow. The interactions of these outflows with the nebular shell result in shocks which excite the emission of H$_2$ and low-excitation lines from ionized species such as [N II] at the tips of the outflows.

Regarding the spectroscopic observations here presented, we have used and analysed high-resolution long-slit spectra from CRIRES-VLT commissioning time. These data have been used to investigate the implementation of the observational technique known as high-resolution spectro-astrometry, not used before in this research field. We have selected the spectro-astrometry technique motivated by the limitations of the IR interferometric techniques in the study of the asymmetries of PNe. High-resolution spectro-astrometry technique using CRIRES-VLT has proven its efficiency in the search for proto-planetary disks. CRIRES-VLT commissioning data of the proto-PN IRAS 17516−2525 and the young PN SwSt 1 have been used to develop the methodology and tools needed to apply the spectro-astrometric analysis to sources transiting towards or at early stages of the PN phase. Previous studies lacked the spatial resolution required to disclose the morphology of these two sources. Our exploratory study using CRIRES-VLT commissioning data has revealed small sized structures after the spectro-astrometric analysis of these two sources. The structures found in SwSt 1 have sizes of 230 mas in the [Fe III] line and 130 mas in the Brγ line. As for the proto-PN IRAS 17516−2525, the spectro-astrometric signal can be interpreted as compact bipolar lobes of 12 mas in size arising from the innermost regions.

In the second phase of the implementation of the spectro-astrometry technique we have obtained observations carefully planed aiming to prove the feasibility of this technique in the search of disks and other compact innermost structures in extremely axisymmetric PNe. We have selected the well studied proto-PN AFGL 915, from which past studies have provided strong evidences of a Keplerian gaseous CO disk as well as a disk of crystalline silicates aligned with its minor axis of symmetry. Based in the previous studies and in the C/O chemistry of this source, we have acquired CRIRES-VLT high-resolution spectra of the near-IR CO fundamental band at 4.99 μm. The spectro-astrometric analysis has revealed the following preliminary results. The spectro-astrometric signatures and the line profiles of the ^{12}C^{16}O (λ4.99 μm) resemble Keplerian sources. The presence of a thick torus-like orientated along the minor axis of symmetry, that is, at 101°, has been also disclosed by the spectro-astrometric analysis. These results are in concordance with previous observations representative for the outermost regions of the Keplerian disk and with models predicting the existence of this thick toroidal structure at the innermost regions of AFGL 915, whose origins are related with the common envelope binary system progenitor. It has been proposed that this thick innermost torus is massive and is accreting material. Finally, we emphasize that these results must be properly modeled in order to corroborate the properties of the disk found by our spectro-astrometric analysis at the central region of AFGL 915.

Index

LIST OF ACRONYMS AND ABBREVIATIONS

2MASS   Two Micron All Sky Survey

AGB   Asymptotic giant branch

AO   Adaptive optics

AU   Astronomical units

AGN   Active galactic nucleus

aPA   anti-parallel position angle

CE   Common envelope

CELs   Collisionally excited lines

Chopnod   Chopping and nodding

CRIRES   CRyogenic high-resolution Infra-Red Echelle Spectrograph

CS   Central Star

CSE   Circumstellar envelope

E-AGB   Early AGB

FoV   Field of view

FWHM   Full width at half maximum

GISW   Generalized interacting stellar winds

HSO   Herschel Space Observatory

HST   Herschel Space Telescope

IR   Infrared

IRAF   Image Reduction and Analysis Facility

IRAS   Infrared Astronomical Satellite

ISO   Infrared Space Observatory

mas   milliarcsecond

MASER   Microwave Amplification by Stimulated Emission of Radiation

MHD   Magneto-hydrodynamical

PA   Position angle

PAH   Polycyclic aromatic hydrocarbon

PdBI   Plateau de Bure Interferometer

PNe   Planetary nebulae

PSF   Point spread function

RGB   Red giant branch

RGB   Red green blue

RLs   Recombination lines

SA   Spectro-astrometry

SWS   Short Wavelength Spectrometer

TP-AGB   Thermal pulsating AGB

UT   Unit telescope

VLT   Very Large Telescope

VISIR   VLT Imager and Spectrometer for the mid-IR

WD   White Dwarf

WF   Wavefront

YSO   Young stellar object

1

Introduction

Among the astrophysical phenomena, planetary nebulae (PNe) are one of the most beautiful and impressive objects, due to the variety of perplexing morphologies produced by the "death" of low- and intermediate-mass stars. Since its discovery in 1974 by Charles Messier, as diffuse green disk-like sources resembling planets, until the last years, in which the modern observational techniques have allowed the sharp detection of multiple and complex shapes, many issues remain unsolved. PNe are the immediate descendants of asymptotic giant branch (AGB) stars, a stellar phase in which the major contributions of dust to the interstellar medium (ISM) is produced. To study the sculpting process of an asymmetric PN, it is necessary to move to infrared and radio wavelengths, since the observational evidences collected during the last decades have proven that dust an molecules trace structures as well as processes involved in the shaping of PNe during these late evolutionary phases. The PN phase starts when the progenitor star reaches an effective temperature of $\sim$30,000 K inducing emission of UV photons that ionize the circumstellar gas ejected during the late AGB and post-AGB phases. This ionization process allows us the detection of PNe in optical wavelengths. Furthermore, the use of high-resolution observational techniques is crucial in the study of the asymmetries in PNe. In this chapter we will discuss the main topics related with the origin and the shaping mechanisms of the sources that have been studied in this thesis and to define the characteristics of near- and mid-IR emission in post-AGB stars, proto-PNe and PNe.

1.1. The origin of planetary nebulae

Planetary nebulae are the descendants of low- and intermediate-mass stars (M_i=0.8–10 M$_\odot$). The shaping of the envelope of a PN occurs at some point between the late AGB and post-AGB phases. In the following lines we briefly describe the most important changes experienced by these stars on their way to become a PN.

The AGB phase begins afterwards the red giant branch (RGB) phase after a short stay in the horizontal branch. The AGB phase is characterized by short episodes of mass-loss occurring through
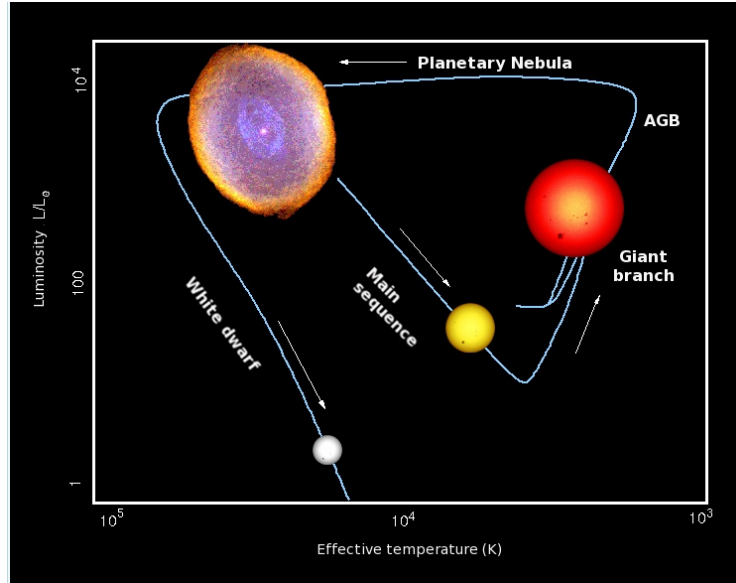
Figure 1.1 Hertzsprung-Russel diagram from the evolution of low- and intermediate- mass stars that will evolve as a PN.

a slow and dense wind ($v_{\mathrm{exp}} \sim 10$ km s^{-1}, $\dot{M} \sim 10^{-4} - 10^{-5}$ M$_\odot$ yr^{-1}). It is divided in two different stages: the early AGB (E-AGB) and the thermal pulsating stage (TP-AGB) . The E-AGB stage starts once the combustion of helium in the core has stopped whereas a degenerated C/O core remains inert. At this stage, the H and He combustion occurs alternatively in thin layers at the base of the outer H shell and the inner He shell, respectively. The He burning is the main source of energy during the E-AGB phase. When He reaches the critical mass its shell becomes unstable, since it produces more energy within its thin burning layer. This unstability leads to the TP-AGB stage, which is believed to be responsible for the mass-loss episodes and final fate of these stars. It is well known that most white dwarfs at the core of PNe have masses $\sim$0.6 $M_\odot$ (Weidemann 1990), but their main-sequence masses were $\gtrsim$1 $M_\odot$ (Pottasch 1984; Jura 1990), that is, a huge amount of mass is lost during the AGB phase. Normally, the PN envelope has $\sim$0.2 $M_\odot$. To gather this PN mass, the AGB progenitor star must have experienced mass-loss rates $\sim$3$\times$10$^{-5}M_\odot$yr^{-1} (Renzini 1981). Figure 1.2 shows the variations of the effective temperature, luminosity, pulsation period, the velocity of the wind, the mass of the star, and the mass-loss rate with time after the first major thermal pulse for a $1M_\odot$ with a helium abundance Y of 0.25 and a metal abundance Z of 0.008 (see Vassiliadis & Wood 1993).

The mass-loss experienced during the AGB phase sets the physical conditions to produce dust and molecules within the expelled circumstellar envelope (CSE, García-Hernández et al. 2003, 2006, 2012). At this time, maser emission of OH, H$_2$O, and SiO molecules arise. The distribution of each maser specie is determined by their excitation temperature, thus, OH masers are located at the outermost zones of the envelope, H$_2$O masers near to the dust forming region, and the SiO masers are located at the innermost regions (Figure 1.3). According with Lewis (1989), their lifetimes are directly related with these spatial distributions: 1000 yrs for OH, 100 yrs for H$_2$O and 10 yrs for the SiO masers. In addition to maser emission from molecules, large spherical shells of CO molecules
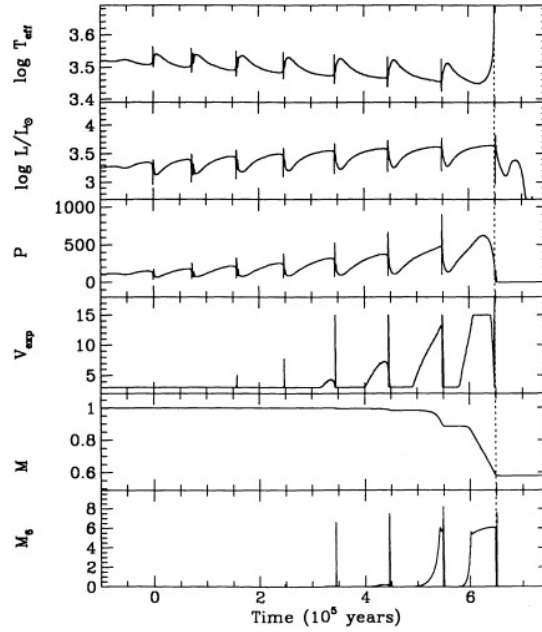
Figure 1.2 Variation of important quantities of a star of $1M_\odot$ facing the TP-AGB phase (Vassiliadis & Wood 1993)

have been found associated to the envelopes of AGB stars beyond the regions in which OH maser emission is found (Olofsson 2000). These shells are typically thin and clumpy, and extend farther from the AGB stars. One notorious case is that of the CO shell of TT Cygni with a radius $\sim 35''$ (Olofsson et al. 2000). The formation of these CO shells may be related with He-shell flashes. On the other hand, far-IR *HSO* (Herschel Space Observatory) observations have revealed non-concentric dust shells around IRC+10216, a C-rich AGB star (Decin et al. 2011). The first evidence of these structures was found in form of arcs (Mauron & Huggins 1999) and has denoted the necessity of re-examine the mass-loss during the AGB phase. The origin of these dust shells has been attributed to a non-isotropic mass-loss in a clumpy dust medium.

The AGB phase reaches its end once the C/O degenerated core remains exposed and surrounded by a detached CSE. In general, the post-AGB phase is characterized by a tenuous CSE that allows us the detection of the central star, except for the most massive stars, which confine the radiation of the central star in a dusty optically thick CSE (Schöenberner 1981; Vassiliadis & Wood 1993; Blöcker 1995). The mass-loss decreases during the post-AGB phase ($10^{-8} M_\odot$ yr^{-1}), whereas the stellar wind is faster than in the AGB phase ($1000 < v < 2000$ km s^{-1}). Simultaneously, the C/O degenerated core contracts and increases its effective temperature. When the effective temperature of the core reaches $\sim 30,000$ K, the increase in the flux of UV photons ionizes the circumstellar material and a new PN is born. Eventually, the expanding PN envelope (20 km s$^{-1} < v < 30$ km s^{-1}, Weinberger et al. 1989) will be diluted in the interstellar medium (ISM) and the only remnant of the beautiful life of these objects will be their white dwarf central star (Figure 1.1).
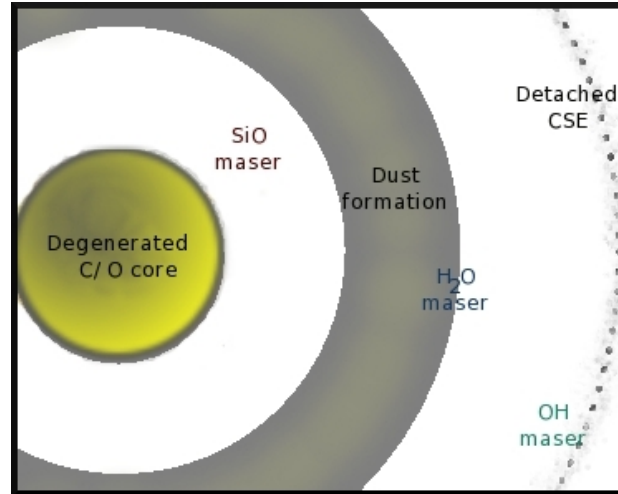
Figure 1.3 Sketch of the spatial distribution of the SiO, H_2O, and OH masers during the post-AGB phase.

1.2.   Shaping planetary nebulae: models and observational challenges

Planetary nebulae are fascinating objects that display several morphologies (Balick et al. 1987; Schwarz et al. 1992; Stanghellini et al. 1993; Corradi & Schwarz 1995; Manchado et al. 1996; Meixner 1997) from spherical to bipolar or multipolar lobes, highly collimated jets often accompanied by point symmetric structures (Figure 1.4, Miranda et al. 1999; Guerrero et al. 1999; Sahai 2000). The observations and studies carried out during the last decades have demonstrated that nearly 80 % of the PNe are asymmetric (Manchado 1997). This high occurrence of asymmetric PNe has established a new observational fact: spherical PNe are less common than asymmetric ones, which is an unexpected result since the RGB and early AGB stellar envelopes are spherical as revealed by the round CO and dust shells surrounding AGB stars.

1.2.1.   Observational evidences of asymmetry

One of the most remarkable signatures of asymmetry in PNe is the presence of collimated outflows (Figure 1.5). These outflows may appear like highly collimated hourglass bipolar lobes (also referred as butterfly morphology), narrow jets resembling the ones observed in Herbig-Haro (HH) objects, or compact low-ionization structures. For example, they can form compact knots and bow shocks resulting from the interaction of collimated outflows moving at supersonic velocities ($v \simeq 20$ km s^{-1}, Balick et al. 1994). Whilst the S-shaped jets, named as BRETs (Bipolar Rotating Episodic JeTs, Lopez et al. 1993; Lopez 1997; López et al. 2000), present remarkably high speeds, from $\simeq 160$ km s^{-1} in the case of M2-9 (Schwarz et al. 1997), 150-200 km s^{-1} for Hen 3-1475 (Riera et al. 2006) up to 500 km s^{-1} in Mz 3 or 630 km s^{-1} in MyCn18 (O'Connor et al. 2000).

With the discovery of these variety of high-velocity jets playing an important role in the shaping of
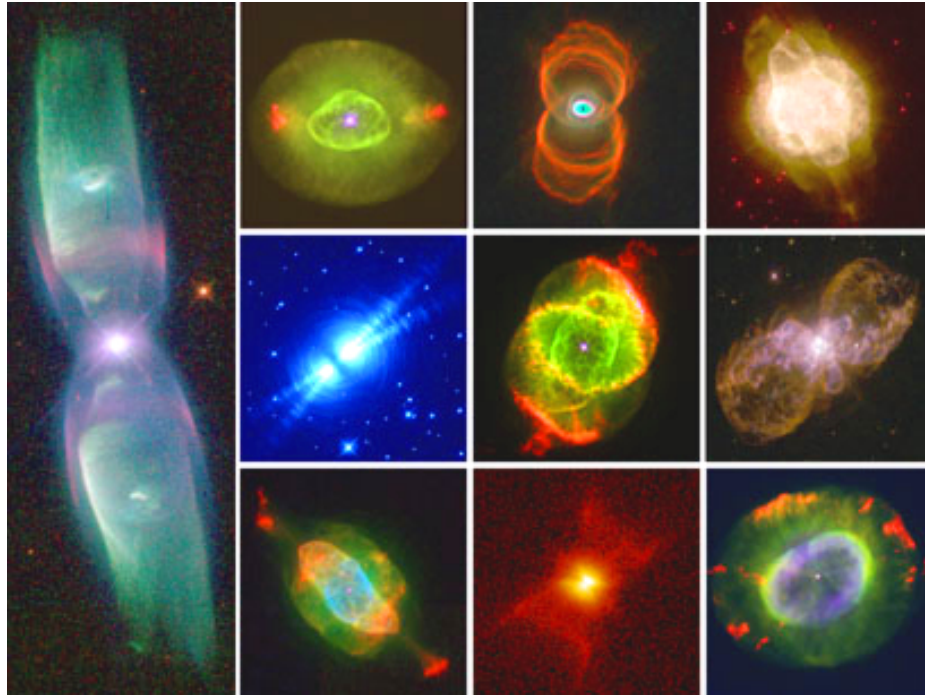
Figure 1.4 *HST* PNe mosaic of different PNe with different morphologies. Image credit: Bruce Balick, Howard Bond, R. Sahai, their collaborators, and NASA.

complex morphologies seen in several PNe questions on how and when they are formed arose. The first evidences of the onset of asymmetry in PNe were found in sources in their transition to PNe, between late AGB and early post-AGB phases (e.g. IRAS 09371-1212 and IRC+10216, Morris & Reipurth 1990; Beuzit et al. 1994; Kastner & Weintraub 1994; Roddier et al. 1995; Sahai 2002). These evidences and the characteristics of the sources in transition to PNe turn the infrared and radio wavelengths the spectral ranges that must be studied to achieve a better comprehension of how the PN asymmetries are sculpted. Concerning to the sizes of the innermost structures of sources in transition to PNe, their observations are proven to be crucial and extremely challenging, since they were not successfully resolved in several previous studies due to the lack of resolution. This fact confirms that the implementation of high-resolution (angular, spatial and/or spectral) observational techniques is absolutely necessary.

One of the most astonishing results regarding small-sized structures in PNe was revealed by radio observations that have detected a magnetized disk of water masers of $\simeq 65$ AU (40 mas) in size in the central region of the young PN K 3-35 (Miranda et al. 2001; Uscanga et al. 2008; Tafoya et al. 2011). Moreover, interferometric observations with Plateau the Bure (PdBI, IRAM) have resolved a Keplerian gaseous CO disk ($2''$ ~ 900 mas) in the proto-PN AFGL 915 (The Red Rectangle, Bujarrabal et al. 2005) and in 11 post-AGB objects (Bujarrabal et al. 2013). Another remarkably result revealed by PdBI (Castro-Carrizo et al. 2012), has been the discovery of two eccentric expanding rings (size≤ 5 $''$) located at the equator of M2-9 (The Butterfly Nebula). Moreover, they found strong evidences of a binary system in M2-9 and, concerning to the eccentric ring-like structures,

Figure 1.5 *HST* images of PNe illustrating different types of jets. From left to the right: NGC 3242 and its FLIERS (red knots), image credit: Bruce Balick, its collaborators and NASA; the Ant nebula (Mz 3), and its high velocity knots (v=500 km s^{-1}), image credit: NASA, ESA, and the Hubble Heritage team; proto-PN Hen 3-1475 and its "S-shaped" jets (a.k.a. BRETs), image credit: Angels Riera (Universitat Politecnica de Catalunya and ESA) and Pedro García Lario (ESA); proto-PN CRL 618 showing highly collimated jets. IC 4634 with its BRETs, image credit: ESA/Hubble and NASA.

they deduced that they were launched by two different mass-loss episodes that shape the complex morphology of this PN.

Meanwhile, observations in the near- and mid-IR have proven its capability in the search of incipient asymmetries and collimating agents in PNe. The search of the asymmetries in early phases of PNe has motivated surveys focused in the post-AGB and proto-PN phases. Meixner et al. (1999) have performed a survey of 66 proto-PNe candidates in the mid-IR, resulting in 1″ angular-resolution images of 17 sources that have been resolved at this resolution. From these 17 sources, 11 present extended emission and a fraction of them suggest equatorial density enhancements. On the other hand, Lagadec et al. (2011) presented a mid-IR imaging catalogue of post-AGB stars using two different mid-IR instruments and the results of the diffraction-limited images are outstanding: the 25 proto-PNe resolved seemed to have circular diffuse envelopes, indicating a departure from spherical symmetry, nevertheless, none of these proto-PNe exhibit spherical morphology. Most of these works focused on post-AGB sources characterized by optically thin detached CSE around these stars. Large samples of optically thick and heavily obscured post-AGB sources were studied with *Spitzer* (Ramos-Larios et al. 2009; Ramos-Larios et al. 2012). In these studies, they have found spherical and asymmetric morphologies for some of the objects that were resolved

Drastic morphological differences are also detected when optical and mid-IR morphologies are compared. For example, observations in the mid-IR with angular resolutions of 0″.6<FWHM<0″.9 of the proto-PNe AFGL 618, CRL 2688 and AFGL 915 are dominated by bright cores, whereas the near-IR morphologies are optical alike (Hora et al. 1996), that is, they are dominated by the bipolar lobes and the outermost morphological components. These mid-R bright cores, which are optically thick at near- and optical wavelengths support the hypothesis of dusty torus and/or disk as shaping mechanism. Another study in the mid-IR, but with higher-resolution ($\simeq$0″.35 at 8.8μm), has disclosed asymmetries traced by warm dust in AFGL 2688. And, in the case of the proto-PN IRAS 22272+5435, the 20.3 μm image traces a dusty equatorial torus (Morris & Sahai 1999). One impressive example of the role of the use of high-resolution techniques and the observation of asymmetries at early phases in sources that
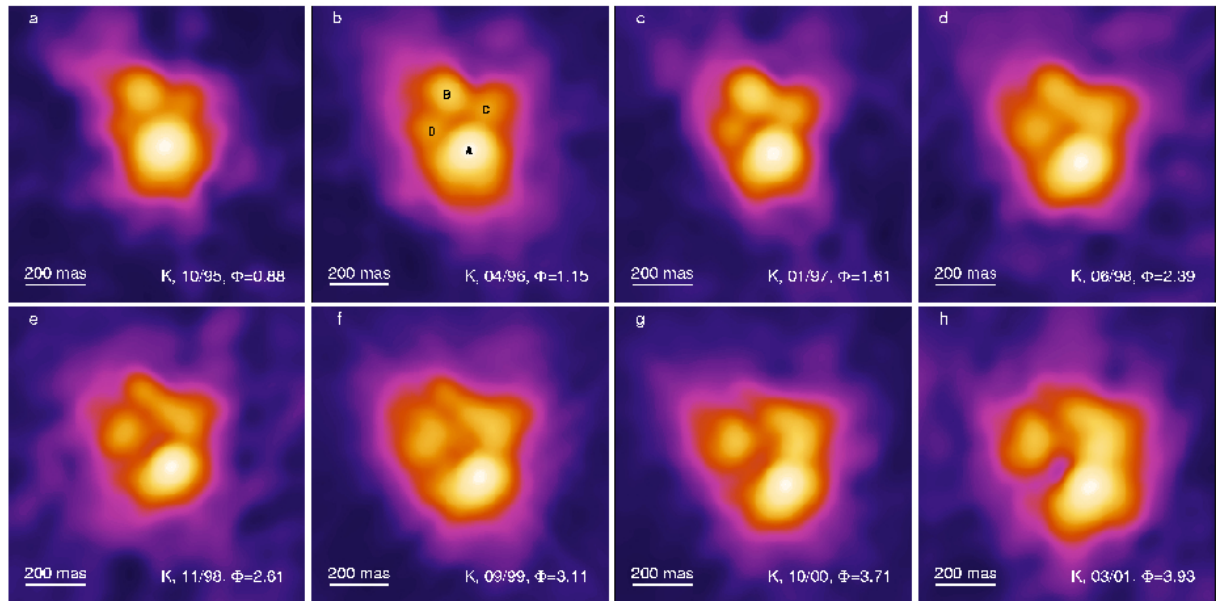
Figure 1.6 Bispectrum speckle interferometry in the near infrared K-band showing the morphological changes of the carbon star IRC+10216 along 6 years (Weigelt et al. 2002).

will evolve into PN is provided by Weigelt et al. (2012) who used bispectrum speckle interferometry in the near-IR with only one telescope to study the carbon star IRC+10216. These observations reveals the changes within 6 yrs in the aspherical morphology of this variable star evolving to the AGB phase (Figure 1.6). We note that the spatial resolution achieved in this study is of the order of few mas.

However, none of these infrared imaging studies has been able to disclose the collimating agent of asymmetric PNe, and just like in the radio studies, the use of powerful interferometers is required. VLTI (Very Large Telescope Interferometer) has the capability to resolve such structures using AMBER-VLTI (near-infrared/red focal instrument of the VLTI) and MIDI-VLTI (mid-infrared instrument of the VLT interferometer). Young and extremely axisymmetric PNe were studied with MIDI-VLTI: Mz 3, M2-9, CPD-56°8032, and M2-29 (Chesneau et al. 2007; Lykou et al. 2011; De Marco et al. 2002; Chesneau et al. 2006). In the case of Mz 3 and M2-9 (Chesneau et al. 2007; Lykou et al. 2011) the composition of the disks are amorphous silicate grains. As for the sizes of the disks, they are ∼30 AU and ∼15 AU, respectively. The size of the silicate disk in Mz 3 is too large to be the responsible of such highly collimated morphology, therefore, it has been suggested the existence of a smaller innermost gaseous disk. As for CPD-56°8032 and M2-29, the disks inner radii are ∼100 AU and have dual dust chemistry (O and C rich). For these four PNe, only M2-9 and M2-29 have a binary companion confirmed (Lykou et al. 2011; Corradi et al. 2011; Hajduk et al. 2008).
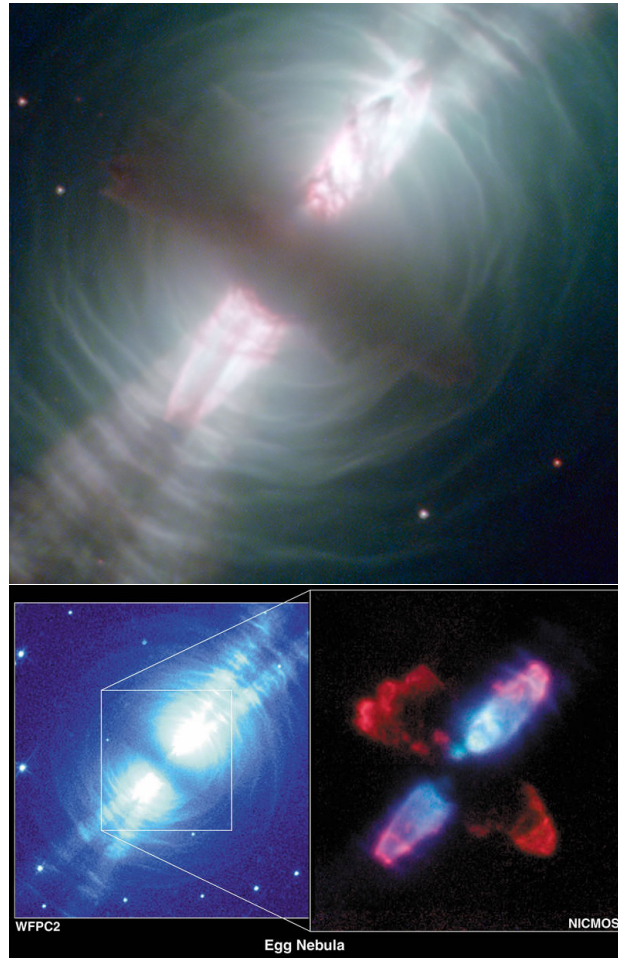
Figure 1.7 The "Egg nebula" (CRL 618) as seen by the *HST*. (*Upper*) The Egg nebula as seen in optical wavelengths is a proto-PN and this image perfectly illustrate the beauty and the complexity of this phase. Also, we note the presence of an equatorial dust cloud hiding the shaping mechanism of this source. Image credit: ESA, *HST*, and NASA. Bottom The image show the dramatic difference of the emission if we look toward IR, red is molecular hydrogen (CREDITS).
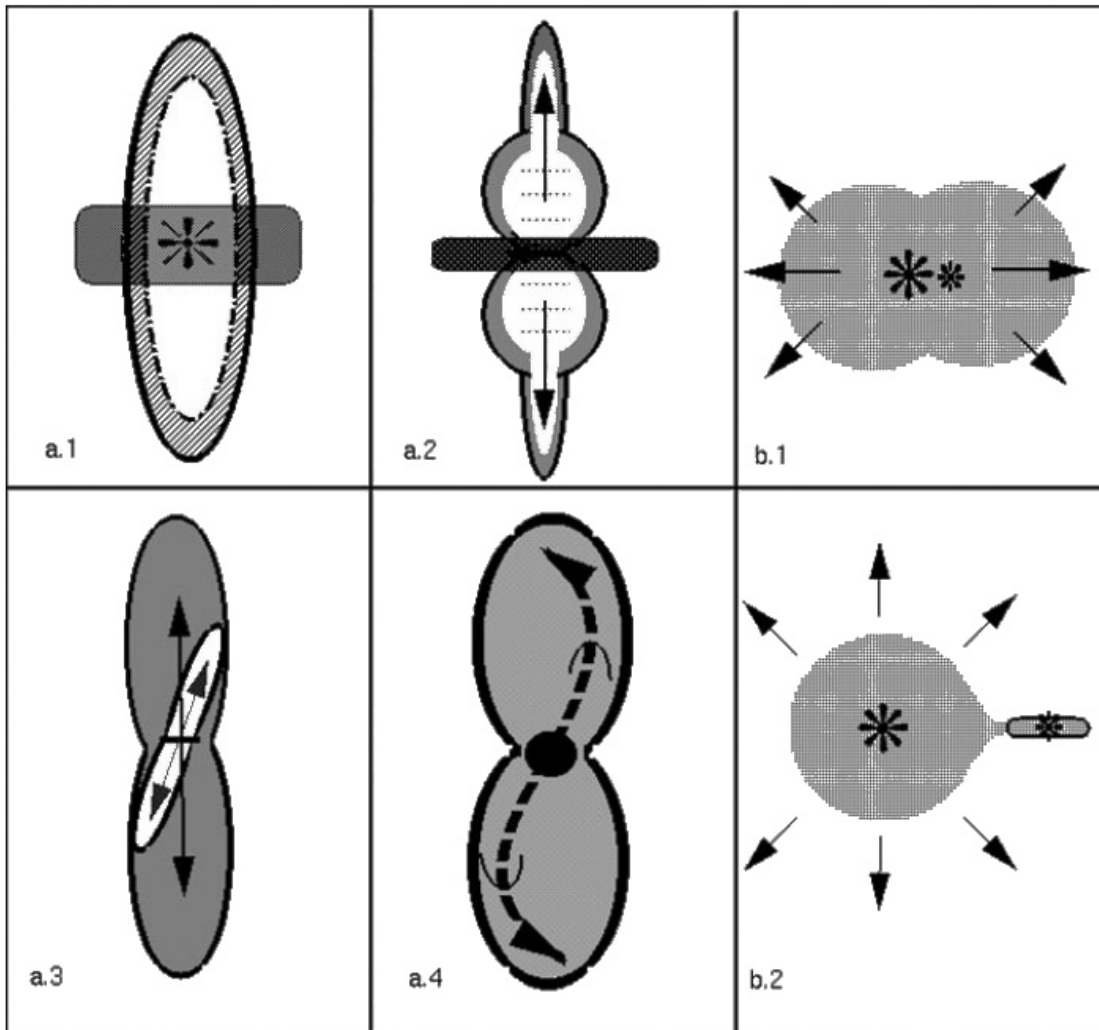
Figure 1.8 Sketch of possible proto-PNe and PNe shaping scenarios from different models. Adapted from Balick & Frank (2002). (a.1) GISW: toroidal slow wind mass-loss followed by isotropic fast wind (Balick et al. 1987; Icke et al. 1989; Mellema & Frank 1995). (a.2) Magnetized wind blow bubble (MWBB): effects of toroidal magnetic fields (García-Segura et al. 1999; García-Segura et al. 2005). (a.3) Magneto-hydrodynamic model of (Blackman et al. 2001b) based in binary disruption that produce a misaligned disk with enough accreting power to launch jets and shape a multipolar PN. (a.4) Scenario in which precessing jets are triggered originating a PNe with point symmetric features. As for (b.1) and (b.2) these schemes represents the two binary scenarios that can produce an accreting disk in this evolutionary phase: a common envelope phase in a system of two close binaries (Rasio & Livio 1996; Soker 1997; De Marco 2009) and an accreting disk formed via Roche lobe (Mastrodemos & Morris 1999).

1.2.2.   Models

The formation of spherical PNe is satisfactorily explained by the interacting stellar wind model (ISW, Kwok et al. 1978). In the ISW scenario, PNe are formed through the interaction between the remnant of the mass-loss that took place during the AGB phase (the slow and dense AGB wind) and the mass-loss of the post-AGB (the faster and less dense wind, also known as "fast wind"). Whilst, the generalized interacting stellar winds model (GISW, Balick et al. 1987; Icke et al. 1989; Mellema & Frank 1995) basically explains how an elliptical or slightly bipolar PNe (those PNe that are not extremely axisymmetric) are formed due to the interaction of the slow and the fast winds assuming an equatorial density enhancement in the remnant AGB wind. In this model, the bipolar lobes are sculpted by radiation pressure and highly pressurized hot gas, although the origin of the equatorial density enhancement is not explained and the formation of point symmetric features are not possible in this scenario.

Nevertheless, the most extreme axisymmetric PNe defy the GISW model. This fact has generated an intense debate in the search of possible scenarios in which the shaping of these complex morphologies is feasible. These scenarios include disks and fast collimated jets as basic components (Sahai & Trauger 1998). The observed high-velocity jets in proto-PNe and PNe require more energy and momentum than that supplied only by radiation pressure on dust grains (Bujarrabal et al. 2001), whereas the origin and characteristics of the disks and/or extended torii are not fully understood due the small number of observational data proving and constraining them. Despite of that, several efforts have been made in the last decades to observe, understand and to explain how such complex morphologies are triggered. In order to get a basic idea of the complexity of the transition to this phase in the evolution of low- and intermediate-mass stars with the most complex morphologies, in the following lines we briefly describe models of shaping scenarios that explain the formation of extremely axisymmetric PNe (Figure 1.8).

If we depart from the hypothesis of a single star as a progenitor of an axisymmetric PN, one plausible scenario is the magnetized wind blown bubble (MWBB, García-Segura et al. 1999; 2005) In this model, magnetically driven flows launch the torus and bipolar hourglass-like outflows if an initial magnetic field increases gradually its intensity during the post-AGB and proto-PN phases. Another scenario capable of triggering jets in a single progenitor involves an AGB star in which a strong magnetic field is induced through the dynamo effect. This is possible if the AGB core is rapidly rotating while its envelope is slowly rotating (Blackman et al. 2001a). On the other hand, binary systems as progenitors of these morphologically complex PNe have been explored and have opened new alternatives and observational challenges. The binary progenitor hypothesis reckons on disks as the mechanisms triggering objects as in young stellar objects (YSOs) or active galactic nuclei (AGNs), but the accretion disks of PNe may be not long-lived like the disks of YSOs or AGNs (Morris 1987; Soker & Rappaport 2001; Frank & Blackman 2004).

As shown in Figure 1.8, the two mechanisms leading to the formation of an accreting disk

may be either via binary systems with large orbital periods or through close binaries experiencing a common envelope phase. The existence of a stellar companion makes it possible the formation of an accreting disk when the AGB star (the primary component of the binary system), undergoes mass-loss episodes which are captured by the secondary stellar companion (Mastrodemos & Morris 1999; De Marco 2009). Mauron & Huggins (2006) have reported evidences of high mass-loss rates during the AGB phase in binary systems. Magneto-hydrodynamical (MHD) models have investigated the existence of a coupled disk and star produced by binary disruption in which one of the stars is rapidly rotating and its magnetic and polar axes are misaligned giving rise to multipolar structures (Blackman et al. 2001b). Whereas hydrodynamical simulations have been applied to either close binaries and binaries with larger orbital periods, the result of these simulations favours the scenario in which precessing jets appear (BRETs, Cliffe et al. 1996; Steffen & López 1998; Soker & Rappaport 2001) and sculpt PNe with point symmetric jets and knots.

Regarding the common envelope (CE) phase, this scenario can produce an accretion disk in close binaries during the CE phase, when the secondary stellar companion (M_i $\geq$0.1 M$_\odot$) and the primary (an AGB star) are engulfed by the envelope of the primary companion (Iben & Livio 1993; Rasio & Livio 1996; Soker 1997; De Marco 2009). Simulations to prove this scenario have shown the formation of an extended torus in a very short time ($\sim$1 yr) due to an ejection of the envelope, mainly in the equatorial plane (Sandquist et al. 1998). In the common envelope phase of close binaries, the jets are launched by the interaction with the secondary stellar component that can twist the envelope producing an enhancement of the magnetic field, setting up a dynamo effect that triggers a short-lived jet ($\leq$100 yr, Nordhaus & Blackman 2006).

The study of the role of CE binaries in PNe is important because it has been estimated that approximately 1 in 5 non-spherical PNe has a post-CE binary system (Miszalski et al. 2009). Regarding this, high-resolution simulations have explored evolved binary systems (with an AGB star as a primary companion) forming accreting disks via Bondi-Hoyle wind capture (Huarte-Espinosa et al. 2013). They have concluded that a white dwarf as secondary companion may produce an accreting disk able to launch highly collimated jets in a PN. For these simulations, the three scenarios studied have considered binaries with orbital radii of 10-20 AU, however, they suggest that CE binary systems are likely the most plausible scenario to achieve the accretion rates necessary to collimate the most high velocity jets reported in PNe. An example of a short orbital period post-CE binary system lay at the core of the Necklace Nebula (PN G054.2-03.4), which is about 1.16 days (Miszalski et al. 2013). Furthermore, this PN has provided the first evidence of mass-transfer via accreting disk in which the pre-WD has a carbon enriched main-sequence secondary companion, only possible if the primary has experienced the AGB phase. The Necklace also show jets likely triggered by this accreting disk. In the case of Fleming 1 (Boffin et al. 2012), a PN with remarkable point symmetric features, the CS has revealed a periodic behavior in the velocity measured using the C IV lines at 581.1 and 581.2 nm due to a close companion, resulting in a binary system with an orbital period of 1.2 days. The point symmetric morphology of this PN has been attributed to a precessing accreting disk produced by the

CE binary system progenitor.

Accretion disks formed via Bondi-Hoyle mass-accretion are not feasible for CE binaries, instead it has been proposed a mechanism named "wind Roche lobe (RL) overflow" to launch the accretion (Mohamed & Podsiadloski 2007; 2012). According to this scenario, the RL is not filled with the envelope of the primary companion, but the wind is channelled through the inner Lagrange point. Once the accretion disk is formed, the presence of magnetic fields may set the viscosity necessary to lose angular momentum and produce jets (i.e The Necklace Nebula, Abell 63, and Ethos 1, Tocknell et al. 2013).

The challenge nowadays is the observational detection of disks and jets to prove or, at least, envisage the shaping mechanism of axisymmetric PNe. The efforts are now focused in finding the proves of whether a single star or a binary system can produce these disks and jets, if these disks are in expansion or accreting material and what are the details of the physical processes involved in their formation and evolution.

1.3.   Infrared emission of post-AGB and PNe

The observation of sources towards infrared wavelengths implies the study of warm to cold material in the universe (few thousands to few tens K). Infrared emission is proper of all the bodies which radiates heat, this fact turn the IR into a prolific spectral range to be studied, since numerous astronomical objects emit certain quantity of radiation either in the IR or in radio. These IR and radio observations make possible the detection of structures that have suffered extinction through dust absorption of the radiation at shorter wavelengths, but re-radiate it at longer wavelengths. The extinction in the near-IR is typically one tenth of the extinction in the optical, whereas the extinction no longer affects towards mid-IR wavelengths and beyond.

According to the technology of the detectors used to register the astronomical infrared radiation ($\lambda 0.7$ μm - $\lambda 1000$ μm), this spectral range is divided into three regions: near-IR, mid-IR, and far-IR. As for the near- and mid-IR spectral regions, its bands are shown in the Figure 1.9. An overview of the IR spectral regions and its main characteristics concerning to the PNe phenomenon are presented in the following lines.

- **Near-IR (I, J, H, K, L, and M bands; 0.7 μm $< \lambda <$ 5 μm; $\sim$ 740 K $< T <$ 5000 K)**. This IR spectral range (see Figure 1.9) includes atomic emission of spectral lines (e.g. Brγ $\lambda 2.16$ μm, He II $\lambda 2.05$ μm, and [Fe III] $\lambda 2.14$ μm), as well as molecules such H$_2$ ($\lambda 2.12$ μm) and CO ($\lambda 4.7$ μm) (Hora et al. 1999). Moreover, emission of hot dust begins to have an important contribution upwards $\sim$2 μm in PNe. Emission of the broad PAH feature ($\lambda 3.3$ μm) may be present in the L-band. As mentioned before, the emission of the ro-vibrational molecule of CO in gaseous state may arise at near-IR wavelengths, and is an excellent tracer of cold to hot gas (CO sublimates at 20 K and dissociates at 4000 K in dense regions, Najita et al. (2007).
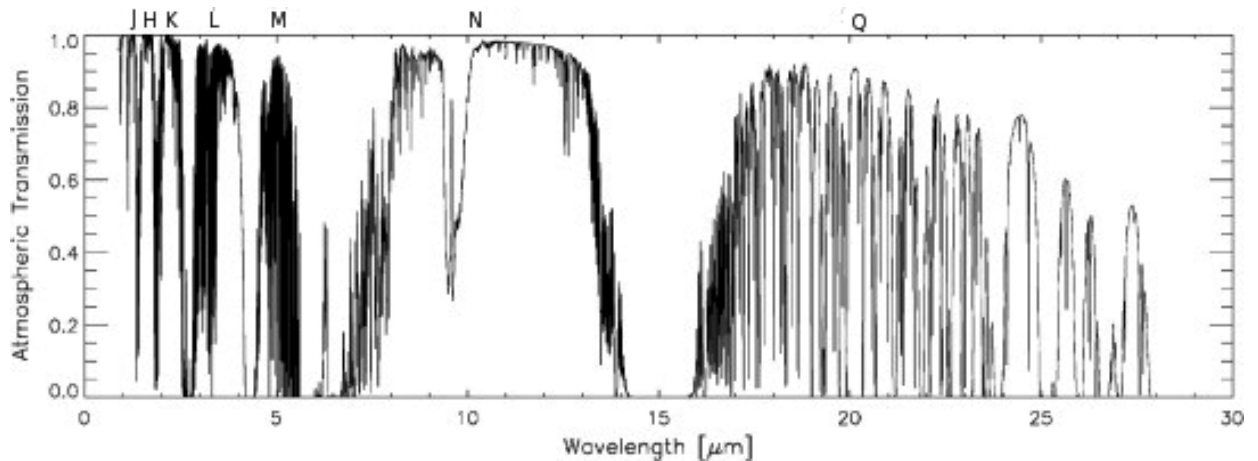
Figure 1.9 Near- and mid-IR photometric bands. The transmission of the atmosphere determines each of the photometric bands. Adapted from Chesneau (2007)

The CO molecule may be detected as bandhead at $\lambda 2.3$ μm (K-band) and emitting at the fundamental band at $\sim \lambda 4.7$ μm (M-band).

- **Mid-IR (N and Q bands; 7.5 μm $< \lambda <$ 30-40 μm; $\sim$ 100 K $< T <$ 740 K)**. The radiation at this IR spectral range (Figure 1.9) arises mainly from small-sized (5-50 Å) dust grains in non-equilibrium heating with the radiation field. As for PNe and objects in transition to this phase, the mid-IR range includes important atomic forbidden emission lines ([Ar IV] $\lambda 8.99$ μm, [S IV] $\lambda 10.49$ μm, and [Ne II] $\lambda 12.81$ μm). Furthermore, mid-IR has a wealth of features attributed either to carbonaceous dust grains (SiC at $\lambda 11.8$ μm), PAHs (polycyclic aromatic hydrocarbons), and silcate dust rich in Si and O (Rinehart et al. 2002). The presence of PAHs emitting at 7.3, 8.6, and 11.3 μm in PNe and objects in transition to this phase will depends on the chemistry of the source.

- **Far-IR (30-40 μm $< \lambda <$ 1000 μm; $\sim$ 10 K $< T <$ 100 K)**. As we move to far-IR wavelengths, we will observe cold material, e.g. molecular clouds and thermal continuum emission of dust in thermal equilibrium with the radiation field. The grains producing this thermal radiation are about 0.01 μm in size.

AGBs are important producers of dust grains given the physical conditions that they develop during late phases of stellar evolution. The detection of silicates and PAHs spectral features in their envelopes is thus natural. Moreover, the dust grains allow the formation of molecules. Figure 1.10 presents three different spectra: two near-IR spectra dominated by different emission mechanism (continuum or line emission dominated) and one starting at the L near-IR band up to the mid-IR Q-band in which emission lines and PAHs can be appreciated.
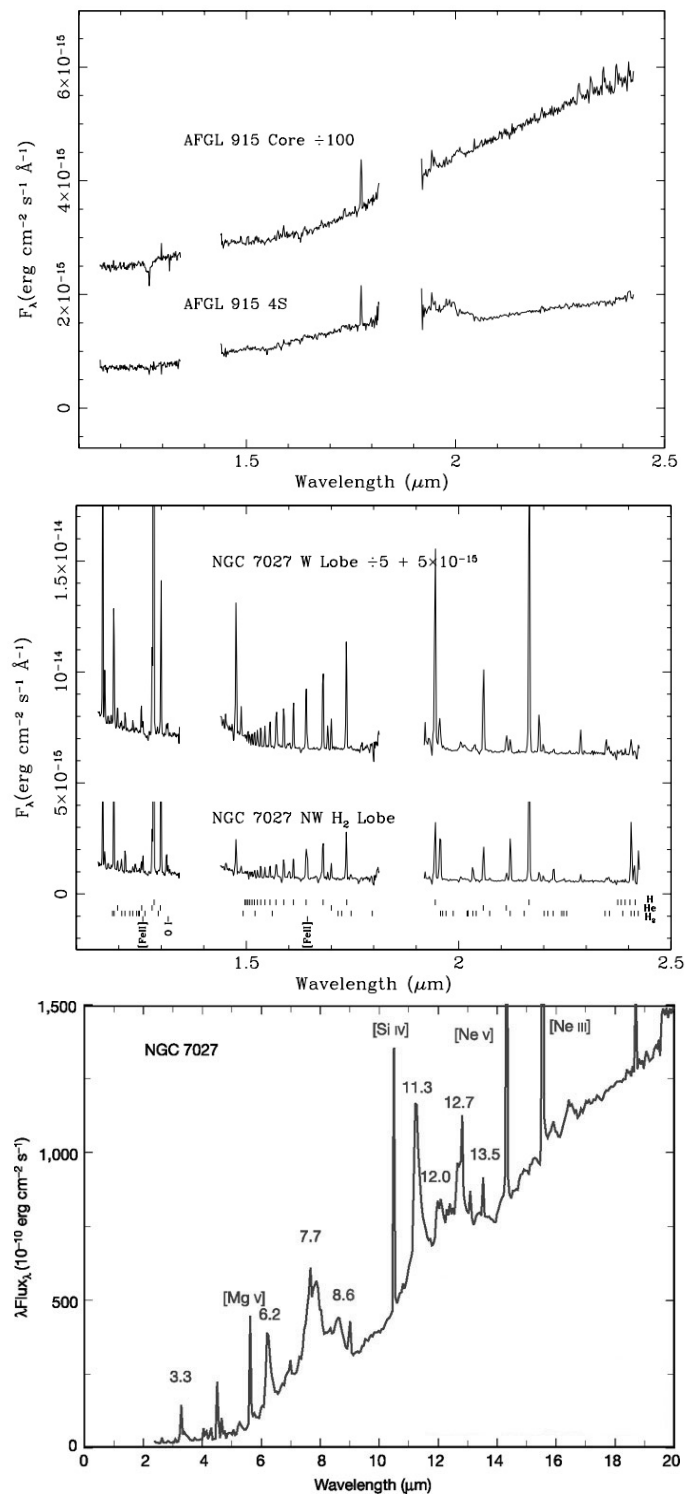
Figure 1.10 Near- and mid-IR low-resolution spectra of PNe. (*upper*) proto-PN AFGL 915. Its spectrum in the near-IR (H and K bands) is dominated by the continuum emission of warm dust, although it is possible to detect the presence of the CO bandhead at $\lambda 2.3$ μm in the spectrum of the core. (*middle*) NGC 7027 (Adapted from Hora et al. 1999). The near-IR spectrum of this PN is rich in hydrogen lines (labeled by the small vertical lines: neutral lines are the 1st row and molecular lines correspond to the 3rd row). (*bottom*) *ISO* spectrum of NGC 7027. This spectrum reveals the presence of forbidden emission lines as well as PAHs features indicated by the wavelengths in which they arise (Adapted from Kwok 2004).

Bibliography

Balick, B., Preston, H. L., & Icke, V. 1987. The evolution of planetary nebulae. II - Dynamical evolution of elliptical PNs and collimated outflows, AJ, 94, 1641

Balick, B., Perinotto, M., Maccioni, A., Terzian, Y., & Hajian, A. 1994, ApJ. FLIERs and other microstructures in planetary nebulae, 424, 800

Balick, B., & Frank, A. 2002. Shapes and Shaping of Planetary Nebulae, A&AR, 40, 439

Beckwith, S., Beck, S. C., & Gatley, I. 1984. The distribution of shocked gas in the bipolar nebulae CRL 2688 and CRL 618, ApJ, 280, 648

Beuzit, J.-L., Thebault, P., Perrin, G., & Rouan, D. 1994. Adaptive optics imaging of the Frosty Leo nebula, A&A, 291, L1

Blackman, E. G., Frank, A., & Welch, C. 2001. Magnetohydrodynamic Stellar and Disk Winds: Application to Planetary Nebulae, ApJ, 546, 288

Blackman, E. G., Frank, A., Markiel, J. A., Thomas, J. H., & Van Horn, H. M. 2001. Dynamos in asymptotic-giant-branch stars as the origin of magnetic fields shaping planetary nebulae, Nature, 409, 485

Blöcker, T. 1995. Stellar evolution of low and intermediate-mass stars. I. Mass loss on the AGB and its consequences for stellar evolution. A&A, 297, 727

Boffin, H. M. J., Miszalski, B., Rauch, T., et al. 2012. An Interacting Binary System Powers Precessing Outflows of an Evolved Star, Science, 338, 773

Bujarrabal, V., Castro-Carrizo, A., Alcolea, J., & Sánchez Contreras, C. 2001. Mass, linear momentum and kinetic energy of bipolar flows in protoplanetary nebulae, A&A, 377, 868

Bujarrabal, V., Castro-Carrizo, A., Alcolea, J., & Neri, R. 2005. The orbiting gas disk in the Red Rectangle, 441, 1031

Bujarrabal, V., Alcolea, J., Van Winckel, H., Santander-Garcia, M., & Castro-Carrizo, A. 2013, Extended rotating disks around post-AGB stars, arXiv:1307.1975

Castro-Carrizo, A., Neri, R., Bujarrabal, V., et al. 2012. Two short mass-loss events that unveil the binary heart of Minkowski's Butterfly Nebula, 545, A1

Chesneau, O., Lykou, F., Balick, B., et al. 2007. A silicate disk in the heart of the Ant, 473, L29

Chesneau, O., Collioud, A., De Marco, O., et al. 2006. A close look into the carbon disk at the core of the planetary nebula CPD-56Â°8032, A&A, 455, 1009

Chesneau, O. 2007. MIDI: Obtaining and analysing interferometric data in the mid-infrared, New Astronomy Reviews, 51, 666

Cliffe, J. A., Frank, A., & Jones, T. W. 1996. Precessing jets and molecular outflows: a 3D numerical study,MNRAS, 282, 1114

Corradi, R. L. M., & Schwarz, H. E. 1995. Morphological populations of planetary nebulae: which progenitors? I. Comparative properties of bipolar nebulae., A&A, 293, 871

Corradi, R. L. M., Balick, B., & Santander-García, M. 2011. The evolution of M 2-9 from 2000 to 2010, A&A, 529, A43

Davis, C. J., Smith, M. D., Stern, L., Kerr, T. H., & Chiar, J. E. 2003. Near-infrared spectroscopy of (proto)-planetary nebulae: molecular hydrogen excitation as an evolutionary tracer, MNRAS, 344, 262

Decin, L., Royer, P., Cox, N. L. J., et al. 2011, A&A, 534, A1 Discovery of multiple dust shells beyond 1 arcmin in the circumstellar envelope of IRC +10216 using Herschel/PACS

De Marco, O., Barlow, M. J., & Cohen, M. 2002. Discovery of an Edge-on Dust Disk around the [WC10] Central Star CPD-56Â°8032, ApJ, 574, L83

De Marco, O. 2009. The Origin and Shaping of Planetary Nebulae: Putting the Binary Hypothesis to the Test, PASP, 121, 316

Frank, A., & Blackman, E. G. 2004. Application of Magnetohydrodynamic Disk Wind Solutions to Planetary and Protoplanetary Nebulae, ApJ, 614, 737

García-Hernández, D. A., Manchado, A., García-Lario, P., et al. 2003. Nature of the H2 Emission Around Planetary Nebulae Precursors, Planetary Nebulae: Their Evolution and Role in the Universe, 209, 135

García-Hernández, D. A., Manchado, A., García-Lario, P., et al. 2006. Revealing the Mid-Infrared Emission Structure of IRAS 16594-4656 and IRAS 07027-7934, ApJ, 640, 829

García-Hernández, D. A. 2012. Molecular processes from the AGB to the PN stage, IAU Symposium, 283, 148

García-Segura, G., Langer, N., Różyczka, M., & Franco, J. 1999. Shaping Bipolar and Elliptical Planetary Nebulae: Effects of Stellar Rotation, Photoionization Heating, and Magnetic Fields, ApJ, 517, 767

García-Segura, G., López, J. A., & Franco, J. 2005. Magnetically Driven Winds from Post-Asymptotic Giant Branch Stars: Solutions for High-Speed Winds and Extreme Collimation, ApJ, 618, 919

Guerrero, M. A., Vázquez, R., & López, J. A. 1999. The Kinematics of Point-symmetric Planetary Nebulae, AJ, 117, 967

Guerrero, M. A., Villaver, E., Manchado, A., Garcia-Lario, P., & Prada, F. 2000. H2 and Br gamma Narrowband Imaging of Bipolar Planetary Nebulae, ApJS, 127, 125

Hajduk, M., Zijlstra, A. A., & Gesicki, K. 2008. An occultation event in the nucleus of the planetary nebula M 2-29, A&A, 490, L7

Hora, J. L., Deutsch, L. K., Hoffmann, W. F., & Fazio, G. G. 1996. Mid-Infrared Imaging of the Bipolar Nebulae AFGL 618, AFGL 2688, and AFGL 915, AJ, 112, 2064

Hora, J. L., & Latter, W. B. 1996. Molecular Hydrogen Imaging of Bipolar Planetary Nebulae, Bulletin of the American Astronomical Society, 28, 1402

Hora, J. L., Latter, W. B., & Deutsch, L. K. 1999. Investigating the Near-Infrared Properties of Planetary Nebulae. II. Medium-Resolution Spectra, ApJ, 124, 195

Huarte-Espinosa, M., Carroll-Nellenback, J., Nordhaus, J., Frank, A., & Blackman, E. G. 2013. The formation and evolution of wind-capture discs in binary systems, MNRAS, 433, 295

Iben, I., Jr., & Livio, M. 1993. Common envelopes in binary star evolution, PASP, 105, 1373

Icke, V., Preston, H. L., & Balick, B. 1989. The evolution of planetary nebulae. III - Position-velocity images of butterfly-type nebulae, AJ, 97, 462

Jura, M. 1990. Which Path for Stellar Evolution?. Ed. M.O. Mennessier & A. Omont, (Yvette Cedex: Editions Frontieres), 67

Kastner, J. H., & Weintraub, D. A. 1994. Broken symmetry: The structure of the dust envelope of IRC +10216, ApJ, 434, 719

Kastner, J. H., Weintraub, D. A., Gatley, I., Merrill, K. M., & Probst, R. G. 1996. H2 Emission from Planetary Nebulae: Signpost of Bipolar Structure, ApJ, 462, 777

Kwok, S., Purton, C. R., & Fitzgerald, P. M. 1978. On the origin of planetary nebulae, ApJ, 219, L125

Lagadec, E., Verhoelst, T., Mékarnia, D., et al. 2011. A mid-infrared imaging catalogue of post-asymptotic giant branch stars, MNRAS, 417, 32

Latter, W. B., Hora, J. L., Kelly, D. M., Deutsch, L. K., & Maloney, P. R. 1993. A new near-infrared imaging study of AFGL 2688 , AJ, 106, 260

Lewis, B. M. 1989. The chronological sequence of circumstellar masers - Identifying proto-planetary nebulae, ApJ, 338, 234

Lopez, J. A., Meaburn, J., & Palmer, J. W. 1993, ApJ. Kinematical Evidence for a Rotating, Episodic Jet in the Planetary Nebula Fleming 1, 415, L135

Lopez, J. A. 1997, Planetary Nebulae IAUS. Jets and Brets in Planetary Nebulae (Invited Review), 180, 197

López, J. A., Meaburn, J., Rodríguez, L. F., et al. 2000, ApJ. The Formation of a Multiple Planetary Nebula:Hubble Space Telescope/WFPC2 Observations of KJPN 8, 538, 233

Luhman, K. L., & Rieke, G. H. 1996. High-Resolution Near-Infrared Spectroscopy of Hubble 12, ApJ, 461, 298

Lykou, F., Chesneau, O., Zijlstra, A. A., et al. 2011. A disc inside the bipolar planetary nebula M2-9, A&A, 527, A105

Manchado, A., Stanghellini, L., & Guerrero, M. A. 1996. Quadrupolar Planetary Nebulae: A New Morphological Class, ApJL, 466, L95

Manchado, A. 1997. On the morphology and internal kinematics of PNe (Invited Review). Planetary nebulae, Proceedings of the 180th Symposium of the International Astronomical Union (IAU), 180, 184

Mastrodemos, N., & Morris, M. 1999. Bipolar Pre-Planetary Nebulae: Hydrodynamics of Dusty Winds in Binary Systems. II. Morphology of the Circumstellar Envelopes, ApJ, 523, 357

Mauron, N., & Huggins, P. J. 1999. Multiple shells in the circumstellar envelope of IRC+10216, A&A, 349, 203 Multiple shells in the circumstellar envelope of IRC+10216

Mauron, N., & Huggins, P. J. 2006. Imaging the circumstellar envelopes of AGB stars, A&A, 452, 257

Meixner, M. 1997. The morphology of dust emission in Planetary Nebulae and proto-Planetary Nebulae (Invited Review), Planetary Nebulae, 180, 325

Meixner, M., Ueta, T., Dayal, A., et al. 1999. A Mid-infrared Imaging Survey of Proto-Planetary Nebula Candidates , ApJS, 122, 221

Mellema, G., & Frank, A. 1995. Radiation gasdynamics of planetary nebulae - V. Hot bubble and slow wind dynamics, MNRAS, 273, 401

Miranda, L. F., Vázquez, R., Corradi, R. L. M., et al. 1999. Detection of Collimated Bipolar Outflows in the Planetary Nebula NGC 6572 Shaping Its Nebular Shell, ApJ, 520, 714

Miranda, L. F., Gómez, Y., Anglada, G., & Torrelles, J. M. 2001. Water-maser emission from a planetary nebula with a magnetized torus. Nature, 414, 284

Miszalski, B., Acker, A., Moffat, A. F. J., Parker, Q. A., & Udalski, A. 2009. Binary planetary nebulae nuclei towards the Galactic bulge. I. Sample discovery, period distribution, and binary fraction, A&A, 496, 813

Miszalski, B., Boffin, H. M. J., & Corradi, R. L. M. 2013, MNRAS. A carbon dwarf wearing a Necklace: first proof of accretion in a post-common-envelope binary central star of a planetary nebula with jets, 428, L39

Mohamed, S., & Podsiadlowski, P. 2007. Wind Roche-Lobe Overflow: a New Mass-Transfer Mode for Wide Binaries, 15th European Workshop on White Dwarfs, 372, 397

Mohamed, S., & Podsiadlowski, P. 2012. Mass Transfer in Mira-type Binaries, Baltic Astronomy, 21, 88

Morris, M. 1987. Mechanisms for mass loss from cool stars, PASP, 99, 1115

Morris, M., & Reipurth, B. 1990. The optical form of the bipolar preplanetary nebula IRAS 09371 + 1212, PASP, 102, 446

Morris, M., & Sahai, R. 1999, Bulletin of the American Astronomical Society. Mid-Infrared Observations of Pre-Planetary Nebulae with the Keck Telescope ,31, 975

Najita, J. R., Carr, J. S., Glassgold, A. E., & Valenti, J. A. 2007. Gaseous Inner Disks, Protostars and Planets V, 507

Nordhaus, J., & Blackman, E. G. 2006. Low-mass binary-induced outflows from asymptotic giant branch stars, MNRAS, 370, 2004

Olofsson, H. 2000. The Neutral Envelopes around AGB and Post-AGB Objects Their Structure and Kinematics, The Carbon Star Phenomenon, 177, 413

Olofsson, H., Bergman, P., Lucas, R., et al. 2000, A&A, 353, 583 A high-resolution study of episodic mass loss from the carbon star TT Cygni

O'Connor, J. A., Redman, M. P., Holloway, A. J., et al. 2000, ApJ. The Hypersonic, Bipolar, Knotty Outflow from the Engraved Hourglass Planetary Nebula MYCN 18, 531, 336

Pontoppidan, K. M., Blake, G. A., van Dishoeck, E. F., et al. 2008. Spectroastrometric Imaging of Molecular Gas within Protoplanetary Disk Gaps, ApJ, 684, 1323

Pontoppidan, K. M., Blake, G. A., & Smette, A. 2011. The Structure and Dynamics of Molecular Gas in Planet-forming Zones: A CRIRES Spectro-astrometric Survey, ApJ, 733, 84

Pottasch, S. R. 1984. Planetary nebulae - A study of late stages of stellar evolution, Astrophysics and Space Science Library, 107

Ramos-Larios, G., Guerrero, M. A., & Miranda, L. F. 2008. The Unusual Distributions of Ionized Material and Molecular Hydrogen in NGC 6881: Signposts of Multiple Events of Bipolar Ejection in a Planetary Nebula, AJ, 135, 1441

Ramos-Larios, G., Guerrero, M. A., Suárez, O., Miranda, L. F., & Gómez, J. F. 2009. Searching for heavily obscured post-AGB stars and planetary nebulae. I. IRAS candidates with 2MASS PSC counterparts, A&A, 501, 1207

Ramos-Larios, G., Guerrero, M. A., Suárez, O., Miranda, L. F., & Gómez, J. F. 2012. Searching for heavily obscured post-AGB stars and planetary nebulae. II. Near-IR observations of IRAS sources, A&A, 545, A20

Rasio, F. A., & Livio, M. 1996. On the Formation and Evolution of Common Envelope Systems, ApJ, 471, 366

Renzini, A. 1981. Evolutionary effects of mass loss in low-mass stars, IAU Colloq. 59: Effects of Mass Loss on Stellar Evolution, 89, 319

Rinehart, S. A., Houck, J. R., Smith, J. D., & Wilson, J. C. 2002. Mid-infrared spectroscopy of protoplanetary and planetary nebulae, MNRAS, 336, 66

Roddier, F., Roddier, C., Graves, J. E., & Northcott, M. J. 1995. Adaptive optics imaging of proto-planetary nebulae: Frosty Leo and the Red Rectangle, ApJ, 443, 249

Sahai, R., & Trauger, J. T. 1998. Multipolar Bubbles and Jets in Low-Excitation Planetary Nebulae: Toward a New Understanding of the Formation and Shaping of Planetary Nebulae, AJ, 116, 1357

Sahai, R. 2000. The Starfish Twins: Two Young Planetary Nebulae with Extreme Multipolar Morphology, ApJ, 537, L43

Sahai, R. 2002. Bipolar and Multipolar Jets in Protoplanetary and Planetary Nebulae. Revista Mexicana de Astronomia y Astrofisica Conference Series, 13, 133

Sandquist, E. L., Taam, R. E., & Burkert, A. 1998. The Common Envelope Phase for Pre-Cataclysmic Variables and Double Degenerate Stars, Bulletin of the American Astronomical Society, 30, #102.11

Schoenberner, D. 1981. Late stages of stellar evolution - Central stars of planetary nebulae, A&A, 103, 119

Schwarz, H. E., Corradi, R. L. M., & Melnick, J. 1992. A catalogue of narrow band images of planetary nebulae, A&AS, 96, 23

Schwarz, H. E., Aspin, C., Corradi, R. L. M., & Reipurth, B. 1997, A&A. M 2-9: moving dust in a fast bipolar outflow, 319, 267

Smith, N., Balick, B., & Gehrz, R. D. 2005. Kinematic Structure of H2 and [Fe II] in the Bipolar Planetary Nebula M2-9, AJ, 130, 853

Shu, F. H., Shang, H., Glassgold, A. E., & Lee, T. 1997. X-rays and fluctuating X-winds from protostars., Science, 277, 1475

Soker, N. 1997. Properties That Cannot Be Explained by the Progenitors of Planetary Nebulae, ApJS, 112, 487

Soker, N., & Rappaport, S. 2001. Departure from Axisymmetry in Planetary Nebulae, ApJ, 557, 256

Stanghellini, L., Corradi, R. L. M., & Schwarz, H. E. 1993. The Correlations Between Planetary Nebula Morphology and Central Star Evolution, A&A, 276, 463

Steffen, W., & López, J. A. 1998. Jets and the Shaping of the Giant Bipolar Envelope of the Planetary Nebula KjPn 8, ApJ, 508, 696

Riera, A., Binette, L., & Raga, A. C. 2006. Shock excitation of the knots of Hen 3-1475, A&A, 455, 203

Tafoya, D., Imai, H., Gomez, Y., et al. 2011. Measurement of the Distance and Proper Motions of the H2O Masers in the Young Planetary Nebula K 3-35, PASJ, 63, 71

Tocknell, J., De Marco, O., & Wardle, M. 2013. Constraints on Common Envelope Magnetic Fields from Observations of Jets in Planetary Nebulae, arXiv:1308.5027

Uscanga, L., Gómez, Y., Raga, A. C., et al. 2008. Kinematics of the H_2O masers at the centre of the planetary nebula K3-35, MNRAS, 390, 1127

Vassiliadis, E., & Wood, P. R. 1993. Evolution of low- and intermediate-mass stars to the end of the asymptotic giant branch with mass loss, ApJ, 413, 641

Weidemann, V. 1990. Masses and evolutionary status of white dwarfs and their progenitors, ARA&A, 28, 103

Weinberger, R. 1989, A&A. A catalogue of expansion velocities of Galactic planetary nebulae, 78, 301

Weigelt, G., Balega, Y. Y., Blöcker, T., et al. 2002. Bispectrum speckle interferometry of IRC +10216: The dynamic evolution of the innermost circumstellar environment from 1995 to 2001, A&A, 392, 131

2

Observational Techniques

As was mentioned in §1.2.1, the study of objects in transition to PN phase requires the use of powerful observational techniques that resolve small-sized structures which are often embedded in dusty environments. For this reason we have selected two new generation instruments of the European Southern Observatory (ESO) Very Large Telescope (VLT) operating in the infrared (IR): VISIR (mid-IR, VLT Imager and Spectrometer for the mid-IR, Lagage et al. 2004) and CRIRES (near-IR; CRyogenic high-resolution Infra-Red Echelle Spectrograph, Kaeufl et al. 2004). Both instruments have demonstrated in previous studies their capabilities to resolve compact sources and to study with great detail these kind of objects in which the high-resolution is essential. The Chapter 2 of this thesis is devoted to the description of these two instruments. Additionally, we mention the techniques used for the analysis of the data presented in this thesis.

2.1. Radiation mechanisms at near- and mid-IR wavelengths

If we deal with radiation of an astronomical source traveling through an optical path we must consider the effects produced by the travel of the light that is detected by the telescope and afterwards analyzed. These effects are accounted by the radiative transfer function (RTF). The RTF refers to the intensity of radiation and establishes that this intensity (I_ν) will suffer losses due to extinction and gains due to emission. Moreover, this behaviour must conserve the energy (second law of thermodynamics): for any loss of energy must be a gain.

Let us consider the simplest case to exemplify the RTF for a light beam traveling through an homogeneous medium, in local thermodynamic equilibrium (LTE), and neglecting the effects produced by scattering. In general, RTF equation is written as follows:

$$\frac{dI_\lambda}{dx} = -\kappa_\lambda \cdot I_\lambda + \rho \cdot j_\lambda \qquad (2.1)$$

Where x is the coordinate along the line of sight, κ_ν is the extinction coefficient, ρ is the mass density, and j_ν is the emission coefficient per unit of mass. The absorption is an attenuation per unit of length at certain frequency ν. Whereas the emission coefficient in LTE depends on the Planck function $B_\lambda(T)$. Thus, the emission can be expressed as follows:

$$\rho \cdot j_\lambda = \kappa_\lambda \cdot B_\lambda(T) \qquad (2.2)$$

For the emission, κ_λ is the attenuation suffered due to absorption too. Therefore, for LTE and no scattering, the RTF is reduced to

$$\frac{dI_\lambda}{dx} = \kappa_\lambda \cdot \rho(B_\lambda(T) - I_\lambda) \qquad (2.3)$$

Although the observation of celestial objects involves more factors which complicate the RTF that has no analytical solution but numerical, this basic idea of RTF is the point of departure for the interactions between the radiation and the medium affecting the signal of the sources studied in this thesis.

2.1.1. Heating and cooling

During the PN phase, the UV photons (ionization potential > 13.6 eV) ionize the hydrogen atoms while electrons are released with each interaction of this type. The electron liberated interacts with other thermal electrons, resulting in an increase in the temperature of the gas. This process is called photoionization and is a typical heating mechanism of plasma. On the other hand, thermal emission of tiny dust grains arises because they are exposed to radiative heating due to the energy density of the starlight (0.5 eV cm^{-1}). This heating mechanism produce photoelectrons that are ejected by these tiny dust grains. The thermal emission arising from these dust grains at shorter IR wavelengths (1-10 μm) is not in thermal equilibrium, that is, they can not be treated as black bodies, instead they are "stochastically heated". When these smaller dust grains with less than 100 atoms are heated by UV photons, its tiny size makes this heating mechanism strongly time dependent and thus they are not in equilibrium with the radiation field. Once a UV photon stroke on a dust grain, a large ΔT_d is experienced followed by radiative cooling in form of continuum radiation. For this reason the range of temperatures of the thermal continuum radiation produced by stochastically heated dust grains is wider ($500 < T_d < 1000$) than the temperature range from the larger dust grains emitted in the far-IR. Finally, shocks produced by outflows and jets in which supersonic compression of the material are present, increase the temperature of the gas too.

Near- and mid-IR spectral ranges are characterized by thermal radiation. The thermal emission of ionized gas might be present as broad thermal continuum radiation and in form of spectral emission lines. The emission of the continuum during the PN phase are produced by free-free (Bremsstrahlung) radiation; this name is because the electrons are free before and afterwards they are accelerated and

scattered off from the ions that give rise to this type of radiation. The radiation mechanisms hereafter mentioned are the result of the heating mechanisms, in a sense, the radiation emitted is the result of the system trying to reach the equilibrium with cooling mechanisms.

- **Recombination lines (RLs)** is a type of thermal radiation proper of gaseous sources in which excited states of ions de-excitate in cascade down to the ground state. The most abundant RLs emerge from neutral hydrogen H I, given rise to RLs of the series of Brackett and Pfund in the near- and mid-IR (e.g. $Br\gamma \lambda 2.16$ μm and $Br\alpha \lambda 4.05$ μm, and $Pa\alpha \lambda 7.46$ μm). Other elements may produce RLs (i.e. He, O, and Fe), its intensity depends on the abundance of the element and other factors.

- **Collisionally excited lines (CELs)** are generated by the interaction of atoms or ions with thermal electrons and every excitation undergo a radiative de-excitation. The electron temperature (T_e) necessary to excite CELs depend of the ion: hydrogen lines require $T_e \geq$ 20,000 K, whereas N, O, or Ne can be excited at lower T_e, given rise to infrared CELs. The emission of CELs is constrained by the probability (P) of the transition, for this reason, they can be permitted ($P \sim 10^8$ s^{-1}), semi-forbidden ($P \sim 10^2$ s^{-1}), and forbidden ($P \leq 10^{-2}$ s^{-1}).

Finally, it is important to mention that the emission in PNe is generally stratified, i.e., the degree of ionization decreases with the distance from the central star as a result of the attenuation of the stellar radiation. Thus, in regions near to the CS, species with high ionization potentials are expected while the species with low ionization potentials, such as atoms singly ionized of C, N, O, or neutral atoms are expected at the outermost regions of PNe. On the other hand, density condensations of certain ions or molecules are also detected in PNe. It has been demonstrated that their origin is not related with stratification of ionization, but it arises from cooling mechanisms produced by shielding or supersonic shocks, like the case of the optical [N II] emission line or the H_2 molecule.

2.1.2. Emission of spectral lines

As we have seen, heating mechanisms in the circumstellar material either in the post-AGB, proto-PNe or during PN phase lead to cooling mechanisms originating spectral lines along the electromagnetic spectrum. A spectral line may arise from atoms or molecules, in emission or in absorption. Hereafter we will focus in the atomic and molecular spectral emission lines and how they emerge. Spectral emission lines arise from neutral and ionized atoms when the electrons at higher excitation levels de-excitate to the ground state emitting a photon with the same energy than the difference of energy (ΔE) between the energy levels (n_1 and n_2) in which this transition occur (Figure 2.1).

$$\Delta E = 13{,}6(\tfrac{1}{n_1^2} + \tfrac{1}{n_2^2})eV \tag{2.4}$$
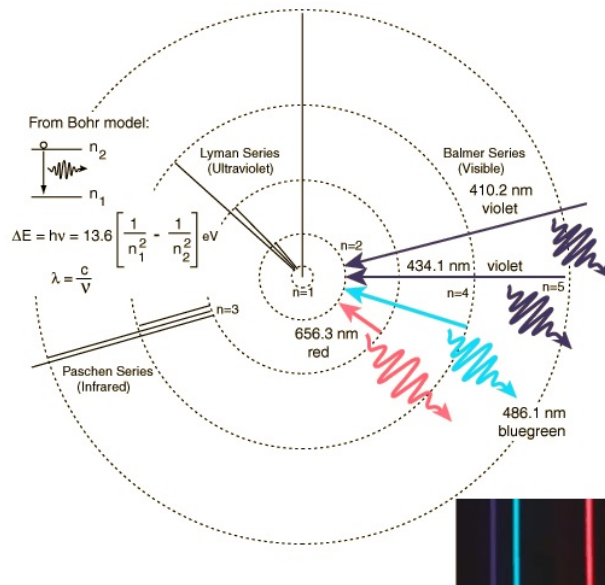
Figure 2.1 Electronic transitions originating the atomic spectra of the hydrogen series.

On the other hand, molecules are formed by two or more atoms chemically bounded by the interaction between the electrons of the involved atoms. Like the atoms, molecules exist in well defined energy levels, but they dissociate at certain energy of few eV, depending on the molecule. Since they have energy levels, UV and optical spectral lines are produced by electronic transitions within the molecules. Additionally, molecules vibrate and rotate, thus emission lines may arise from changes in the vibrational or in the rotational states (Δv and ΔJ, where v and J are the vibrational and rotational quantum numbers of the molecule). Vibrational and rotational lines emerge in the IR towards longer wavelengths. A mixture of rotational-vibrational lines (a.k.a. ro-vibrational lines) arise exclusively in the IR. Given the nature of the sources of this thesis, we will introduce some basic ideas of ro-vibrational spectra of diatomic linear molecules, such H_2 and CO.

A molecule with N atoms vibrating behave as coupled harmonic oscillators system with $n = 3N - 6$ degrees of freedom, or $n = 3N - 5$ for linear molecules, with certain rotational energy. The rotational degrees of freedom for non-linear molecules are three, one per each axis whereas a diatomic molecule has one vibrational degree of freedom and two for rotation.

The energy of the vibrations is quantized, likewise the energy levels of atoms. The vibrational energy of a molecule are described as follows:

$$E_v = h\nu(v + \tfrac{1}{2}) \tag{2.5}$$

where v=0, 1, 2 ..., $\nu = \frac{1}{2\pi}(\frac{\kappa}{\mu})^{1/2}$ is the frequency of the vibration, κ is the force constant, and μ is the reduced mass of the diatomic molecule with masses m_1 and m_2. The vibrational transition
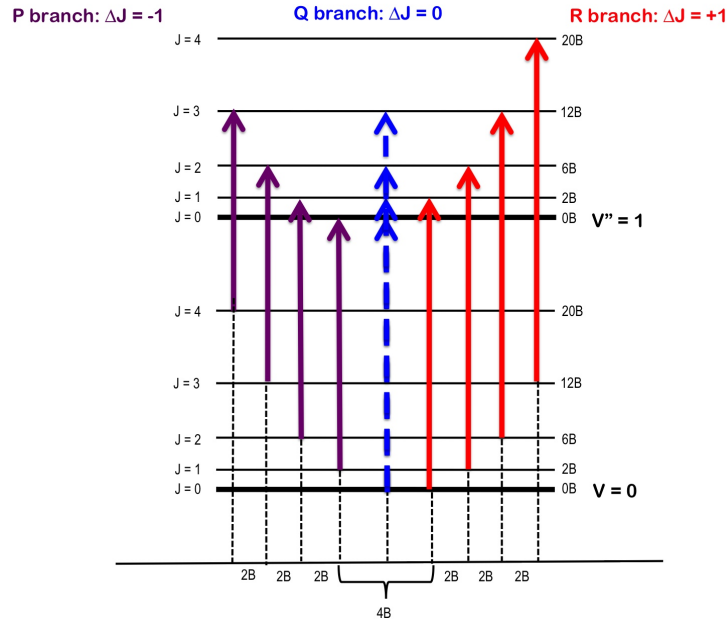
Figure 2.2 Transitions originating ro-vibrational spectra. B is the rotational constant related with the moment of inertia of the molecule.

selection rule is that vibrational state may increase or decrease by one energy level from the original vibrational state, that is $\Delta v = \pm 1$.

On the other hand, a rotating molecule is treated as a rigid rotor with its rotational energy quantized as well:

$$E_r = \tfrac{h}{8\pi^2 I} J(J+1) \tag{2.6}$$

where $I = \mu r^2$ is the moment of inertia of the molecule and μ is again the reduced mass of the molecule. The rotational transition selection rules give rise to the P-branch ($\Delta J = -1$), R-branch ($\Delta J = +1$), and Q-branch ($\Delta J = 0$, Figure 2.2).

Among all the molecules present in a PN spectra, as well as in proto-PN, molecules of CO and H_2, the so called "tracer molecules", may be detected as well. In general, the most important mechanisms of CO emission are collisions between CO molecules and H I and/or H_2. Emission from CO ro-vibrational near-IR emission lines have traced innermost hot gaseous disks in YSOs such T Tauri stars and HAeBe stars (Shu et al. 1997; Najita et al. 2007), as well as in protoplanetary disks (Pontoppidan et al. 2008; Pontoppidan et al. 2011). The CO ro-vibrational fundamental band at $\sim \lambda 4.7$ μm trace structures of cool gas between 200 and 1000 K.

H_2 is the most abundant molecule and no pure rotational spectral lines are emitted at wavelengths beyond the mid-IR. H_2 lacks dipole dipole moment making the transitions $\Delta J = \pm 1$ forbidden. Following this dipole selection rule, H_2 molecules have the following notation: $v_u - v_l$ $O(J)$; for $J=2$,

$v_u - v_l$ $Q(J)$; for J=0, $v_u - v_l S(J)$; for J=2. However, because of its moment of inertia, H_2 produce pure rotational transitions in the mid-IR (at $\lambda12$ μm (J=4-2) and at $\lambda28$ μm (J=2-0)). Therefore, the pure rotational, as well as vibrational and ro-vibrational H_2 spectrum are found at IR wavelengths. The emission of the H_2 molecules at IR wavelengths arise in warm gas (500-2000 K) due to CELs produced by shocks or by UV fluorescence induced by nearby star.

One of the most H_2 studied spectral lines is the ro-vibrational transition 1-0S(1) at 2.12 μm in the K-band of the near-IR. UV Fluorescent excited H_2 is found in PNe in equatorial rings (Kastner et al. 1996; Guerrero et al. 2000) as well as in bipolar lobes, as shown by the PN Hb 12 and the PN M2-9 (Luhman & Rieke 1996; Hora & Latter 1996; Smith et al. 2005). The proto-PN CRL 2688 (The Egg nebula, Beckwith et al. 1984; Latter et al. 1993; Davis et al. 2003) and PN NGC 6881 (Ramos-Larios et al. 2008) have the H_2 emission distributed along the equator and at the tips of bipolar lobes, nonetheless, H_2 in both PNe is collisionally excited. H_2 emission can be detected practically during all the post-AGB phase, thus, this emission has been proposed to be used as an evolutionary tracer in PNe and sources in transition to this phase: fluorescent excitation seems to be the important excitation mechanism of H_2 in young PN, whereas collisional excitation of this molecule are the dominant excitation mechanism during the proto-PN phase (Davis et al. 2003).

2.2.   Diffraction limit
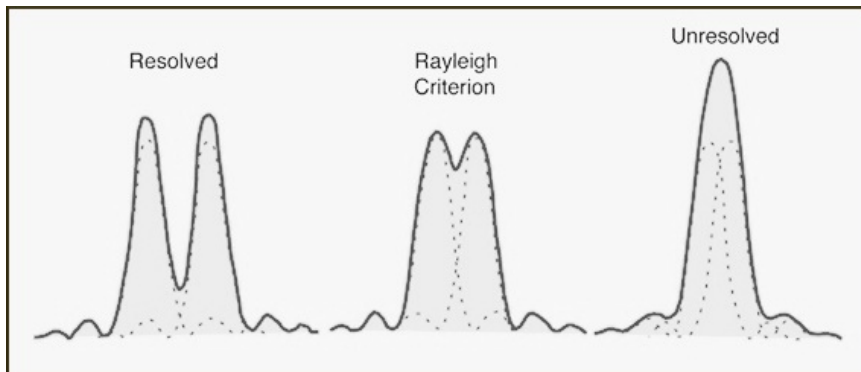
Figure 2.3 Intensity curves for the radial distribution of the diffracted light for different separations. (*Left*) Intensity curve for a fully resolved source. (*Middle*) Intensity curve for the minimum resolvable detail (Rayleigth criterion). (*Right*) Intensity curve of a unresolved source.

Since the objects studied in this thesis are compact sources emitting at IR wavelengths, the diffraction limit (Figure 2.3) concept must be introduced. Observations performed with a telescope with a primary mirror of diameter D (aperture), the resolution achieved are limited by the aperture diffraction follows:

$$d = \frac{1,22\lambda}{D} \qquad (2.7)$$
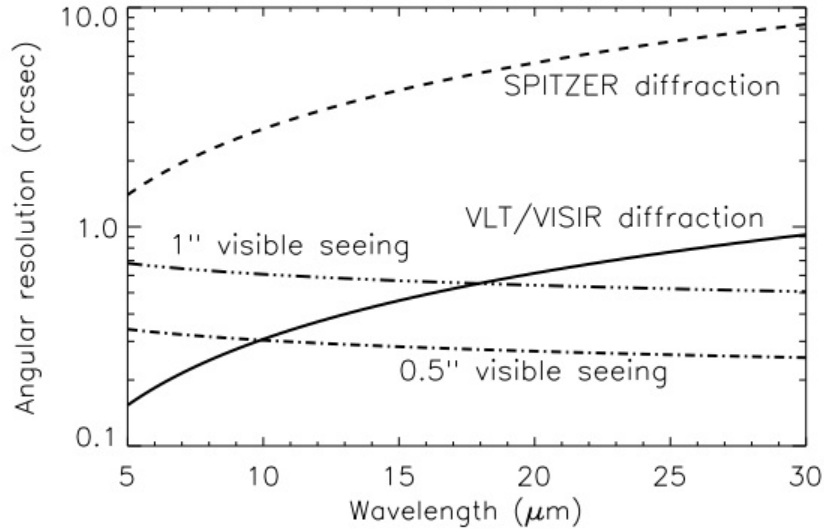
Figure 2.4 Diffraction-limit (full line) of VISIR-VLT versus seeing. The diffraction-limit of *Spitzer* (dashed line) is shown for comparison. Adapted from VISIR-VLT user manual.

The diffraction limit (d, in radians) is the minimum angular separation between two sources or two structures observed by a telescope, and is function of the wavelength observed (in cm) and of the diameter of the telescope (in cm). The diffraction limit in the near- and mid-IR of a VLT unit telescope (UT, aperture=8.2 m) at 2.2 μm is $0\rlap{.}{''}07$ μm and $0\rlap{.}{''}3$, respectively. For good seeing conditions ($\leq 0\rlap{.}{''}5$), the resolution is affected by atmospheric turbulence, thus, nearly diffracted limited images are commonly produced in these telescopes.

2.3.   VISIR-VLT: high angular resolution imaging in the mid-IR

VISIR-VLT is an imager and spectrograph capable of acquiring diffraction-limited images ($\sim$0.3$''$ in the N-band, Figure 2.4), as well as high and low resolution spectra. It is mounted at UT3 (a.k.a. Melipal). The observations with VISIR-VLT are performed at high sensitivity in the mid-IR N- and Q-bands (5 mJy 10σ/1h at 8.6 μm up to 100 mJy 10σ/1h at 19.5 μ), offering the possibility to study the main spectral range in which the thermal emission of small dust grains may be detected, as well as atomic and molecular emission lines, PAHs and silicates features.

The detector of VISIR-VLT is a DRS, former Boeing, of 256$\times$256 pixels. Its imager offers two spatial scales: $0\rlap{.}{''}127$ and $0\rlap{.}{''}075$ with a $32\rlap{.}{''}5$ and $19\rlap{.}{''}2$ field of view (FoV), respectively. In this thesis, we have used the highest spatial scale given the small angular extent of the sources studied.

2.3.1.   Observations in the mid-IR and analysis

Observations in the IR, from 3 to 25 μm, are contaminated with the signal of atmospheric emission known as "mid-IR background", emitting as a blackbody of 253 K. Hence, ground-based IR observa-
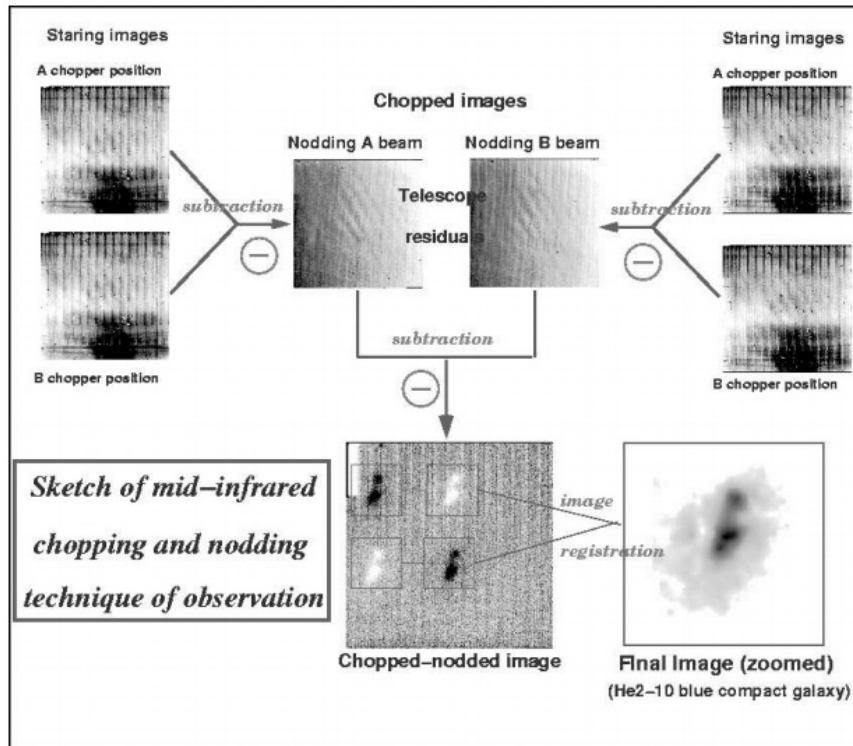
Figure 2.5 Chopping and nodding technique as performed by VISIR in the so-called PERPENDICU-LAR mode. Adapted from VISIR-VLT ESO user manual.

tions apply the chopping and nodding (chopnod, Figure 2.5) techniques to reduce this atmospheric contamination. When chopping is performed the secondary mirror of the telescope oscillates at high frequencies of several Hz. The first chopping position A has a field of view with the emission of the source and from the sky, while the chopping position B has sky emission solely. Thus, A and B chopping positions are subtracted and co-added removing almost all the atmospheric contamination. Nodding technique is applied to completely remove this contamination by moving the telescope to start chopping again. The number of nodding cycles will depend on the exposure time needed to achieve the signal to noise required. Usually, depending of the magnitude of the source, the image of the source only appears when the resulting A and B nodding images are subtracted and co-added.

The chopnod pattern used in our observations was ABBA with chopping cycles of 80 to 100 (number of frames for each chopping position), that have been co-added and then subtracted as part of the observations performed in the so called NORMAL mode resulting in a data cube of several tens of nodding images A and other data cube corresponding to the data cube for the nodding position B.

High resolution imaging analysis: Deconvolution

An image observed is degraded by the point spread function (PSF) of the instrument used, that is, the response of the detector used to a point source. Deconvolution is used to improve the quality
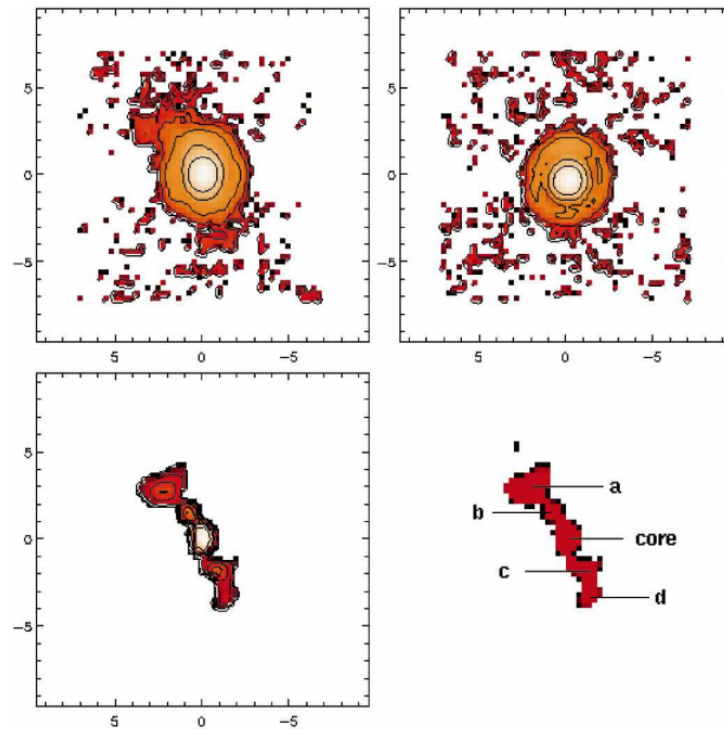
Figure 2.6 (*upper left*) Mid-IR raw image of the AGN NGC 1068. (*upper right*) The star used as PSF. (*down*) The image reconstructed after deconvolution (Alloin et al. 2000).

of an image, correcting the artifacts produced by the PSF and also is a powerful technique to correct the blurring provoked by the atmosphere. This correction results specially useful for small-sized sources, since the deconvolution with a standard star, which provides a good approximation to the PSF, allows us to sharpen and enhance the characteristics of the image observed. These standard stars used as PSF are well-known standard stars, frequently used to perform flux calibrations. These observations of a nearby standard star must be executed using the same filters and instrumental setup, soon before or after the observation of the science observation of the source of interest.

The deconvolution of astronomical images has proven to be crucial in certain topics. For example, deconvolution of mid-IR images at 20 μm revealed the innermost regions affected by the extinction in the optical of the AGN NGG 1068 (Figure 2.6 Alloin et al. 2000). This procedure also has improved the resolution of those observations limited by the seeing.

Observations of the sources $O(x, y)$ provide the data which is the intensity distribution as observed by the detector $I(x, y)$. For an imaging system linear and shift-invariant the relation between the intensity distribution observed and the original image of the source is given by:

$$I(x, y) = P * O(x, y) + N(x, y) \tag{2.8}$$

Where P is the PSF (kernel) of the detector, $N(x, y)$ is additive noise, and * is the convolution operator. The VISIR images presented in this thesis have been deconvolved using either Richardson-Lucy (Richardson 1972; Lucy 1974) or maximum likelihood algorithm. Richardson-Lucy algorithm is an iterative non-linear algorithm in which the PSF is approximated to the unity after each iteration. Whereas the maximum likelihood algorithm is iterative as well and represents the most probable solution from Gaussian statistics. Both algorithms are based in Bayesian probability:

$$P(O|I) = \frac{P(I|O)P(O)}{P(I)} \tag{2.9}$$

Once again, O is the original image of the source and I is the intensity distribution detected. That is, the probability of observe the Image I given the original image O. Therefore, when these methods are used a probability model is fitted to the data and the result is the probability distribution on the model parameters and observed quantities.

A critical point using iterative deconvolution algorithms regards in the number of iterations executed. As mentioned, the purpose is the improvement of the image quality, removing the PSF artifacts and enhancing real morphological characteristics. Thus, the number of iterations of both algorithms used in this thesis (Richardson-Lucy and Maximum Likelihood) has been fairly conservative[1] to prevent morphological artifacts. The final deconvolved images used in this thesis have been carefully inspected after different number of iterations and the optimal ones have been selected for the analysis.

2.4. CRIRES-VLT: high resolution spectro-astrometry

The Cryogenic high-resolution Infra-Red Echelle Spectrograph (CRIRES), mounted at the Nasmyth focus of the UT1 (Antu), is a high-sensitive instrument of the VLT operating in the near-IR (0.95 μm to 5.2 μm) and provides high-resolution long-slit (40″) spectra with two slit widths (0.″2 and 0.″4) and with a spatial sampling of 0.″086. In addition, CRIRES-VLT improve the observations when the adaptive optics system MACAO is used. The prism acting as a pre-disperser and an echelle grating of 31.6 lines/mm with a 63.5°blaze angle are its main optical elements. An array of four Aladdin III detectors (resulting in a FoV of 4096×512) offer a spectral coverage of $\lambda/70$ for each CRIRES-VLT wavelength settings. Using the 0.″2 slit and MACAO, CRIRES-VLT is able to reach an spectral power of ∼100,000.

Its scientific aim is to observe faint objects with higher spatial, spectral, and temporal resolutions. Concerning to sources in transition to PNe and young PN, CRIRES-VLT offers the possibility of studying at high-resolution emission lines (atomic and molecular), silicates and PAHs detected in the near-IR photometric bands, as well as the opportunity of resolve structures related with these emission lines (e.g. disks and outflows).

---

[1]For the maximum likelihood algorithm the minimum number of iterations are systematically lower (>5), while for the Richardson-Lucy algorithm the iterations ranges from 10 up to 30, depending on the quality of the raw image.
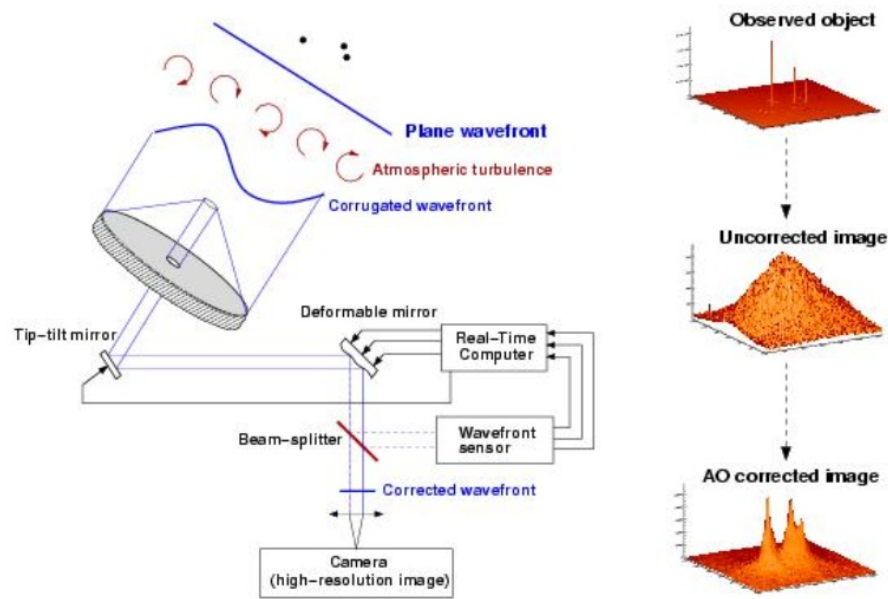
Figure 2.7 Sketch of the adaptive optics principle to correct the wavefront received by the detector. Adapted from CRIRES-VLT ESO user manual.

2.4.1.   Adaptive Optics

Adaptive optics (AO) systems are used to correct the effects suffered by the wavefront (WF) of the light passing through the atmosphere. In addition to the blurring caused by the atmospheric turbulence, there are inhomogeneities in the atmospheric temperature that induce temporal and spatial fluctuations in the optical path leading to a corrugated WF.

The technique named "Adaptive optic" is used to correct in real-time these WF deformations, that is, during the execution of the observations (Figure 2.7). For this purpose, a deformable mirror (DM) is used and is controlled by a real-time computer (RTC) that receives the measurements of a wavefront sensor (WFS) to compensate the WF deformations. This RTC controls a set of piezoelectric actuators mounted on the back of the mirror, pushing and pulling the DM as long as it is necessary. Thanks to the use of DM, the inward WF is flattened while the WFS measures the residual WF error, which is used to deform and correct the next incoming WF. Whenever an AO system uses this residual WF error previously calculated is said to be operating with a"closed-loop".

2.4.2.   Observations and analysis

For CRIRES-VLT, the mid-IR background imposes a sensitivity limitation over the K-, L, and M-bands. At wavelengths shorter than 2.2 μm, the background emission of the sky is dominated by OH lines, whereas at longer wavelengths this background is dominated by sky and telescope emission. To remove this background contamination CRIRES-VLT uses the nodding technique. The
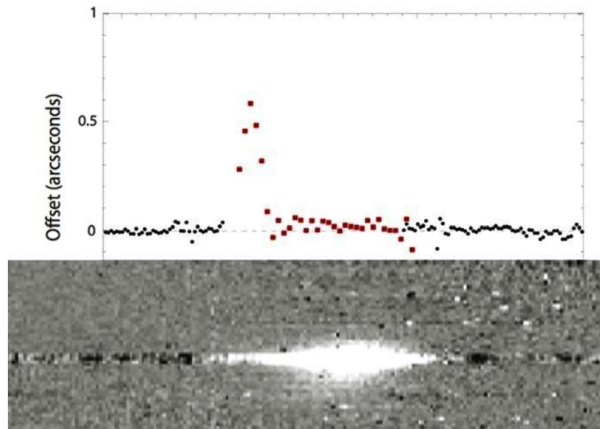
Figure 2.8 T Tauri star and a jet detected in the Paβ line after the spectro-astrometric analysis (Whelan et al. 2004).

first nodding position is acquired and the telescope is moved subsequently to the nodding position B to acquire the next spectrum. The subtraction of the nodding positions A and B results in a spectrum (hereafter refereed as "science spectrum") in which the sky contribution is removed. CRIRES-VLT offers different observing templates and the nodding cycles and throw are free observing parameters.

Jittering is used to correct for bad pixels, this means that the position of the telescope between exposures is slightly shifted (typically of few arcsecs, 2 - 3″ for our CRIRES-VLT observations). In near-IR spectroscopy, observations of standard stars near to the field of the science spectrum and executed soon before or after this science observation are used for telluric correction. This telluric lines are produced by the atmosphere of the Earth. The selection of the telluric standard star also depends on the emission lines of interest, that is, for the sources in transition to PNe, it is recommendable to avoid B stars if hydrogen lines will be studied, since they present important emission of H and He lines. Cooler stars, such late-type and G stars are the most suitable in this cases. The spectrum of the telluric standard star is collapsed and afterwards used to divide the science spectrum.

2.4.3.   The spectro-astrometry technique

As mentioned in the chapter 1 (§1.2) the search and characterization of disks, proposed to be the basic shaping agent of the most asymmetric post-AGB sources and young PNe, demands high-resolution mid-IR and radio observations. The origin and characteristics of these disks are under intense debate because such compact structures lie into cores embedded in dust that mostly dissipates during the short transition from the AGB star to PN. MIDI-VLTI has achieved super spatial resolutions, but these interferometric observations are challenging and time consuming. Furthermore, they are particularly depending on the models used to interpret the dispersed available baselines which are not always suitably aligned with the orientation of the source on the sky. Finally, the sensitivity of these observations is limited.
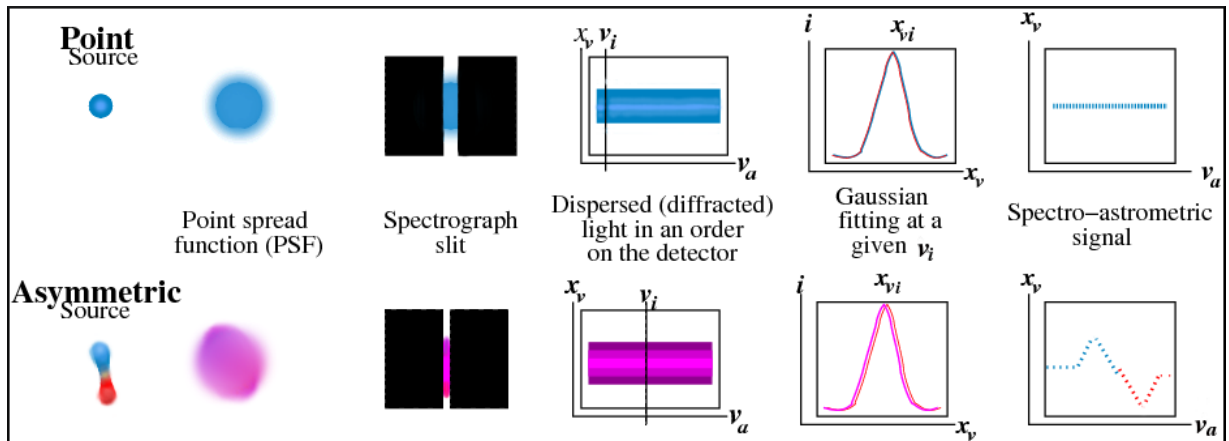
Figure 2.9 The spectro-astrometry technique. *(top)* Dispersed long-slit spectrum of a point source affected by diffraction and optical imperfections. The spectro-astrometric signal does not reveal any offset. *(bottom)* Dispersed long-slit spectrum of a compact bipolar source also affected by the seeing. The source consists of two spatially separated components. For simplicity we assume one lobe moving towards the observer, the other one away. The seeing and optical imperfections smear out this double source into an object resembling an unresolved point source. The plots illustrate the recovery of the spatial signal of the double structure after the spectro-astrometric analysis. Having created a 2-dimensional spectrum, an extraction algorithm is applied. Rather than looking at intensity vs wavelength, the center of gravity of the spectrum in the spatial direction is being recorded. Given sufficient signal to noise ratio in the spectrum, the original spatial structure gives rise to a spectro-astrometric signature. The notation used in this figure is explained in the text, the figure has been adapted from Whelan & García (2008) to the type of sources here studied.

An alternative to overcome the lack of spatial coverage and complex instrumental setup of MIDI-VLTI observations is the use of spectro-astrometric studies using CRIRES-VLT (CRyogenic high-resolution Infra-Red EchelleSpectrograph, Kaeufl et al. 2004). This observational technique has proven its efficiency in the search for close binaries (Bailey 1998; Takami et al. 2001), disks around B[e] stars (Oudmaijer et al. 2008), jets launched by brown dwarfs (Figure 2.8, Whelan et al. 2005), and protoplanetary disks (Pontoppidan et al. 2008; Pontoppidan et al. 2011). In the latter, Keplerian disks traced by the CO ro-vibrational fundamental band at $4.7\,\mu$m with sizes in the range of 60–180 mas (Pontoppidan et al. 2008) have been detected. Therefore, CRIRES-VLT spectro-astrometry opens a new window in the search of compact structures in which high spatial resolution is crucial.

The spectro-astrometry technique takes advantage of high-resolution spectral observations to resolve spatial details at mas scales by basically using the stellar continuum outside the spectral features as the astrometric reference. By using and adaptive optics module, CRIRES-VLT allows to push the spatial resolution limit even further while rejecting artifacts which have been reported from applications of the technique to data from seeing limited instrumentation. This technique is very attractive. Using a single telescope with a standard instrumental setup it can retrieve spatial information on scales that normally require interferometric observations.

The spectro-astrometric analysis recovers the centroid of the flux along the spatial axis (x_v) of

the dispersed spectrum (Figure 2.9). Since a Gaussian function is a suitable approximation to the point spread function (PSF) of the dispersed spectrum, a Gaussian fitting is used to calculate the centroid of the signal and derive its offset (Stone 1989). Once the centroid at a certain velocity (v_i) has been computed, the offsets in the wavelength range (v_a) of interest can be traced along the spatial direction (x) without the dilution provoked by diffraction and optical imperfections. This result is the spectro-astrometric signature. The true spatial offset of a line may be more extended due to the drag induced to its centroid by the continuum emission. The drag depends on the relative intensities of the line and continuum. In this work we have adopted the formulation of (Pontoppidan et al. 2008) to derive and correct these effects on the spectro-astrometric signature, such that the corrected offset is computed as:

$$X_{vi} = x_{vi} \times (1 + F_c(v)/F_l(v)) \tag{2.10}$$

where X_{vi} is the corrected offset, x_{vi} is the measured offset obtained by the Gaussian fitting, and F_c and F_l are the continuum and line fluxes, respectively.

Figure 2.9 illustrates how the spectro-astrometry technique works over two different sources, a point source and a compact bipolar source, both blurred by diffraction. The compact structures of order of mas, such as the bipolar lobes, are embedded within the dispersed spectrum. The spectro-astrometric signature does not show any spatial offsets for a truly point-like source, independently of the position angle (PA) of the slit. If the source has spectral signatures correlated with spatial coordinates a spectro-astrometric signature arises and can vary with the slit PA. A physical structure tilted with respect to the plane of the sky and aligned along the slit will result in maximal spectro-astrometric signature, but the oriented across the slit will produce a minimal signature or no signature will be detected, depending again on its inclination. Consequently, different source geometries and models can be distinguished on scales typically as small as 1/100th of the telescope diffraction pattern.

While spectro-astrometry can reveal the existence of spatial structures down to small fractions of a pixel, it is necessary to keep in mind that a spatial structure can not be derived directly. A proper model fitting is mandatory to draw firm conclusions, considering also that a more than one solution is possible.

Bibliography

Alloin, D., Pantin, E., Lagage, P. O., & Granato, G. L. 2000. 0.6 resolution images at 11 and 20 mu m of the active galactic nucleus in NGC 1068, A&A, 363, 926

Bailey, J. A. 1998. Spectroastrometry: a new approach to astronomy on small spatial scales, SPIE, 3355, 932

Kaeufl, H.-U., Ballester, P., Biereichel, P., et al. 2004. CRIRES: a high-resolution infrared spectrograph for ESO's VLT, SPIE, 5492, 1218

Kwok, S. 2004. The synthesis of organic and inorganic compounds in evolved stars, Nature, 430, 985

Lagage, P. O., Pel, J. W., Authier, M., et al. 2004. Successful Commissioning of VISIR: The Mid-Infrared VLT Instrument, The Messenger, 117, 12

Lucy, L. B. 1974. An iterative technique for the rectification of observed distributions, Aj, 79, 745

Oudmaijer, R. D., Parr, A. M., Baines, D., & Porter, J. M. 2008. Sub-milliarcsecond precision spectro-astrometry of Be stars, A&A, 489, 627

Pontoppidan, K. M., Blake, G. A., van Dishoeck, E. F., et al. 2008. Spectroastrometric Imaging of Molecular Gas within Protoplanetary Disk Gaps, ApJ, 684, 1323

Pontoppidan, K. M., Blake, G. A., & Smette, A. 2011. The Structure and Dynamics of Molecular Gas in Planet-forming Zones: A CRIRES Spectro-astrometric Survey, ApJ, 733, 84

Richardson, W. H. 1972. Bayesian-Based Iterative Method of Image Restoration, Journal of the Optical Society of America (1917-1983), 62, 55

Stone, R. C. 1989. A comparison of digital centering algorithms, AJ, 97, 1227

Takami, M., Bailey, J., Gledhill, T. M., Chrysostomou, A., & Hough, J. H. 2001. Circumstellar structure of RU Lupi down to au scales, MNRAS, 323, 177

Whelan, E. T., Ray, T. P., & Davis, C. J. 2004. Paschen beta emission as a tracer of outflow activity from T-Tauri stars, as compared to optical forbidden emission, A&A, 417, 247

Whelan, E. T., Ray, T. P., Bacciotti, F., et al. 2005. A resolved outflow of matter from a brown dwarf, Nature, 435, 652

Whelan, E., & Garcia, P. 2008. Spectro-astrometry: The Method, its Limitations, and Applications, Jets from Young Stars II, 742, 123

3

Motivation and aims

3.1. Motivation: observational successes and limitations

As was mentioned in chapters 1 and 2, the study of the origins of the shaping of asymmetrical PNe represents an observational challenge, since it is widely believed that the onset of asymmetries reckon on jets launched by disks arising in compact sources in transition to the PN phase. The diffracted limited imaging in conjunction with robust deconvolution algorithms have unveiled valuable morphological characteristics in several astrophysical objects, including PNe and sources in transition to this phase. Meanwhile, spectroscopic observations disclose physical conditions and structures that play an important role in the shaping of asymmetries.

On the other hand, interferometry with the VLTI has proven the existence of disks and torii at the center of PNe, and is the only long-baseline interferometer available for the near- and mid-IR. Despite of that, VLTI has limitations regarding to the sensitivity of the targets and the useful baselines using the 1.8 m auxiliary telescopes (ATs) instead of the 8 m UTs. ATs offer more baselines compared with those offered by the UTs, but the use of these smaller telescopes implies sensitivity losses. Furthermore, in the case of MIDI-VLTI, where only two UTs are used to build the baseline, the lack of closure phase prevent the reconstruction of images. Also, the interpretation of the results is considerably constrained by the model used.

Furthermore, the most powerful interferometers operate at radio frequencies, and the resolution achieved in these studies has proven to be crucial to resolve the innermost structures of post-AGB objects and PNe. However, in the search of the shaping mechanism of PN, the observation of dust as well as molecules whose emission is detected at IR wavelengths are essential too.

In this regards, Figure 3.1 exemplify three cases in which the use of high-resolution techniques are mandatory. Ground-based images obtained with the Near-Infrared Camera Spectrometer (NICS) of the 3.58 m Telescopio Nazionale Galileo (TNG) at the Observatorio Roque de los Muchachos (ORM) disclosed extended emission of the post-AGB candidate IRAS 15534-5422, but was not resolved
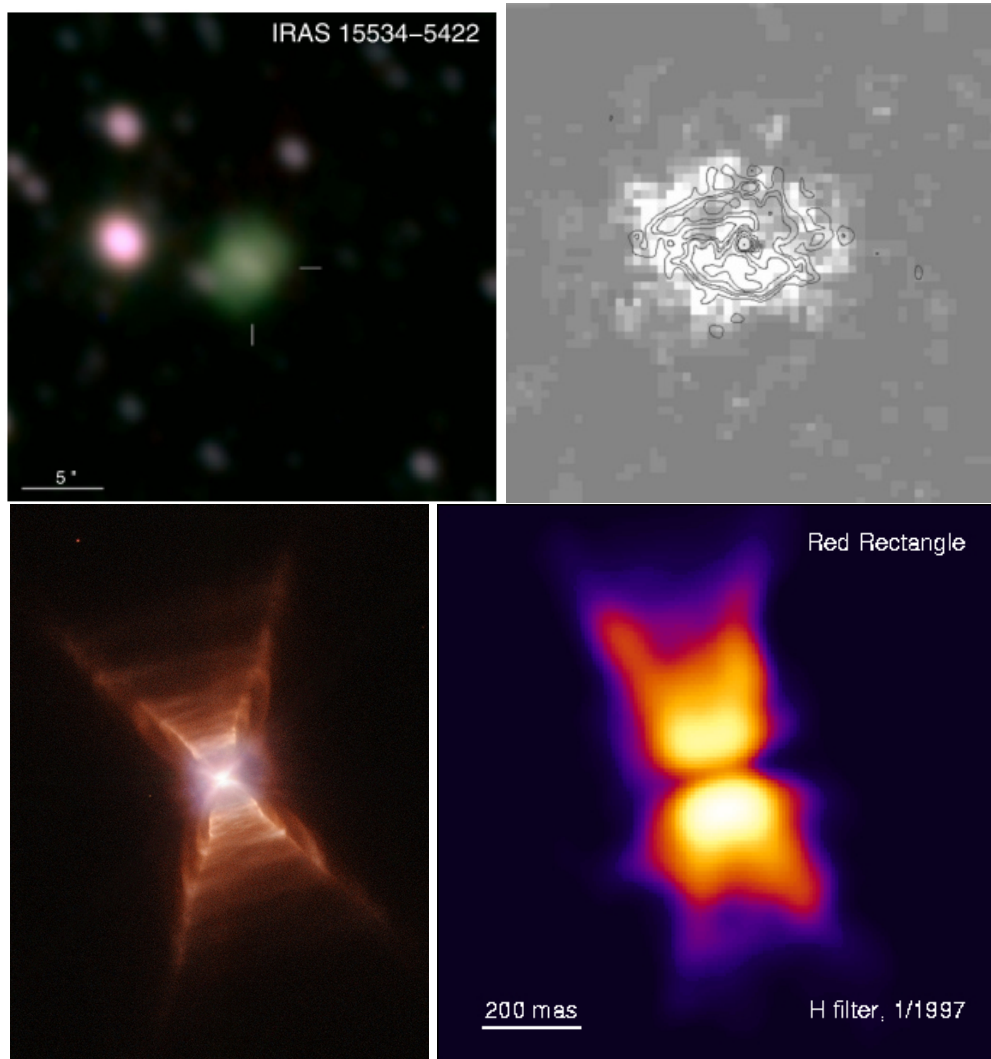
Figure 3.1 (*Upper left*) RGB composite image of IRAS 15534-5422, H_2 (red), Brγ (green), and $K_{continuum}$ (blue) as seen by NICS-TNG (Ramos-Larios et al. 2012.). (*Upper right*) *HST* image of the young PN SwSt 1 (FoV $\sim 2''\!.6$, De Marco et al. 2001). (*Bottom*) HST image of the proto-PN AFGL 915 (total extent $\sim 1'$, Koning et al. 2011) and H-band image reconstructed by biespectrum speckle interferometry (Men'shchikov et al. 1998).

(Ramos-Larios et al. 2012). Even the *HST* has limitations, as shown by the young and compact PN SwSt 1, from which a toroidal morphology has been suggested after the deconvolution of the Hβ *HST* image. Regarding to the enigmatic proto-PN AFGL 915, biespectrum speckle interferometry performed with the ESO-MPG 2.2 m telescope in Chile has outlined the innermost region of AFGL 915 with the high-resolution of $\sim$70 mas in the near-IR H- and K-bands (Men'shchikov et al. 1998), nevertheless, the obscured equatorial region remains unresolved. Moreover, the presence of an equatorial Keplerian rotating gaseous CO disk of $\sim$2 $''$ in AFGL 915 was revealed by the Plateau de Bure Interferometer (Bujarrabal et al. 2005) and these observations are consistent with the preliminary analysis of ALMA (the Atacama Large Millimeter/submillimeter Array) observations (Bujarrabal et al. 2013). Whereas such disk is certainly associated to the collimated agent of AFGL 915, its large size makes unfeasible to learn about the details of the collimation processes in this proto-PN.

3.2. Aims

Inspired by these successful observational results as well as by the observational limitations, the present thesis aims to prove the use of imaging and spectroscopic high-resolution observational techniques in the near- and mid-IR to further resolve and investigate the morphological characteristics in the compact innermost regions of post-AGBs, proto-PNe and young PNe. The main objectives of this thesis are listed in the following lines.

- **Acquisition of VLT IR data**. Firstly, the sources subject to study in this thesis are strong IR emitters post-AGBs, proto-PNe, and young PNe with prominent asymmetries or whose morphologies were not previously resolved at these wavelengths. These sources are usually compact, with total angular extents of a few arcseconds or even with subsecond sizes. In addition to the atomic line emission, they may present molecular emission, silicates and PAHs features as well as dust emission. Given the characteristics of these sources we propose the use of two new generation VLT instruments operating at near- and mid-IR wavelengths: VISIR-VLT for high-resolution imaging and CRIRES-VLT to test high resolution spectro-astrometry.

- **Improvement of mid-IR images to investigate morphological and physical properties of PNe and sources in transition to this phase.** Deconvolution algorithms will be used to enhance the morphological characteristics observed in the nearly diffracted limited VISIR-VLT mid-IR images. Also, we aim to build color (temperature) and optical depth maps to assess the temperature distribution of the structural components detected as well as its optical depth. For this purpose we will acquire the N- and Q-band narrow-band images required to this kind of analysis.

- **Analysis of high-resolution near-IR spectroscopic data to resolve the innermost regions of proto-PNe and young PNe.** We will explore the spectro-astrometry technique

at high-resolution requesting observing time with CRIRES-VLT. This technique will be applied for the first time in the search of disks and other compact structures at the innermost regions of proto-PNe and PNe.

- **Investigate the origin of the asymmetries in PNe.** We will use these imaging and spectroscopic results to investigate the origin of asymmetries in PNe, the spatial distribution of the atomic and molecular gas, and thermal dust in these late phases of low- and intermediate-mass stars. The high-resolution data obtained and analysed in this thesis will be used to complement previous results performed with other techniques, whether at high-resolution or with poorer resolution. Finally, we expect to investigate the link between disks/torii and the outflows/jets suggested as fundamental components to sculpt asymmetric PNe.

Bibliography

Bujarrabal, V., Castro-Carrizo, A., Alcolea, J., & Neri, R. 2005. The orbiting gas disk in the Red Rectangle, 441, 1031

Bujarrabal, V., Castro-Carrizo, A., Alcolea, J., et al. 2013. ALMA observations of the Red Rectangle, a preliminary analysis, A&A, 557, L11

De Marco, O., Crowther, P. A., Barlow, M. J., Clayton, G. C., & de Koter, A. 2001. SwSt 1: an O-rich planetary nebula around a C-rich central star, MNRAS, 328, 527

Koning, N., Kwok, S., & Steffen, W. 2011. Morphology of the Red Rectangle Proto-planetary Nebula, ApJ, 740, 27

Men'shchikov, A. B., Balega, Y. Y., Osterbart, R., & Weigelt, G. 1998. High-resolution bispectrum speckle interferometry and two-dimensional radiative transfer modeling of the Red Rectangle, New Astronomy, 3, 601

Ramos-Larios, G., Guerrero, M. A., Suárez, O., Miranda, L. F., & Gómez, J. F. 2012. Searching for heavily obscured post-AGB stars and planetary nebulae. II. Near-IR observations of IRAS sources, A&A, 545, A20

4

VISIR-VLT study of the extended emission of four obscured post-AGB stars

In this chapter we present the mid-IR VISIR-VLT high angular resolution observations of four heavily obscured sources adapted from Blanco Cárdenas et al. 2013a (A&A 551, A54). The images have been used to describe their morphologies, to analyze their innermost structures, and to derive color (temperature) and optical depth maps.

4.1. Heavily obscured post-AGB stars

Evolved low- and intermediate-mass stars ($0.8M_\odot < M < 8M_\odot$) undergo heavy mass-loss episodes during the red giant and asymptotic giant branch (AGB) phases. At the tip of the AGB, these stars will eject most of their stellar envelopes in a short time until they evolve into post-AGB stars, the immediate precursors of planetary nebulae (PNe). PNe display an impressive variety of morphologies, from spherical to the most complex shapes: bipolars and multipolars with point-symmetric structures and collimated jets moving at high velocities. It has been suggested that asymmetric PNe are the rule, rather than the exception (Manchado et al. 2000; Schwarz et al. 1993). The shaping mechanism of complex PNe is a matter of intense debate and has not been completely understood Balick & Frank (2002).

It has been claimed that the short transition between the AGB and post-AGB phase contains the clues to understanding the transformation of the spherical stellar envelope into an asymmetric PN (Sahai & Trauger 1998). AGB stars are surrounded by thick and compact circumstellar envelopes that are rich in dust and this makes their detection almost impossible at optical wavelengths, whereas their infrared emission is strong. As they evolve into the post-AGB phase, the temperature of the stellar cores increases and the envelopes become optically thin, although it must be noted that it can be found sources at this stage and even young PNe that are significantly obscured because they preserve optically thick envelopes (e.g., IRAS 17347−3139, de Gregorio-Monsalvo et al. 2004). Observational studies of the reflection, thermal dust, and ionized emission around proto-PNe and young PNe
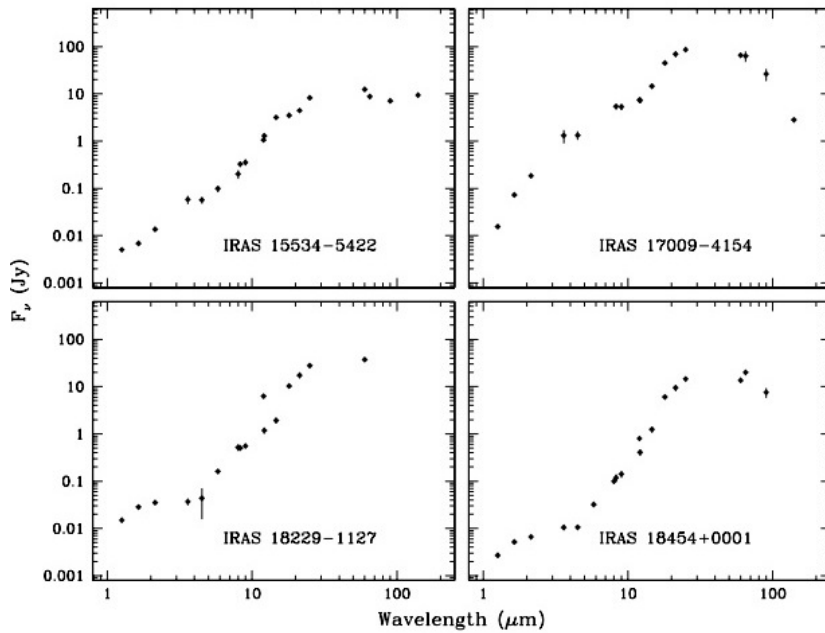
Figure 4.1 Near- and mid-IR spectral energy distributions (SEDs) of the sources in our sample. See RL09 and RL12 for further details on the different datasets used to build these SEDs.

(Sahai & Trauger 1998; Sahai et al. 2007; Ueta et al. 2000; Lagadec et al. 2011; Sahai et al. 2011) *typically detect* the existence of extreme axisymmetric morphologies, with highly collimated bipolar lobes and equatorial rings or torii. On the other hand, spherical and elliptical morphologies seem to be rare among the objects in this transition phase.

Infrared surveys (e.g., 2MASS, *IRAS*, and *AKARI*) have contributed to the study of objects in the late AGB and early post-AGB stages, providing the first insights into this short transition phase (e.g., García-Lario et al. 1997; Jiménez-Esteban et al. 2006; Cox et al. 2011). Recently, Ramos-Larios et al. (2009, 2012), hereafter RL09 and RL12, respectively, have investigated a sample of heavily obscured post-AGB and PNe candidates selected according to their *IRAS* colors and the lack of an optical counterpart (Suárez et al. 2006) using near-IR *JHK* and *Spitzer* IRAC GLIMPSE images, and *MSX*, *AKARI*, and *IRAS* photometric data. RL09 and RL12 have gathered a small sample of four objects that are resolved in *Spitzer* IRAC GLIMPSE images, namely IRAS 15534−5422, IRAS 17009−4154, IRAS 18229−1127, and IRAS 18454+0001. The spatial resolution of these images (∼2″), however, is not adequate to investigate the angularly small structures typical of sources in these evolutionary phases (Suárez et al. 2011; Lagadec et al. 2011). Mid-IR observations using the new generation of ground-based telescopes provide a unique opportunity to resolve the extended emission detected in these four highly obscured post-AGB objects in their transition to the PN phase.

4.2.   The sample

RL09 and RL12 report the detection of extended emission in *Spitzer* IRAC images of four post-AGB source candidates, namely IRAS 15534−5422, IRAS 17009−4154, IRAS 18229−1127, and IRAS 18454+0001 (hereafter also referred as I15534, I17009, and so on). According to the spectral energy distribution (SED) classification scheme of post-AGB sources introduced by Van Der Veen et al. (1998) these four sources shown in Figure 4.1 can be assigned to Type II for I15534 (peak at ∼25 μm and gradual fall-off to shorter wavelengths, although we note that its SED also suggests a near-IR excess at 2–5 μm), to Type III for both I18229 and I18454 (peak at ∼25 μm and steep fall-off to shorter wavelengths with a plateau between 1 and 4 μm), and to Type IV for I17009 (with a main peak at 25 μm and a secondary peak blue-wards). These SEDs are suggestive of two dust components, cold dust in the thermal IR and hot dust obscuring the central star in the near-IR.

Besides the information provided by RL09 and RL12, there is no detailed study available in the literature for these sources. Based on their *IRAS* colors, I15534 is classified as a PN candidate (Preite-Martinez 1988), as recently confirmed by Parker et al. (2012) by means of spectroscopy, whereas I18454 is classified as a post-AGB star (García-Lario et al. 1997). We note that the *IRAS* selection criteria for these sources (Suárez et al. 2006) may overlap with those of young stellar objects (YSOs), although RL09 note that these four objects are not located near star forming regions and they have also not been classified as YSOs in the literature. The lack of CO line emission in I15534 and I17009 and the detection of narrow (≃0.8 km s^{-1}) CO line emission toward I18454 (Urquhart et al. 2008, RMS Survey) are inconsistent with a YSO nature. Based on the *IRAS* colors of the sample, we can also discard a possible symbiotic star nature, as these have typically values of the *IRAS* [12]−[15] color ∼0.8 (Kenyon et al. 1988), whereas the sources in our sample present values ≥2. Moreover, our sources do not present variability in near-IR observations (RL09 and RL12), so we can disregard an eruptive nature, as for instance in circumstellar shells around luminous blue variable sources (e.g., IRAS 18576+0341, Buemi et al. 2010).

The detection of radio continuum emission in I15534, I17009, and I18454 (Urquhart et al. 2008) confirms that ionization is already present, implying that these three sources may have already entered the PN phase. Indeed, Brγ emission from ionized material has been detected in I15534 (RL12) and in I17009 (Van de Steene et al. 2000). For I15534, this emission is found to be extended and to display a bipolar morphology (RL12). We are thus confident of the PN nature of I15534, I17009, and I18454.

As forI18229, the absence of filamentary diffuse emission in the mid-IR, which is characteristic of YSOs, and the similarities between its SED and that of I18454 can be used as additional arguments for a post-AGB classification.

Table 1. Observation log.

| Object | α | δ | Date of | Integration time | | Standard star | FWHM | | | |
	(J2000.0)		observation	N band (s)	Q band (s)		PAH1 (″)	SiC (″)	[Ne II] (″)	Q1 (″)
IRAS 15534−5422	$15^{h}57^{m}21\!\!\overset{s}{.}11$	$-54°30'46\!\!\overset{''}{.}4$	2011-05-25	600	900	HD 133550	0.28	0.37	0.35	0.46
IRAS 17009−4154	$17^{h}04^{m}29\!\!\overset{s}{.}6$	$-41°58'38\!\!\overset{''}{.}9$	2010-05-24	300	450	HD 163376	0.31	0.36	0.38	0.48
IRAS 18229−1127	$18^{h}25^{m}45\!\!\overset{s}{.}0$	$-11°25'56''$	2010-06-14	600	600	HD 169916	0.34	0.51	0.42	0.49
IRAS 18454+0001	$18^{h}48^{m}01\!\!\overset{s}{.}5$	$+00°04'47''$	2010-06-22	840	1320	HD 168723	0.28	0.35	0.35	0.49

Table 2. Estimated fluxes.

Object	PAH1 (8.54 μm) (mJy)	SiC (11.9 μm) (mJy)	[Ne II] (12.8 μm) (mJy)	Q1 (17.7 μm) (mJy)
IRAS 15534−5422	181.6 ± 0.1	768.5 ± 0.1	1461.9 ± 0.1	1891.9 ± 0.2
IRAS 17009−4154	9054.5 ± 0.5	4212.2 ± 0.1	3280.2 ± 0.2	50674 ± 5
IRAS 18229−1127	659.78 ± 0.02	270.25 ± 0.04	270.79 ± 0.03	4101.8 ± 0.1
IRAS 18454+0001	184.34 ± 0.03	167.61 ± 0.02	225.17 ± 0.03	3096 ± 1

4.3. Observations and data reduction

High angular resolution observations (Program ID: 087.D-0367(A), PI: M.A. Guerrero) were obtained with the mid-IR imager VISIR (Lagage et al. 2004) attached to the Cassegrain focus of Melipal (UT3) at the VLT. The sources have been observed through four different filters, PAH1 (λ_c=8.54 μm, $\Delta\lambda$=0.42 μm), SiC (λ_c=11.85 μm, $\Delta\lambda$=2.34 μm) and [Ne II] (λ_c=12.82 μm, $\Delta\lambda$=0.21 μm) in the N band, and the Q1 filter (λ_c=17.65 μm, $\Delta\lambda$=0.83 μm) in the Q band. The observations of standard stars were performed after every science ObsBlock to correct for PSF artifacts and flux-calibration purposes. The date of observation, the integration time, and the FWHM of the standard star observed subsequently are summarized in Table 1. The pixel scale is $0\!\!\overset{''}{.}075$ and the field of view (FoV) is $19\!\!\overset{''}{.}2 \times 19\!\!\overset{''}{.}2$.

The data were taken using several exposures with short DIT (detector integration time) depending on the flux of the source and the required S/N. The observation mode used was the so-called NORMAL with a perpendicular chop-throw of $8''$. The chopping and nodding standard technique was used to help in the removal of the background signal. In the NORMAL mode used for these observations, all frames taken at a chopping position are added immediately at the end of the exposure, resulting in a data cube of reduced size. The data reduction was carried out following standard procedures of Gasgano-VISIR pipeline (version 3.4.4), in which flat-fielding correction, bad pixel removal, source alignment, and co-addition of frames are executed to produce a combined image for each filter. The resulting FoV is $\leq 8''$.

To improve the spatial resolution of the raw images, we deconvolved each of them using its PSF observation according to two different deconvolution algorithms: maximum likelihood (number of iterations $\geq$5) and Richardson-Lucy (number of iterations$\geq$ 10). The precise algorithm and number of iterations was determined by the quality of the raw image, so that the spatial resolution of the deconvolved image was improved, but no artifacts were introduced. The maximum likelihood algorithm was used to deconvolve the images of I17009, I18229, and I18454, whereas the Richardson-Lucy

algorithm was used for I15534. The final images are presented in Figure 4.2.

The final images have been flux-calibrated using fluxes of the PSF stars (Cohen et al. 1999). For the flux calibration we performed aperture photometry (Table 2). We note that the angular extent of I15534 and I17009 is similar to the final FoV of 8″. Because the background aperture may include emission from these objects, their fluxes listed in Table 2 should be regarded as lower limits of the real fluxes.

4.4. Results

The VISIR-VLT images presented in Figure 4.2 reveal the extended emission from these four sources in unprecedented detail. These images also disclose notable variations among the morphological features shown in images obtained through different filters, which we interpret as related to the spectral features registered by these filters. The emission in the PAH1 filter may include the PAH1 feature at 8.6 μm associated with C-rich dust, as well as thermal continuum emission. The broad SiC filter includes thermal dust emission, silicate features, the PAH2 feature at 11.3 μm, and emission lines such as [Ne II] and [S IV]. The [Ne II] filter is fine-tuned to the [Ne II] emission from ionized gas, but it may also include the contribution from dust emission. Finally, the Q1 filter maps the continuum emission of the thermal dust at 17.7 μm.

Considering that the thermal emission of the dust represents the major contribution to the emission in the mid-IR, we have applied the procedure described by Dayal et at. (1998) and have generated color maps (also known as temperature maps) using pairs of flux calibrated images in different wavelengths for the four objects in our sample (Figure 4.3). This procedure relies on the relation between the intensity of the thermal dust continuum at a given wavelength (I_λ) with the temperature and optical depth under the assumption of the optically thin emission of the warm dust component. Because the extinction produced by cool dust component along the line of sight can be considered as similar at the mid-IR wavelengths of the different filters used in this work, we can further assume that its effects on the ratio maps are negligible. Since variations in the temperature produced by the emission properties of the dust appear as color variations in the maps, the temperature of the dust can be approximated by the following expression:

$$T \approx \frac{1{,}44 \times 10^4 (1/\lambda_2 - 1/\lambda_1)}{ln[(I_{\lambda_1}/I_{\lambda_2})(\lambda_1/\lambda_2)^3]} \text{K} \tag{4.1}$$

where λ_1 and λ_2 are the two wavelengths used for the estimation of the temperature, and I_{λ_1} and I_{λ_2} are the measured intensities at these two wavelengths. This method assumes that the variation in the emissivity (Q) can be represented by a power law ($Q \sim \lambda^{-n}$), and it has been proven to provide a good estimate of the spatial distribution of the cold and warm dust across the source studied (Dayal et al. 1998; Meixner et al. 1999; Ueta et al. 2001; Lagadec et al. 2005), since it is helpful to
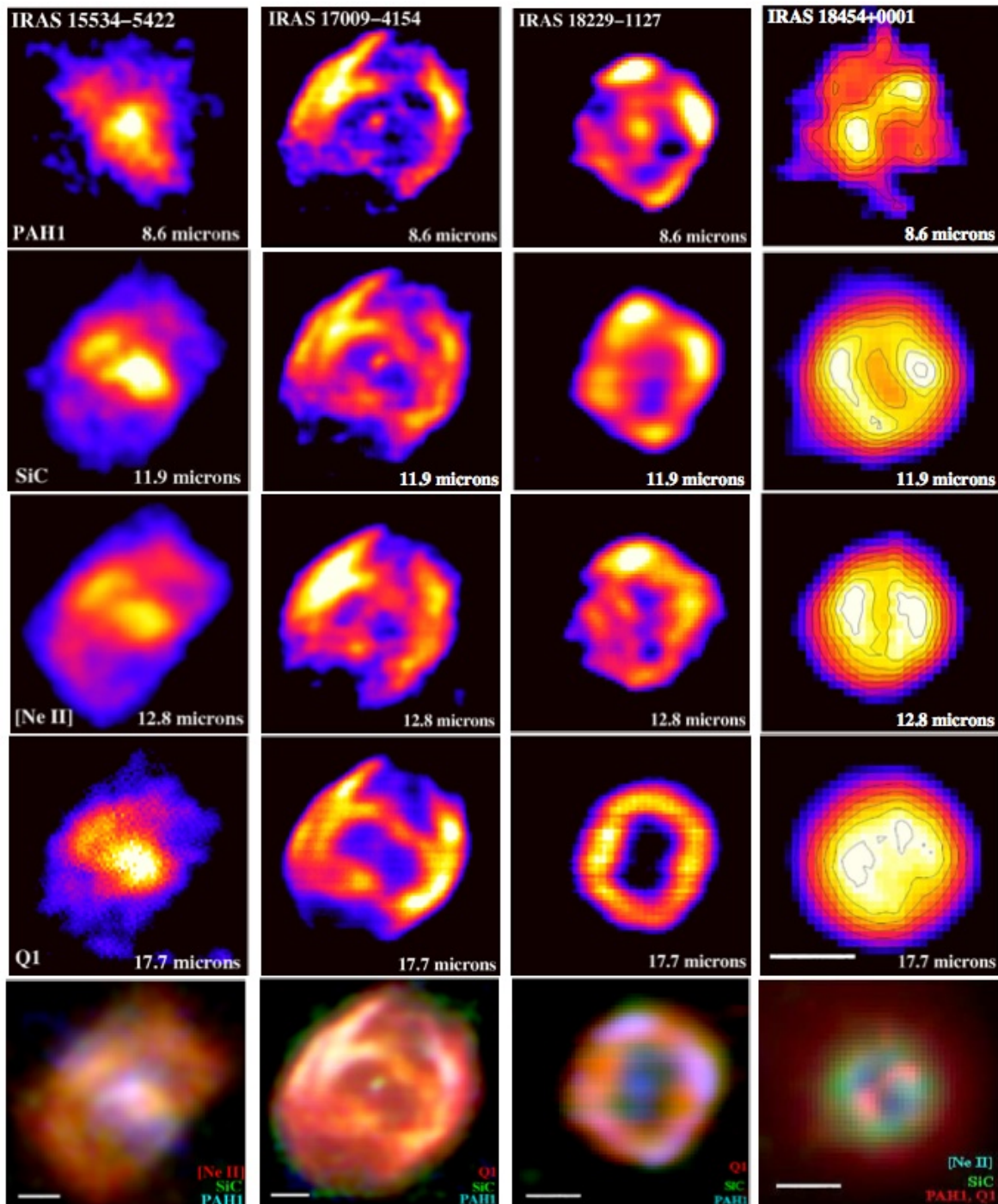
Figure 4.2 Deconvolved VISIR images of the objects in our sample in the different filters observed in the N and Q bands. North is up and east to the left. The images of I18454 are overlaid with contours at 30, 40, 50, 60, 70, 80, 90 and 100 % of the peak intensity to highlight its morphological features.The frames at the bottom are color-composite RGB pictures using the filters with the colors of the corresponding labels. The bar at the bottom of each RGB image and at the bottom of the Q1 image of I18454 represents 1″. The scale of the color-composite picture of I18454 is different from that of the individual images to show in the former the faint halo detected in the Q1 band.

reveal or enhance morphological features.

To derive the color maps shown in Figure 4.3, we used the Q1 image in conjunction with one N-band image, since the longer wavelength range provides a better leverage of the continuum slope that is determined by the thermal dust temperature. We also avoided images in those filters that may present important contributions of spectral features other than the continuum. Therefore, the SiC images were not used, because they may include multiple contributions from emission lines and dust features.

Once the value of the temperature is estimated, we can construct optical depth maps using the Planck function under the same assumption. Therefore, the optical depth at a certain wavelength λ can be derived using the following expression:

$$\tau_\lambda \approx -ln\left[1 - \frac{I_\lambda}{B_\lambda(T)}\right] \tag{4.2}$$

where I_λ is the intensity at the wavelength analyzed. Using these maps, we are able to estimate the column density variations across the nebula to assess whether the emission is optically thin at the observed wavelength range.

We next describe in detail the morphology, temperature, and optical depth properties of the individual sources.

4.4.1.   IRAS 15532-5422

I15534 is resolved in at least two structures that are distinguished by their morphology and emission properties (Figure 4.2). A first structure is an elongated, bar-like feature with a size of $\sim 3''$ oriented at PA 55°. The emission of this bar is detected in PAH, SiC, and Q1, and is much weaker in [Ne II]. A second structure is an arc-like feature, $\sim 5'' \times 3''$ in size, which is oriented perpendicular to the bar and is particularly prominent in [Ne II], but weak in SiC and Q1 and absent in PAH1. This arc-like extended structure is not closed and presents a rectangular shape at low intensity levels. The color composite picture of I15534 (Figure 4.2) suggests that the arc-like feature traces ionized material, while the bar is mostly dominated by thermal dust emission.

The color map of this source (Figure 4.3), obtained using the [Ne II] and the Q1 images, reveals a range of temperatures across the nebula from 80±1 K to 270±1 K, with a mean value of ≈190 K. The color map greatly enhances the arc-like feature, which is the hottest component, whereas the bar, with lower temperatures, almost disappears in this map. The optical depth maps at different wavelengths (Figure 4.4), computed for a mean temperature value of 190 K, imply that the south-west tip of the bar represents the highest density zone in this object. The [Ne II] optical depth map reveals a noticeable enhancement of the column density at the northeast tip of the bar, where it goes across
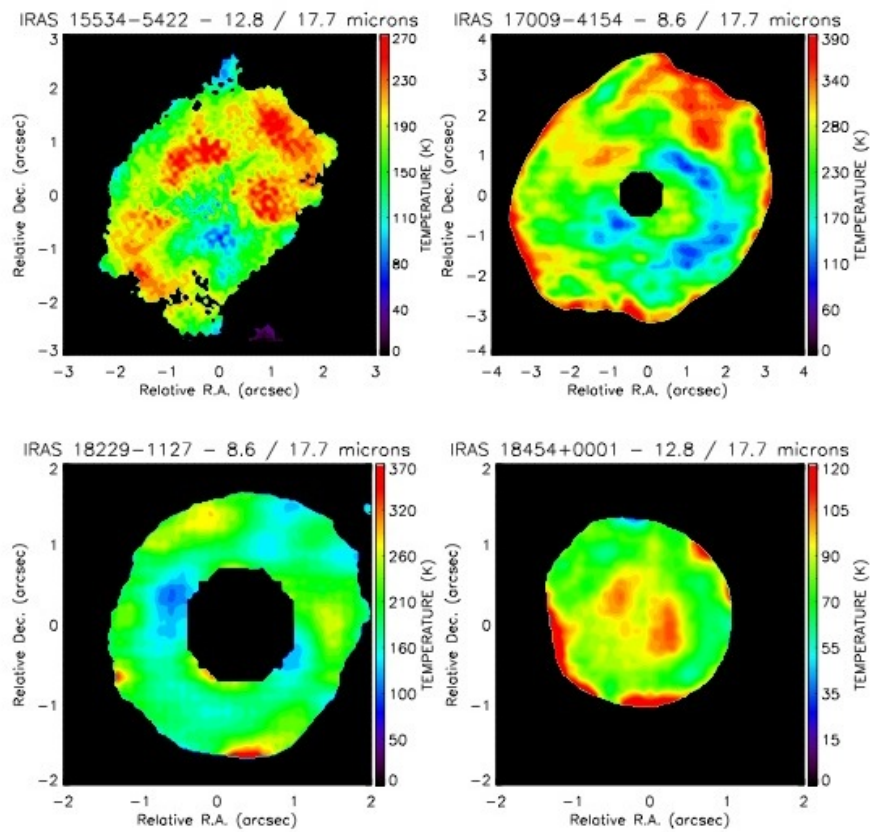
Figure 4.3 Temperature (color) maps derived using the equation 1 of I15534, I17009, I18229 and I18454. We note that the red patches at the borders of the color the maps of I17009 and I18454 are artifacts caused by the reduced S/N ratio in the outermost regions of these sources. The central stars of I17009 and I18229 have been masked to construct the color maps
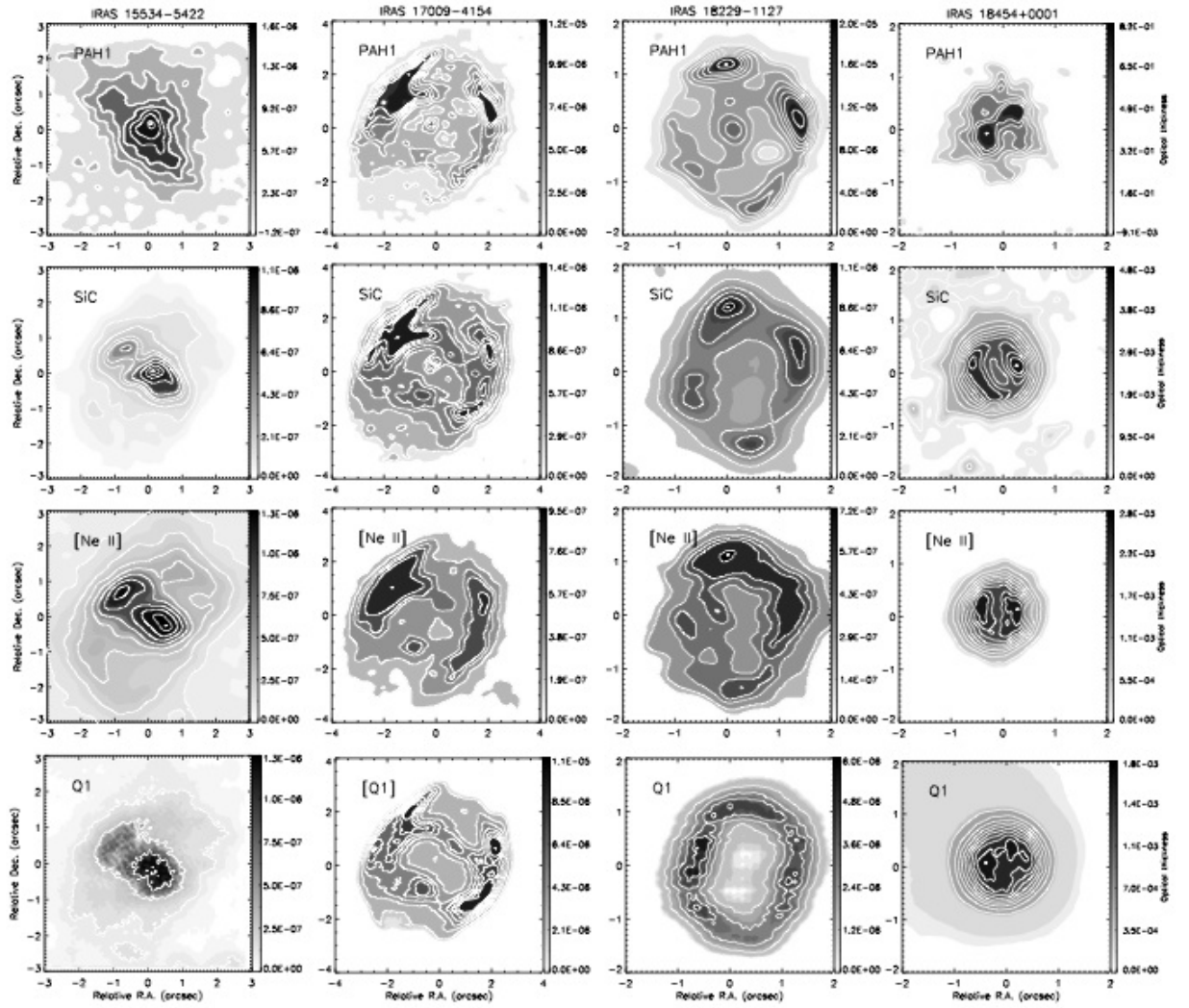
Figure 4.4 Optical depth maps of the sources obtained using equation 2 for the four different wavelengths observed. Contours are in intervals of 10 % of the intensity peak for I17009, I18229, and I18454. For I15534 the contours are in intervals at 10 % for [Ne II] and SiC, intervals at 20 % for Q1, and for the PAH1 map the contours start at 70 % of the intensity in intervals of 2.5 % of the intensity peak.

the arc-like feature.

4.4.2.   IRAS 17009-4154

I17009 has an elongated morphology toward the northwest with a size of $6\rlap{.}''3\times5\rlap{.}''5$. There is an innermost equatorial enhancement that can be appreciated as an elongated ring-like structure ($\sim3''\times2''$) at PA$\sim64°$ surrounding a central star that is detected in all VISIR bands (Figure 4.2). Two prominent arc-like features trace the edge of the outermost regions and are located at PAs $64°$–$244°$ with brightness increasing with wavelength.

The color map of this source (Figure 4.3) shows values of temperature in the range from 150±5 K up to 390±5 K with a mean value of 210 K. The maximum in temperature are related to regions at the tips of the major axis of symmetry. The innermost ring-like structure surrounding the central star seems to have two different temperature components: the southwest is the coolest region (~150 K), whereas there is a hot component located toward northeast with a temperature of ~350 K. The arcs are warmer (~250 K). The mean value of the temperature ($T=210$ K) has been used to derive the optical depth maps of I17009 (Figure 4.4). The regions with the highest column densities are the arcs, followed by the ring-like structure, as shown in all optical depth maps.

4.4.3.   IRAS 18229−1127

IRAS 18229−1127 has a rhomboidal clumpy envelope with an angular size of $2\rlap{.}''5$. In the PAH1, SiC, and [Ne II] N-band images (Figure 4.2), this envelope is dominated by two bright knots toward the north and northwest, and two weaker knots are noticeable toward the south and southeast. The southeast knot is not detected in [Ne II]. Interestingly, these knots are singularly not apparent in the Q1 image that shows a clearly hollow envelope, with an elongated cavity oriented along the north-south direction. The central star is detected, but only in the bluest PAH1 image at 8.6 μm. The color-composite RGB picture of this object at the bottom of Figure 4.2 shows a reddened, hollow rhomboidal envelope with a spot brighter at shorter wavelengths at each corner.

We derived the color map of this source using its PAH1 and Q1 images and estimated a mean temperature of 170 K (Figure 4.3), with a range of 100 K$\leq$ T $\leq$370±1 K. The bright knots in the N-band filters are the warmest regions of this source, with $T \simeq 280$ K, whereas the rest of the rhomboidal envelope has the lowest temperatures (~200 K). The mean value of 170 K has been used to derive the optical depth maps of I18229 (Figure 4.4). The knots represent the regions with the highest densities in the N-band, with the north one the densest. These density variations are diminished in the Q1 optical depth map, where the rhomboidal envelope has a more homogeneous density distribution. The difference between the optical depth maps of the N-band and the one of Q1 is remarkable: while the knots are the densest zones from 8.6 to 12.8 μm, the peak of the density at 17.7 μm is toward the east, where not a single knot is present.

4.5.   Discussion

4.5.1.   Physical structure of the sources

We obtained mid-IR high spatial resolution images of three PNe and one post-AGB source candidate using VISIR at the VLT. These images reveal notable morphological differences among the sources in our sample. The shell-like morphology and detection of a central star in three of these sources are not expected for the diffuse mid-IR emission from compact H II regions (Takahashi et al. 2000). Only I15534 may look like a compact H II region, but its PN nature is well established by optical spectroscopy (Parker et al. 2012).

Temperature and optical depth maps built from these images have been proven to be powerful tools to enhance morphological structures and to reveal new ones in these objects. In the following we discuss the main characteristics of the individual sources, as well as the characteristics that are shared by them all.

I15534 is a young PN with two distinct structural components. The elongated innermost structure is dominated by thermal dust continuum, and it represents the coldest and densest regions in this PN. This structure is surrounded by a warmer, ionized extended envelope of lower density. Whereas the color-composite picture of I15534 in Figure 4.3 seems to imply that the elongated inner structure is a bipolar nebula surrounded by the ring-like envelope, the physical properties of the different components favor an alternative, more solid interpretation. The innermost structure is instead a high-density, dusty "torus", whereas the apparent envelope can be associated to a pair of ionized bipolar lobes perpendicular to that "torus". This interpretation is consistent with the narrow-band near-IR images presented by RL12 and with the near-IR excess noticeable in its SED (Fig. 4.1).

I17009 seems to have an slightly bipolar or elliptical morphology. The bright arcs can be interpreted as ionized bipolar extensions of an elliptical shell sculpted by an SiC and Q1 bright, dusty equatorial ring. The dust ring is the coldest structure in this source, whereas the bright arcs are warmer. The temperature is the highest at the northwest and southeast tips of the lobes.

Based on the properties of the SED of I18229 and on its similarity with that of the PN I18454 (Fig. 4.1), we favor its classification as a post-AGB source and discard a YSO nature. This source shows a peculiar clumpy and dusty rhomboidal envelope. This rhomboidal appearance is enhanced by the knots located toward the northwest, the densest region of this source, and southeast knots. The rhomboidal morphology of I18229 resembles the shape of the PN BD+303639 (Lagadec et al. 2011; Akras & Steffen 2012).

I18454 is a compact PN displaying both a spherical AGB shell and a dusty torus, which are most noticeable in the PAH1 (8.6 μm) and Q1 (17.7 μm) images. The temperature map suggests the

presence of relatively hot regions along the direction perpendicular to this torus. Alternatively, these regions may be dominated by ionized gas unveiled by its [Ne II] emission. The torus shows density enhancements in the dust-dominated PAH1 and Q1 filters corresponding with the high density knots along the southeast and northwest direction. The presence of a high density torus, but a spherical AGB envelope, is intriguing. We might witness in this source the early phase on the shaping of a bipolar PN, before the spherical geometry of the AGB wind is disrupted by a fast stellar wind collimated by a toroidal density enhancement as proposed by the generalized interacting stellar wind model of PN shaping (GISW, Balick et al. 1987).

The morphological features detected in direct images are notably enhanced in the temperature and optical depth maps, because these distinguish between structures of the same brightness, but different physical conditions. Furthermore, the physical characteristics of the structures detected for each source are generally consistent. The innermost dusty rings or torii of I15534, I17009, and I18454 have lower temperatures ($T \sim 100$ K) than the elongated hotter ($T \gtrsim 150$ K) bipolar regions.

The optical depth maps of I15534, I17009, and I18229 peak at similar values for each of these sources. This implies that there are no variations in the density derived from the different filters for each of these sources, and thus that the mid-IR emission of these source is optically thin.

4.5.2.   Comparison with the morphology and physical structure of other evolved objects

Our mid-IR VISIR-VLT images have unveiled a wealth of structural components in the four sources in our sample. In short, these sources can be described as a detached rhomboidal shell (I18229), a spherical shell with strong evidence of a dusty torus orthogonal to an ionized bipolar flow. (I18454), and two mild bipolar or elliptical sources (I15534 and I17009). Unlike other studies of sources in the transition towards the PN phase (Sahai & Trauger 1998; Ueta et al. 2000; Sahai et al. 2007; Sahai et al. 2011; Lagadec et al. 2011), we do not find evidence of extreme axisymmetric bipolar or multipolar morphologies. In this respect, we note that we have not imposed on the sources in our sample any of the restrictions of previous studies, required the sources to be detected in the optical (Ueta et al. 2000; Sahai et al. 2011), or to have fluxes at 12 μm greater than 10 Jy (Lagadec et al. 2011). These selection criteria may have introduced notorious biases in the morphological output of the sample.

In this sense, the lack of restrictive selection criteria in our sample may probe a different population of sources in the transition between the late AGB and early post-AGB phases. The small number of objects in our sample does not allow us to drawn firm conclusions; however, the observed morphologies may be analyzed within the evolutionary context of PN formation. At least three of the sources in our sample (I15534, I17009, and I18454) have already reached the PN stage, although they are still mostly obscured at optical wavelengths. The significant

obscuration can be attributed to large amounts of circumstellar material that has been previously ejected by their central stars, suggesting massive progenitors. Interestingly, the optical depth values computed for I18454 are significantly higher than those of the remaining sources, whereas its temperature is lower. The thicker envelope of this source may be indicative of an even more massive progenitor.

If the sources in our sample indeed descended from massive AGB stars, we do not see the expected correlation between extreme bipolar morphology and massive progenitors (Corradi & Schwarz 1995; Ueta et al. 2000; Siódmiak et al. 2008). It can be argued that the sources in our sample are at a very early evolutionary phase, when asymmetries have not fully developed yet. For example, I15534, with its dense, dusty torus and bipolar lobes, might be a bipolar PN in the making, whereas the high density torus of I18454, enclosed within a spherical shell, can provide the seed for a bipolar PN.

The use of color maps in the mid-IR domain has revealed a torus in IRAS 07134+1005 (Dayal et al. 1998) and hinted at the presence of jets in Roberts 22 and in V Hya (Lagadec et al. 2005). The mid-IR size of these sources ($\sim 4''$) are similar to that of the sources in our sample, but the variations in the temperature across the sources studied in this work have shown structures that define the morphology more clearly. Compared with these previous analyses of color and optical depth maps, our study resolves many more morphological details, especially if we note that the sources in our sample do not display extreme axisymmetric nebulosities. The high-spatial resolution achieved by our data is certainly required to resolve the extended emission of the obscured and small-sized or compact sources transiting this evolutionary phase.

4.6.   Conclusions

We have observed four heavily obscured post-AGB sources and PN candidates with VISIR-VLT in three different N bands (PAH1, SiC, and [Ne II]), and one Q band (Q1). Three sources in our sample (I15534, I17009, and I18454) can be classified as young PNe, whereas only a preliminary classification as a post-AGB source is possible for I18229.

The high-spatial resolution VISIR images were used to investigate the extended emission and to study the spatial variations of the physical conditions (temperature and optical depth) of these sources. We provided evidence of asymmetry in three young PNe: an innermost dust torus or ring embedded within an ionized spherical shell (I18454), and two mild bipolar or elliptical sources with dusty rings (I15534 and I17009).

Compared to previous works, the use of color and optical depth maps have proven very useful in revealing fine structural details in a small sample of heavily obscured sources reaching the PN phase, confirming the usefulness of mid-IR high-resolution observations for the study of this short evolutionary phase.

Our imaging study confirmed that asymmetry is present in heavily obscured post-AGB stars and young PNe but, unlike previous studies focused on these evolutionary phases, no extreme axisymmetric morphologies are found. These previous studies may be biased towards the mid-IR and optical brightest sources, missing critical early phases of the post-AGB evolution of the most massive progenitors. Although based on a small sample, our study may be yielding important clues to the onset of asymmetry in massive progenitors of PNe. Further studies of the most obscured post-AGB sources must be pursued in the future.

Bibliography

Akras, S., & Steffen, W. 2012. Three-dimensional modelling of the collimated bipolar outflows of compact planetary nebulae with Wolf-Rayet-type central stars, MNRAS, 423, 925

Balick, B., & Frank, A. 2002. Shapes and Shaping of Planetary Nebulae, A&AR, 40, 439

Balick, B., Preston, H. L., & Icke, V. 1987. The evolution of planetary nebulae. II - Dynamical evolution of elliptical PNs and collimated outflows, AJ, 94, 1641

Blanco Cárdenas, M. W., Guerrero, M. A., Ramos-Larios, G., et al. 2013. VISIR-VLT high-resolution study of the extended emission of four obscured post-AGB candidates, A&A, 551, A64

Buemi, C. S., Umana, G., Trigilio, C., Leto, P., & Hora, J. L. 2010. VISIR/VLT and VLA Joint Imaging Analysis of the Circumstellar Nebula Around IRAS 18576+0341, ApJ, 721, 1404

Cohen, M., Walker, R. G., & Witteborn, F. C. 1999. Building a Network of Self-Consistent Mid-Infrared Calibration Stars, LPI Contributions, 969, 5

Corradi, R. L. M., & Schwarz, H. E. 1995. Morphological populations of planetary nebulae: which progenitors? I. Comparative properties of bipolar nebulae, A&A, 293, 871

Cox, N. L. J., García-Hernández, D. A., García-Lario, P., & Manchado, A. 2011. Far-infrared Imaging of Post-asymptotic Giant Branch Stars and (Proto)-planetary Nebulae with the AKARI Far-Infrared Surveyor, AJ, 141, 111

David, P., Le Squeren, A. M., & Sivagnanam, P. 1993. An OH Satellite Line Maser Survey of Cool IRAS Sources and Circumstellar Envelope Evolution, A&A, 277, 453

Dayal, A., Hoffmann, W.F., Bieging, J.H. et al. 1998. Mid-Infrared (8–21 Micron) Imaging of Proto–Planetary Nebulae, ApJ, 492, 603

Jiménez-Esteban, F. M., García-Lario, P., Engels, D., & Perea Calderón, J. V. 2006. The O-rich AGB sequence, A&A, 446, 773

de Gregorio-Monsalvo, I., Gómez, Y., Anglada, G., et al. 2004. A Survey for Water Maser Emission toward Planetary Nebulae: New Detection in IRAS 17347-3139, ApJ, 601, 921

García-Lario, P., Manchado, A., Pych, W., & Pottasch, S. R. 1997. Near infrared photometry of IRAS sources with colours like planetary nebulae. III, A&AS, 126, 479

Kenyon, S. J., Fernandez-Castro, T., & Stencel, R. E. 1988. Far-infrared data for symbiotic stars. II - The IRAS survey observations, AJ, 95, 1817

Lagadec, E., Mékarnia, D., de Freitas Pacheco, J. A., & Dougados, C. 2005. Dust temperature and density profiles in the envelopes of AGB and post-AGB carbon stars from mid-infrared observations, A&A, 433, 553

Lagadec, E., Verhoelst, T., Mékarnia, D., et al. 2011. A mid-infrared imaging catalogue of post-asymptotic giant branch stars, MNRAS, 417, 32

Lagage, P. O., Pel, J. W., Authier, M., et al. 2004. Successful Commissioning of VISIR: The Mid-Infrared VLT Instrument, The Messenger, 117, 12

Manchado, A., Villaver, E., Stanghellini, L., & Guerrero, M. A. 2000. The Morphological and Structural Classification of Planetary Nebulae, Asymmetrical Planetary Nebulae II: From Origins to Microstructures, 199, 17

Meixner, M., Ueta, T., Dayal, A., et al. 1999. A Mid-Infrared Imaging Survey of Proto-Planetary Nebulae Candidates, ApJS, 122, 221

Parker, Q. A., Cohen, M., Stupar, M., et al. 2012. Discovery of planetary nebulae using predictive mid-infrared diagnostics, MNRAS, 427, 3016

Preite-Martinez, A. 1988. Possible new planetary nebulae in the IRAS Point Source Catalogue, A&AS, 76, 317

Ramos-Larios, G., Guerrero, M. A., Suárez, O., Miranda, L. F., & Gómez, J. F. 2009. Searching for heavily obscured post-AGB stars and planetary nebulae. I. IRAS candidates with 2MASS PSC counterparts, A&A, 501, 1207

Ramos-Larios, G., Guerrero, M. A., Suárez, O., Miranda, L. F., & Gómez, J. F. 2012. Searching for heavily obscured post-AGB stars and planetary nebulae. II. Near-IR observations of IRAS sources, A&A, 545, A20

Sahai, R., & Trauger, J. T. 1998. Multipolar Bubbles and Jets in Low-Excitation Planetary Nebulae: Toward a New Understanding of the Formation and Shaping of Planetary Nebulae, AJ, 116, 1357

Sahai, R., Morris, M., Sánchez Contreras, C., & Claussen, M. 2007, AJ, 134, 2200

Sahai, R., Morris, M. R., & Villar, G. G. 2011, AJ. Preplanetary Nebulae: A Hubble Space Telescope Imaging Survey and a New Morphological Classification System, 141, 134

Schwarz, H. E., Corradi, R. L. M., & Stanghellini, L. 1993. H alpha Morphological Classification of Planetary Nebulae, Planetary Nebulae, 155, 214

Siódmiak, N., Meixner, M., Ueta, T., et al. 2008. Hubble Space Telescope Snapshot Survey of Post-AGB Objects, ApJ, 677, 382

Suárez, O., García-Lario, P., Manchado, A., et al. 2006. A spectroscopic atlas of post-AGB stars and planetary nebulae selected from the IRAS point source catalogue, A&A, 458, 173

Suárez, O., Lagadec, E., Bendjoya, P., et al. 2011. Water fountains and H2O-PNe as seen by VI-SIR/VLT, Asymmetric Planetary Nebulae 5 conference, held in Bowness-on-Windermere, U.K., 20 - 25 June 2010, A. A. Zijlstra, F. Lykou, I. McDonald, and E. Lagadec, (eds. 2011) Jodrell Bank Centre for Astrophysics

Takahashi, H., Matsuhara, H., Watarai, H., & Matsumoto, T. 2000. [NE II] 12.8 Micron Images of Four Galactic Ultracompact H II Regions: Ionized Neon Abundance as a Tracer of the Ionizing Stars, ApJ 541, 779

Ueta, T., Meixner, M., & Bobrowsky, M. 2000. A Hubble Space Telescope Snapshot Survey of Proto-Planetary Nebula Candidates: Two Types of Axisymmetric Reflection Nebulosities, ApJ, 528, 861

Ueta, T., Meixner, M., Dayal, A., et al. 2001. Discovery of an Extended Dust Emission around IRAS 18576+0341 (AFGL 2298) At 10.3 and 18.0 Microns: A New Luminous Blue Variable Candidate?, ApJ, 548, 1020

Urquhart, J. S., Hoare, M. G., Lumsden, S. L., Oudmaijer, R. D., & Moore, T. J. T. 2008. The RMS survey. 13CO observations of candidate massive YSOs in the northern Galactic plane, Massive Star Formation: Observations Confront Theory, 387, 381

Van de Steene, G. C., van Hoof, P. A. M., & Wood, P. R. 2000. Near-infrared and Brγ observations of post-AGB stars, A&A, 362, 984

van der Veen, W. E. C. J., Habing, H. J., & Geballe, T. R. 1989. A comparison between CO-, OH-, and IR-mass-loss rates of evolved stars, A&A, 226, 108

5

Near- and mid-IR morphology of the H$_2$O planetary nebula K 3-35

This chapter is dedicated to the description of the multiwavelength imaging study of the PN K 3-35 adapted from Blanco Cárdenas et al. 2013b (accepted in A&A, in press) We present new high angular resolution N-band images and narrow- and broad-band near-IR images of K 3-35, complemented with mid-IR spectroscopic observations to analyze and investigate the nature of the structures detected at these wavelengths. The near- and mid-IR images have been compared with high-resolution optical and radio continuum images to gain a better view of a PN in the very first stages of its formation.

5.1. The young water maser emitter PN K 3-35

The study of the youngest asymmetrical PNe is fundamental for a better comprehension of the sculpting processes of the material ejected from these stars in the last phases of their evolution. One of the first sources revealing the link between the disks and collimated outflows is K 3-35, and extremely young PN as indicated by its water maser emission (Miranda et al. 2001). At optical wavelengths, K 3-35 presents bright bipolar lobes split by a prominent dark lane (Miranda et al. 2000; Sahai et al. 2011). The main nebular axis is defined by two bow-shock-like structures $\simeq 6''$ apart oriented along a direction perpendicular to the dark lane. Two bright point-symmetric knots are observed in the bipolar lobes, but the relative orientation of these knots is not coincident with the main nebular axis (Miranda et al. 2000).

Radio observations of K 3-35 have revealed a remarkably different morphology; radio continuum images at 2, 3.6, and 6 cm show a bright precessing bipolar jet emanating from the core and extending up to the bright point-symmetric knots observed at optical wavelengths (Aaquist et al. 1990; Aaquist et. al 93; Miranda et al. 2001) Moreover, observations at 1.3 cm have unveiled the presence of a small disk of radius $\simeq 65$ AU (assuming a distance of 3.9 kpc to K 3-35, Tafoya et al. 2011) traced by water masers at the center of the object (Miranda et al. 2001; Uscanga et al. 2008). The disk is not

totally perpendicular to the main nebular axis of K 3-35, but to the innermost regions of the bipolar jet (Uscanga et al. 2008), suggesting a physical connection between disk and jet. Furthermore, the high degree of circular polarization detected in the 1665 and 1720 MHz OH maser emission indicates that the disk is magnetized (Gómez et al 2009). Water maser emission has also been detected at the tips of the bipolar jet, in spatial coincidence with the bright optical knots (Miranda et al. 2001). The detection of CO and HCO$^+$ from K 3-35 indicates the presence of molecular material (Dayal et al. 1996; Tafoya et al. 2011; Gómez et al. 2008) In particular, the detection of HCO$^+$ reveals the existence of dense neutral regions that could preserve and shield the water molecules in the nebula from the strong UV radiation of the central star, although the spatial correspondence between the HCO$^+$ and water maser emitting regions has not been established so far.

The previous studies of K 3-35 have shown notable discrepancies between the optical and radio continuum morphologies, being almost complementary. While the optical observations trace structures produced by scattered light and ionized gas whose emission is strongly absorbed by dust, the radio continuum observations maps emission from ionized gas at the innermost regions of K 3-35 that eludes the absorption of dust. On the other hand, molecular observations (CO, HCO$^+$) show the existence of neutral material, although the morphology of this component is unknown.

Observations of K 3-35 in the near- and mid-infrared can be used to bridge the optical and radio (continuum and molecular) observations. Near-IR observations provide the first insights into the dust thermal emission, and may also trace both ionized gas (e.g., Brγ line emission) and molecular emission (e.g., H$_2$ emission). In the mid-IR, the N-band is expected to be dominated by thermal dust emission, but important contributions from UIR (unidentified infrared) bands commonly attributed to PAHs (polycyclic aromatic hydrocarbons) may be present. Spectral features from silicates and emission lines of ionized species (e.g., [S IV] $\lambda10.50$ μm, [Ne II] $\lambda12.81$ μm, and [Ar V] $\lambda13.10$ μm) may also be detected in this band (Rinehart et al. 2002).

5.2.   Observations

5.2.1.   Mid-IR observations

High angular resolution observations of K 3-35 were obtained on September 9, 2010 at the UT3 (Melipal) Very Large Telescope (VLT) using the VLT Imager and Spectrometer for mid InfraRed (VISIR, Lagage et al. 2004) during the observing program 085.D-0256(A). Near-diffraction images (FWHM$\sim0\rlap{.}''3$) have been acquired in the so-called NORMAL observing mode in three different N-band filters: PAH1 ($\lambda_c = 8.54$ μm, half band width HBW = 0.42 μm), [S IV] ($\lambda_c = 10.49$ μm, HBW = 0.16 μm), and SiC ($\lambda_c = 11.85$ μm, HBW = 2.34 μm). Chopping and nodding standard techniques were used to remove the background signal with parallel chop-throw of 10$''$. The pixel scale of the detector, a 256$\times$256 pixels DRS (former Boeing) device, is 0$\rlap{.}''$075, resulting in a field of view of 19$\rlap{.}''$2$\times$19$\rlap{.}''$2. An observation of a standard star after every science observation was performed for deconvolution and flux calibration purposes. The data reduction of the raw VISIR data cubes has been performed using

the standard routines provided by the Gasgano pipeline (version 3.4.4.). These routines carry out the flat-field correction, bad pixel removal, source alignment, and co-addition of frames. The final images were deconvolved using a Richardson-Lucy algorithm (Richardson 1972; Lucy 1974) with a number of iterations between 20 and 30 to enhance those morphological features already present in the raw data. The resolution of the deconvolved images is $\simeq 0\rlap{.}''24$, $\simeq 0\rlap{.}''31$, and $\simeq 0\rlap{.}''27$ in the PAH, [S IV], and SiC filters, respectively.

5.2.2. Broad-band near-IR observations

Broad-band J, H and K_s images of K 3-35 were obtained on June 28, 2010 using the Long-Slit Intermediate Resolution Infrared Spectrograph (LIRIS, Acosta-Pulido et al. 2003) attached at the Cassegrain focus of the 4.2m William Herschel Telescope (WHT) of the ORM (Observatorio de El Roque de los Muchachos, La Palma, Spain). The detector was a HAWAII array with a plate scale of $0\rlap{.}''25\,\mathrm{pixel}^{-1}$ and a $4\rlap{.}'7 \times 4\rlap{.}'7$ field of view. The data were reduced using the dedicated software LIRISDR (LIRIS Data Reduction package), a pipeline for the automatic reduction of near-IR data developed within the IRAF environment. The reduction by LIRISDR includes standard and additional non-standard steps, such as bad pixel mapping, cross-talk correction, flat-fielding, sky subtraction, removal of reset anomaly effect, field distortion correction, and final image shift and co-addition. The angular resolution achieved by these observations is $\simeq 0\rlap{.}''7$.

5.2.3. Narrow-band near-IR observations

Narrow-band near-IR images of K 3-35 were obtained on September 19, 2003 with the Near-Infrared Camera Spectrometer (NICS) attached to the Telescopio Nazionale Galileo (TNG) at the ORM and were used by Miranda et al. (2007) for a preliminary analysis of the near-IR morphology of this object. The detector was a Rockwell HgCdTe Hawaii array with 1024×1024 pixels. We used the Short field camera of NICS which provides a plate scale of $0\rlap{.}''13\,\mathrm{pixels}^{-1}$. Three narrow-band filters in the K band were used: H_2 ($\lambda_0 = 2.122\ \mu$m, FWHM = 0.032 μm), Brγ ($\lambda_0 = 2.169\ \mu$m, FWHM = 0.035 μm), and a continuum filter, K_{cont} ($\lambda_0 = 2.275\ \mu$m, FWHM = 0.039 μm). Several exposures were obtained with the nebula centered in each quadrant of the detector for total exposure times of 1440 s per filter. The data were reduced using standard procedures within the MIDAS package. The angular resolution of the H_2, Brγ, and K_{cont} images is $\simeq 0\rlap{.}''59$, $\simeq 0\rlap{.}''71$, and $\simeq 0\rlap{.}''67$, respectively.
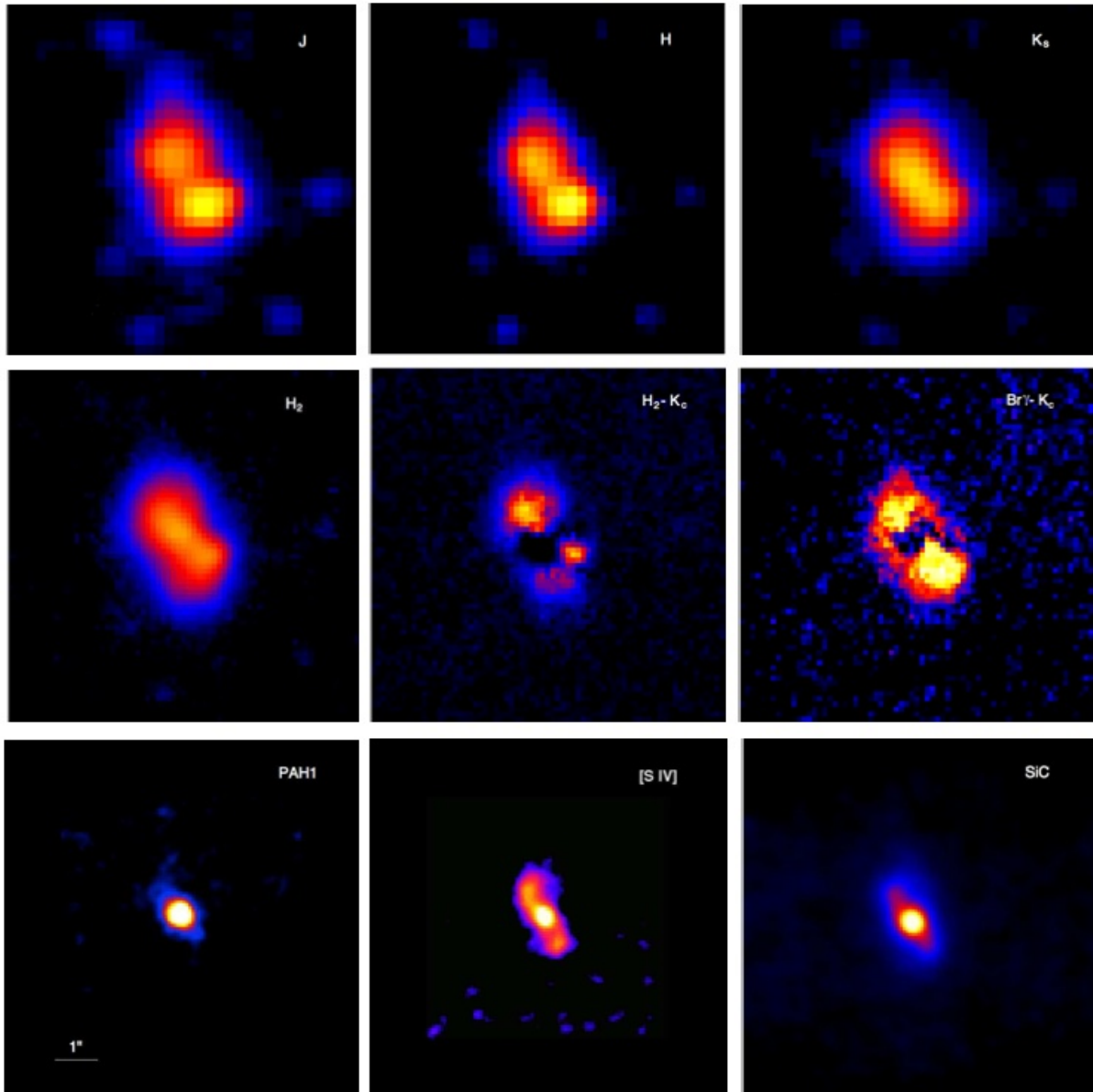
Figure 5.1 Images of K 3-35 from near-IR (WHT LIRIS J, H, and K_c and TNG NICS H_2, H_2–K_{cont}, and Brγ–K_{cont}) to mid-IR (VLT VISIR PAH1 $\lambda 8.6$ μm, [S IV] $\lambda 10.49$ μm, and SiC $\lambda 11.85$ μm). The images are displayed in logarithmic scale to enhance the morphological characteristics. The spatial scale, as is indicated in the PAH1 image, is the same for all images. North is up, east to the left.

5.2.4. *ISO* SWS spectrum

We have used *ISO* (Infrared Space Observatory) spectral processed and normalized data Sloan (2003) from the SWS (Short Wavelength Spectrometer, De Graauw et al. (1996)) available in the *ISO* database. This spectrometer operates between 2.4 and 45 μm with aperture sizes of 14×20 arcsec^2 for λ=2.38−12.1 μm and 20×22 arcsec^2 between λ=12−29 μm. In this paper, we have used data from 8 μm to 14 μm obtained on November 25, 2001 (Proposal ID: SAHAI_1) to investigate the nature of the emission of K 3-35 in the N-band.

Figure 5.2 JHK color composite image of K 3-35 with SiC logarithmic contours overplotted to improve the morphological characteristics of this PN. The SiC image has been degraded to the resolution of the JHK image.

5.3.   Results

We next describe the new images of K 3-35 obtained through narrow- and broad-band near- and mid-IR filters shown in Figure 5.1. To study the multi-wavelength spatial distribution of the emission of K 3-35, we will also use VLA radio continuum data at 3.6 cm from Miranda et al. (2001) and *HST* WFPC2 F658N [N II], F606W R, and F814W I images downloaded from the Mikulski Archive for Space Telescopes (MAST) (Program 9101, P.I.: R. Sahai). This will allow us to emphasize the notable morphological differences and similarities between the nebular emission in the optical, IR, and radio domains.

The emission in the mid-IR N-band is dominated by a bright, compact source at the center of K 3-35 (Figure 5.1, *bottom row*), which will be referred hereafter as to the core of K 3-35. We note that the core of K 3-35 remains unresolved at the spatial resolution of $0\rlap{.}''3$ achieved by the VISIR observations. The intensity of the emission from the innermost regions of K 3-35 increases toward redder wavelengths. Most of the emission detected in the narrow PAH1 filter arises in the core, with very faint extensions detected at PA$\simeq$45°. The broad-band 11.85 μm image reveals additional extended emission that traces narrow and elongated structures emanating from the core and extending up to $sim0\rlap{.}''8$ along PA$\sim$31°. These features are better defined in the image through the [S IV] filter. In this filter, the emission of these two structures is prominent, revealing an S-shape that closely resembles the bipolar precessing jet observed at 3.6 cm radio continuum.

The LIRIS broad-band near-IR images (Figure 5.1, *top row*) disclose contrasting morphologies as they probe emission in the different bands. The spatial distribution of the extended emission in the J and H bands is alike: the emission peaks in two blobs $\sim1\rlap{.}''6$ apart bisected by an obscured region at the equatorial plane of K 3-35. These two blobs correspond with the bright point-symmetric knots detected in optical images. The northeastern blob at PA$\sim$31° is fainter than the southwestern blob at PA$\sim$220°, in contrast with the optical wavelengths that show the northeastern knot to be brighter. Nevertheless, we note a field star overimposed on the southwestern lobe whose contribution to the brightness in the J and H bands of the southwestern lobe may be responsible of this discrepancy.

Very remarkably, the emission in the K_s band peaks at the core of K 3-35. This is in agreement with the emission shown in the N-band images, although at difference with the N-band, the K_s image is not dominated by the emission from the core (see Figures 5.1 and 5.2). We must emphasize that the K_s band marks the shortest wavelength at which the innermost regions of K 3-35 is faintly detected.

The morphology in the K_s image therefore shows structural components seen in the J and H images, as well as those seen in the N-band images, thus reconciling the distinct morphologies observed in the near- and mid-IR.

Very remarkably, the emission in the K_s band peaks at the core of K 3-35. This is in agreement with the emission shown in the N-band images, although at difference with the N-band, the K_s image is not dominated by the emission from the core (see Figs. 5.1 and 5.2). We must emphasize that the K_s band marks the shortest wavelength at which the innermost regions of K 3-35 is faintly detected. The morphology in the K_s image therefore shows structural components seen in the J and H images, as well as those seen in the N-band images, thus reconciling the distinct morphologies observed in the near- and mid-IR.

Figure 5.1 (*middle row*) also presents the narrow-band near-IR images obtained with NICS at the TNG. In particular, we show the H_2 image and the continuum-subtracted H_2–K_c and Brγ–K_{cont} images isolating the molecular and ionized emissions[1]. The H_2 emission appears over the tips and beyond the bipolar blobs observed in the mid-IR images, along an axis oriented at PA$\simeq 27°$ and at angular distances of $\sim 1''1$ from the core of K 3-35. The emission is brighter at the northeastern lobe, as highlighted by the H_2-K_c image. The spatial distribution of the ionized material traced by the Brγ line resembles that described for H_2, but the emission is more extended, it seems to enclose the equatorial region and, contrary to the H_2 emission, it peaks in the southwestern lobe at PA $\sim 215°$. We caution that the contribution from a field star overimposed on the southwestern lobe may alter this conclusion. The northeast peak of the Brγ emission is oriented at PA$\simeq 26°$ and at distance of $\sim 0''8$ from the core, i.e., closer to the core than the corresponding peak of H_2 emission.

The comparison of the IR images with previous high-angular resolution VLA radio continuum maps (Figure 5.3) and *HST* WFPC2 optical observations (Figure 5.4) reveals important spatial coincidences between the different morphological components of K 3-35. The 3.6 cm radio continuum image in Figure 5.3 shows a bright core and extended emission along the S-shaped precessing bipolar jet. The tips of the bipolar jet are spatially coincident with regions of enhanced H_2 emission (Figure 5.3-left), but neither the core nor the collimated outflows themselves are detected in the narrow-band near-IR H_2 or Brγ images; only the K_s band detects the core observed at 3.6 cm (Figure 5.2). On the other hand, there is a close correspondence between the radio 3.6 cm and mid-IR [S IV] images (Figure 5.3-right). At these two wavelengths, the emission from the core is bright, but there is a prominent S-shaped feature that traces the precessing collimated outflow. There is a perfect match between the morphology of this S-shaped feature at 3.6 cm and in the [S IV] filter.

The *HST* RGB composite picture (Figure 5.4), which traces the ionized material detected in

---

[1] The spectral distribution of the core of K 3-35 and that of the stars in the field of view are notably different, and thus those stars could not be used to scale the emission in the continuum filter to that in the line filters. In particular, the star projected on the southwestern lobe is poorly removed in the continuum subtracted images. Furthermore, differences in the PSF of the images (see text) are probably responsible for the apparent circular H_2 emission feature around its core.
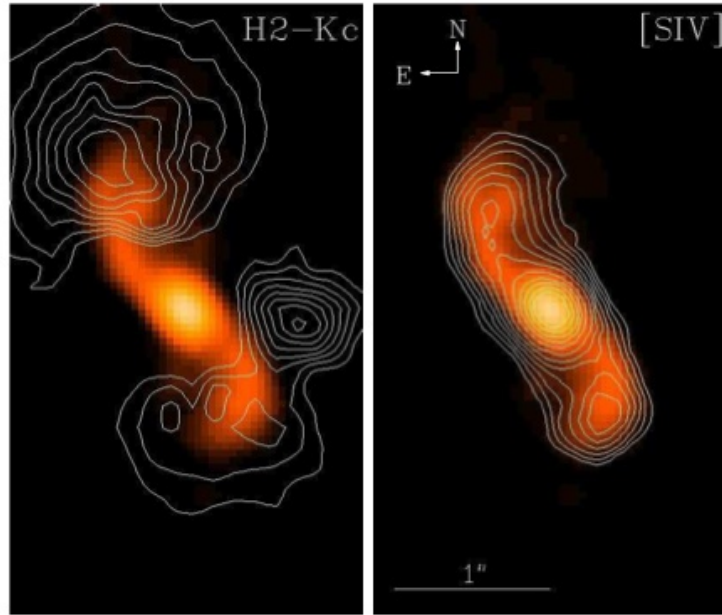
Figure 5.3 VLA 3.6 cm radio continuum image of K 3-35 overplotted by H$_2$–K$_{cont}$ (*left*) and [S IV] (*right*) contours. The spatial scale is indicated in the left panel. The bright point source to the west of the central core in the continuum-subtracted H$_2$ contours at PA∼260° corresponds to a field star not properly subtracted (see text). The contours overplotted are in logarithmic scale to enhance the morphological features detected.

the [N II] filter and very likely by the contribution of the Hα emission line into the bandpass of the F606W *R* filter, shows emission from the bipolar lobes and point-symmetric knots of K 3-35. The bow-shock-like features at the tips of the bipolar lobes, ∼3″ from the core of K 3-35, do not have any counterpart in the radio and IR images described so far. On the contrary, the contours overplotted on Figure 5.4 indicate that the regions of enhanced H$_2$ and Brγ emission and the tips of the jet seen in radio and [S IV] are coincident with the optically bright point-symmetric knots of the bipolar lobes. Therefore, the H$_2$ emission is mostly detected at the tips of the precessing jet, where the [N II] and Brγ emissions also peak.

The *ISO* SWS N-band spectrum is displayed in Figure 5.5. It does not show significant emission in the [S IV] 10.50 μm line nor in the [Ne II] 12.81 μm line, but a continuum emission increasing with wavelength. This continuum emission can be attributed to warm dust. According to Aaquist & Kwok (1989), the IR spectral energy distribution of K 3-35 can be interpreted as a black-body with temperature of 133 K. It is worth noting that the *ISO* spectrum is representative of the bright core and not of the bipolar jet observed mainly in the [S IV] filter.
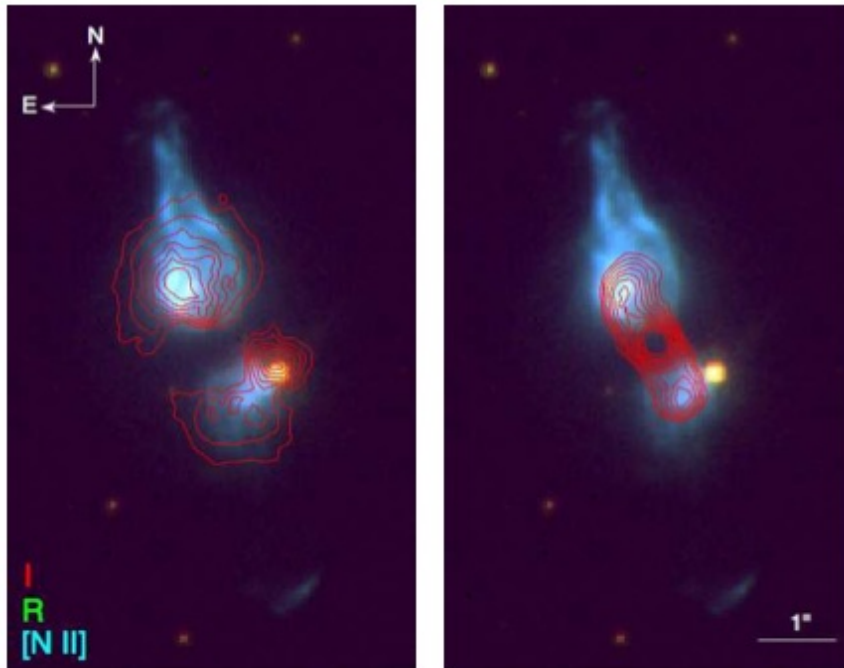
Figure 5.4 Color-composite *HST* WFPC2 picture of K 3-35 (*I*: red, *R*: green, [N II]: blue) overplotted by H_2–K_{cont} (left) and [S IV] (right) contours. The spatial scale is indicated. The contours overplotted to enhance the morphological features are in logarithmic scale. Note that the field of view of this picture is much larger than that of Figure 5.3.
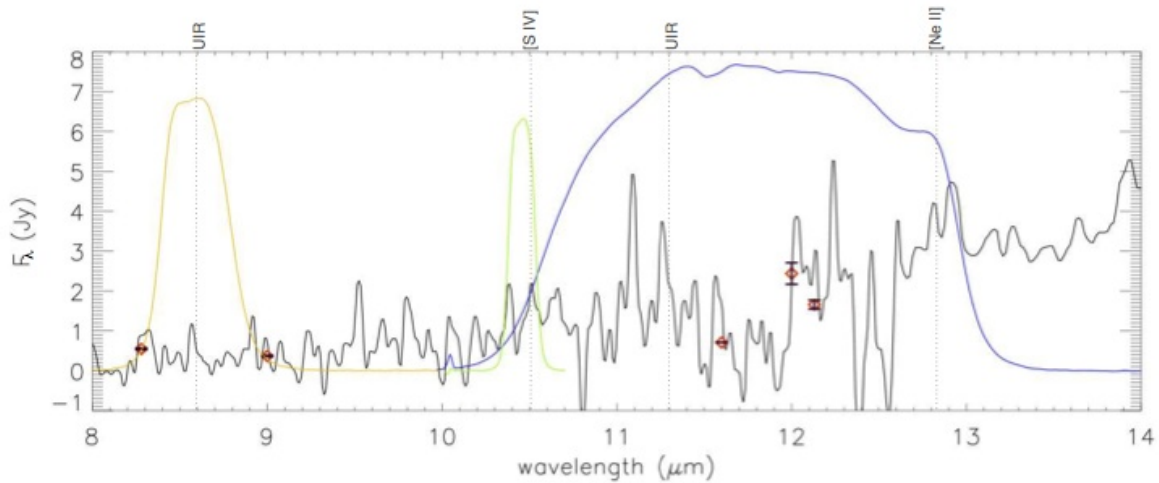
Figure 5.5 N-band *ISO* SWS spectrum of K 3-35 with normalized transmission curves of the VISIR filters used in this work: PAH1 in orange, [S IV] in green, and SiC in blue. Photometric data obtained by different space missions are represented by ◇ signs: *MSX* at 8.28 μm and 12.13 μm, *AKARI* at 9 μm, *IRAS* at 12 μm, and *WISE* at 11.6 μm. The wavelengths of the main features and emission lines in the N-band are labeled and marked by vertical lines.

5.4.   Discussion

The comparison between the near- and mid-IR images, and the VLA 3.6 cm radio continuum and *HST* optical images of K 3-35 is inspiring. The morphology in the broad-band J and H, and narrow-band H_2 and Brγ images is similar to that in the *HST* optical, whereas the mid-IR images are more alike that in the 3.6 cm radio continuum. At this point, the K_s image is key, as it shows morphological features which are common to those observed in the optical and 3.6 cm radio continuum images. We discuss below the morphological components present in the different images and the nature of these emissions.

The core of K 3-35 is a bright feature in the mid-IR VISIR images, with intensity increasing with wavelength in the N-band, whereas it fades towards shorter wavelengths and falls below detection bluewards of the K_s band. This spectral behavior and the presence of a dark lane obscuring the central regions in optical images, imply the presence of warm dust which is detected through its thermal continuum emission. On the other hand, the detection of radio continuum emission from the core indicates the existence of ionized material at the very center of K 3-35. We therefore conclude that the mid-IR emission from the central regions of K 3-35 is thermal emission of dust in a cocoon which embeds the innermost ionized core.

The mid-IR emission in the [S IV] and the broad-band SiC filters from the precessing outflows may have a different origin. To investigate the nature of the emission in these mid-IR filters, we compare in Figure 5.6 spatial profiles along the outflows extracted from the 3.6 cm radio continuum, [S IV], and SiC images. The spatial profile of [S IV] matches that of the 3.6 cm radio continuum; both show a bright emission peak encompassed by two shoulders whose position and relative brightness are very similar. The emission peak corresponds to the core, whereas the shoulders correspond to emission from the collimated outflows. In sharp contrast, the SiC profile shows the bright emission peak from the core, but much fainter emission at the position of the collimated outflows. These results suggest that the extended emission in the [S IV] image indeed originates from [S IV] line emission of the ionized material revealed by the radio continuum emission. The lack of [S IV] line emission in the *ISO* spectrum can be understood as due to the faintness of the collimated outflows in comparison with the emission from the core which is probably the dominant contribution to the *ISO* SWS spectrum.

Meanwhile, the weak extended emission in the collimated outflows registered by the SiC $\lambda11.85\,\mu$m filter may be attributed to dust, thus suggesting that a small amount of dust is present in these structures. This dust component can originate in material from the dust cocoon entrained and carried away by the outflows.

The spatial distribution of the ionized material traced by the optical and near-IR observations is notably distorted by the large extinction towards the central regions of K 3-35. The total extent of the bipolar lobes is only shown in the *HST* images, whereas their outermost, faintest regions are missed by the near-IR images. The J, H, and Brγ images[2] detect emission from the bright spots

---

[2]These images also include the continuum emission from a foreground star southwest of the core of K 3-35.

in the bipolar lobes at the tips of the collimated outflows seen in radio and mid-IR observations. The emission in these broad-band near-IR filters may be attributable to the Paschen and Brackett hydrogen emission lines present in the J and H bands. The faint emission in these filters that envelops the central regions indicates an additional contribution of scattered light.

The spatial coincidence between the point-symmetric knots and the H_2 bright regions is notorious. The origin of the H_2 emission at these positions may be attributed to shocks. Indeed, the spectral properties of these knots strongly suggest that shocks are involved in the emission. In particular, the high [N II]/Hα intensity ratio, the large range of excitation, and the presence of water maser emission in the point-symmetric knots are indicative of shocks (Miranda et al. 2007). These results provide a clear evidence for the existence of neutral material in the point-symmetric knots, as required by the existence of water maser molecules at these positions (see Tafoya et al 2011) Observations of CO and HCO^+ at high angular resolution would be very valuable to test whether these molecules are also associated with the point-symmetric knots and, if so, to study their properties. Moreover, the detection of thermal cold dust toward the core and the collimated outflows of K 3-35 is crucial concerning the existence of water maser molecules. Dust grains absorb most of the UV radiation from the central star, thereby preventing the dissociation of the water molecules. In the case of the core, the radius of the water maser ring ($\simeq 65$ AU; Uscanga et al. 2008) establishes an approximate boundary between the very compact ionized region and the dusty torus, at least along the equatorial plane of K 3-35. Along the perpendicular direction, dust may be swept up and carried outwards by the collimated outflows up to the position of the point-symmetric knots. This would represent another contribution to the neutral material existing in the knots.

The detection of a central dust component veiling the innermost regions of K 3-35 and the distribution of H_2O masers on a small disk reinforce the evidences for the existence of a circumstellar molecular torus in K 3-35. This dust component seems critical to allow the survival of molecules such as H_2O, H_2, or HCO^+, despite the strong UV radiation from the central star. Meanwhile, the H_2O maser emission and the evidence for shocks at the tips of the radio and mid-IR jet-like features strongly support the presence of a fast collimated outflow which interacts with the nebular envelope. The dusty component of the outflows may imply that these, after emanating from the central regions of K 3-35, have entrained material from these inner regions, thus revealing the additional interaction between the fast outflows and the dust cocoon. In these regards, K 3-35 is a notorious case study for models where high-velocity jets and disks are the basic ingredient in the shaping of the most axisymmetric PNe (Morris et al. 1987; Soker et al. 1996; Reyes et. al. 1996; Sahai & Trauger 1998, Soker 2000; Nordhaus & Blackman 2006, Huggings 2007).

5.5. Conclusions

We have presented here new broad- and narrow-band, near- and mid-IR images of the extremely young PN K 3-35. The data have allowed us to make a description of the structures observed at
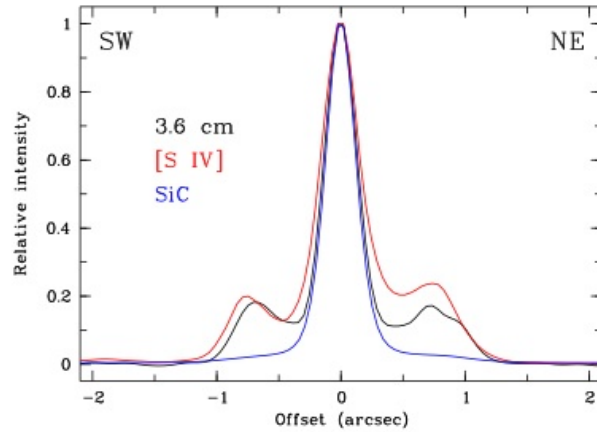
Figure 5.6 Normalized spatial profiles of the emission observed at 3.6 cm radio continuum, [S IV] and SiC filters along PA = 30°.

IR wavelengths and to compare them with the morphology seen at optical and radio continuum wavelengths. These data have been complemented with *ISO* SWS mid-IR spectra to assess the nature of the mid-IR emission.

A faint core is detected in the K_s band, whilst it becomes very bright in the mid-IR. The spectral properties of the core indicate that its mid-IR emission is due to dust.The dust at the core of K 3-35 may shield the water molecules from the ionizing radiation of the central star. Among the three mid-IR images observed in this study, the [S IV] image best shows the bipolar jet previously detected in 3.6 cm radio continuum images. The perfect agreement between the morphology in the [S IV] and 3.6 cm images of this jet implies that the emission from this feature detected in the [S IV] image is mostly contributed by line emission from ionized material. The jet is also detected in the broad-band image at 11.85 μm, but its morphology does not resembles that produced by ionized material, thus suggesting the presence of dust in the bipolar jet, although less abundantly than at the core.

The near-IR broad-band J and H and narrow-band H_2 and Brγ images are very similar to those in the optical, mainly tracing line emission from the point-symmetric knots at the tips of the bipolar jet. Shocks in these knots are the most plausible origin for the H_2 emission. The acquisition of spectral information in the near- and mid-IR to allow us a reliable temperature diagnostic for the dust and the nature of the material in the jet is mandatory in order to draw firm conclusions concerning the origin of the H_2 and mid-IR emissions detected in K 3-35.

Bibliography

Aaquist, O. B., & Kwok, S. 1989. Bipolar radio morphology in the compact nebula K3-35, A&A, 222, 227

Aaquist, O. B., & Kwok, S. 1990. Six centimetre VLA radio survey of compact planetary nebulae, A&A, 84, 229

Aaquist, O. B. 1993, A&A. Detailed radio morphology of the compact nebula K 3-35, 267, 260

Acosta Pulido, J. A., Ballesteros, E., Barreto, M., et al. 2003. First Commissioning of the IR Spectrograph LIRIS, The Newsletter of the Isaac Newton Group of Telescopes, 7, 15

Dayal, A, & Bieging, J. H. 1996. Millimeter-Wave Observations of CO in Planetary Nebulae, ApJ, 472, 703

de Graauw, T. et al. 1996. SWS observations of solid CO_2 in molecular clouds., A&A, 315, L49

Dopita, M. A., & Sutherland, R. S. 2003. Book Review: Astrophysics of the diffuse universe, Springer, 2003, Astrophysics of the diffuse universe, Berlin, New York: Springer, 2003. Astronomy and astrophysics library, ISBN 3540433627

Gómez, Y., Tafoya, D., Anglada, G., et al. 2008. HCO+ emission possibly related with a shielding mechanism that protects water molecules in the young PN K 3-35, IAU Symposium, 251, 173

Gómez, Y., Tafoya, D., Anglada, G., et al. 2009. The Magnetic Field Toward the Young Planetary Nebula K 3-35, ApJ, 695, 930

Huggins, P. J. 2007. Jets and Tori in Proto-Planetary Nebulae, ApJ, 663, 342

Lagage, P. O., Pel, J. W., Authier, M., et al. 2004. Successful Commissioning of VISIR: The Mid-Infrared VLT Instrument, The Messenger, 117, 12

Lucy, L. B. 1974. An iterative technique for the rectification of observed distributions, AJ, 79, 745

Miranda, L. F., Fernández, M., Alcalá, J. M., et al. 2000. High-resolution spectroscopy and broad-band imaging of the young planetary nebula K3-35, MNRAS, 311, 748

Miranda, L. F., Gómez, Y., Anglada, G., & Torrelles, J. M. 2001. Water-maser emission from a planetary nebula with a magnetized torus. Nature, 414, 284

Miranda, L. F., Luridiana, V., Guerrero, M. A., et al. 2007. Morphological and spectroscopic analysis of the planetary nebula K 3-35, Asymmetrical Planetary Nebulae IV, http://www.iac.es/proyect/apn4, article 34

Morris, M. 1987. Mechanisms for mass loss from cool stars, PASP, 99, 1115

Nordhaus, J., & Blackman, E. G. 2006. Low-mass binary-induced outflows from asymptotic giant branch stars, MNRAS, 370, 2004

Reyes-Ruiz, M., & López, J. A. 1999. Accretion Disks in Pre-Planetary Nebulae, ApJ, 524, 952

Richardson, W. H. 1972. Bayesian-Based Iterative Method of Image Restoration, Journal of the Optical Society of America (1917-1983), 62, 55

Rinehart, S. A., Houck, J. R., Smith, J. D., & Wilson, J. C. 2002. Mid-infrared spectroscopy of protoplanetary and planetary nebulae, MNRAS, 336, 66

Sahai, R., & Trauger, J. T. 1998. Multipolar Bubbles and Jets in Low-Excitation Planetary Nebulae: Toward a New Understanding of the Formation and Shaping of Planetary Nebulae, AJ, 116, 1357

Sahai, R., Morris, M. R., & Villar, G. G. 2011. Young Planetary Nebulae: Hubble Space Telescope Imaging and a New Morphological Classification System, AJ, 141, 134

Sloan, G. C., Kraemer, K. E., Price, S. D., & Shipman, R. F. 2003. A Uniform Database of 2.4-45.4 Micron Spectra from the Infrared Space Observatory Short Wavelength Spectrometer, ApJ, 147, 379

Soker, N. 1996. Destruction of Brown Dwarfs and Jet Formation in Planetary Nebulae, ApJ, 468, 774

Soker, N., & Rappaport, S. 2000. The Formation of Very Narrow Waist Bipolar Planetary Nebulae, ApJ, 538, 241

Tafoya, D., Gómez, Y., Anglada, G., et al. 2007. Detection of HCO+ Emission toward the Planetary Nebula K3-35, AJ, 133, 364

Tafoya, D., Imai, H., Gomez, Y., et al. 2011. Measurement of the Distance and Proper Motions of the H2O Masers in the Young Planetary Nebula K 3-35, PASJ, 63, 71

Uscanga, L., Gómez, Y., Raga, A. C., et al. 2008. Kinematics of the H_2O masers at the centre of the planetary nebula K3-35, MNRAS, 390, 1127

6

CRIRES-VLT high-resolution spectro-astrometry in PNe

Among all the morphological varieties displayed by PNe, the most axisymmetric objects represent a challenge for the understanding their formation, since they confront the canonical Generalized Interacting Stellar Wind model (GISW, Balick & Frank 2002). These PNe are believed to be sculpted by fast collimated outflows (jets), whose collimation and launch would be produced by strong magnetic fields (García-Segura et al. 2005) and/or binary systems (Soker 1998). De Marco (2009) proposed the association of disks with the binary evolution through a common-envelope phase. The detection and characterization of those disks ha proven challenging.

This chapter is devoted to the description of the spectroscopic observations and results obtained applying for the first time the high-resolution spectro-astrometry technique to a sample of young PNe and proto-PNe. Section§6.1 is dedicated to the results obtained using CRIRES-VLT commissioning data of a young PN (SwSt 1) and a proto-PN (IRAS 17516-2525). In section §6.2 we present preliminary spectro-astrometric results of the proto-PN AFGL 915.

6.1.   Spectro-astrometry technique applied to CRIRES commissioning data

In this section we explore the capabilities of CRIRES-VLT spectro-astrometry for the detection and analysis of disks and small-scale asymmetrical structures in objects in their transition to PNe. We will describe the CRIRES-VLT observations used in an exploratory program.

6.1.1.   CRIRES-VLT commissioning data

CRIRES-VLT (UT1) commissioning data have been used in the search for small-scale structures hidden in the dusty environments at the core of one proto-PN, IRAS 17516−2525, and one young PN, SwSt 1. CRIRES-VLT operates in the near infrared, from 1 to 5 μm, offering the possibility to

study ionized and molecular material, as well as dust features already present in the mid-IR L-band. CRIRES-VLT can reach a spectral resolution $\sim$100,000 if the 0''.2 slit width is used and the adaptive optic (AO) loop is closed.

The observations were taken with the AO loop closed and the 0''.2 slit, for a PA of the slit of 0°. The exposure time was 120 s and only two nodding positions were used. The data were registered by a 4×1 mosaic of Raytheon 1024×1024 pixel InSb Aladin III detectors with pixel size of 27 μm. The detector readout mode was FowlerNsamp and the observational templates used were Generic offset (in which a larger nodding throw $->25''$ is available, ideal for extended sources) for SwSt 1, and the template commonly used for compact sources using a small nodding throw ($\sim$10'', AutoNodOnSlit) for IRAS 17516−2525. The observations covered the spectral range λ2.115-2.168 μm.

The data were corrected for bad-pixels, flat field, combined to remove the background contamination, and the sky lines were removed using IRAF standard procedures for long-slit spectra. Each combined spectrum was corrected by telluric absorptions using a telluric standard star (HR 7933 for SwSt 1, and HR 5985 for IRAS 17516−2525). The spatial resolution, as determined by the full-width half maximum (FWHM) of the stellar continuum before the spectro-astrometric analysis, was 0''.70 and 0''.66 for the Brγ and [Fe III] lines of SwSt 1, respectively, and 0''.44 for the Brγ line of IRAS 17516−2525. We note that CRIRES-VLT was not optimally focused during this first commissioning run.

Each combined spectrum used for spectro-astrometric analysis was corrected from detector misalignments that might affect the spectro-astrometric (hereafter referred also as SA) signatures obtained, specially at mas scales. This correction was made by fitting the continuum position using a polynomial function (quadratic or cubic). The spectral range around the lines of interest has been fitted with a Gaussian profile using narrow rectangular apertures along the dispersion axis with size 2×60 pixel^2 $\equiv$ 3 km s^{-1}× 5''.16 to derive for each wavelength bin the center of gravity of the flux distribution in the spatial direction. Additional IDL programs were written to perform the spectro-astrometric analysis.

It is important to mention that, even though the observations presented in this section were not specifically tailored to this purpose, they have allowed us to develop the methodology and programing tools to apply the spectro-astrometric technique to search for mas structures in proto-PNe and young PNe.

6.1.2. Spectro-astrometric analysis

IRAS 17516−2525 has been classified as a proto-PN, although, no images revealing its morphology are yet available. The source appears compact in near-IR images (1'' in size, Ramos-Larios et al. 2009; Ramos-Larios et al. 2012), and it is not resolved in the mid-IR imaging catalogue of post-AGB stars presented by Lagadec et al. (2011) despite the nearly-diffracted angular resolution of the images. The spectroscopic study of Sánchez-Contreras et al. (2008) found
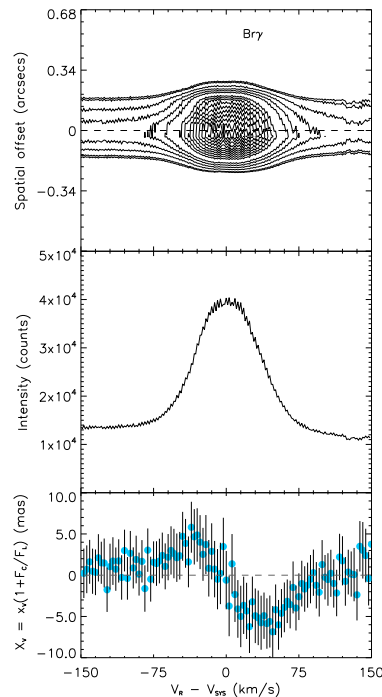
Figure 6.1 Spectrum (*top*), line profile (*middle*), and spectro-astrometric signature (*bottom*) of the Brγ $\lambda 2.160\,\mu$m line of IRAS 17516−2525. The systemic velocity has been assigned to the peak of the line profile. The SA signature shown in the bottom panel can be interpreted as a small-sized Keplerian disk.

a P-Cygni profile in the Hα line, but the Pa lines do not show this profile. We have selected the Br$\gamma\lambda 2.160\,\mu$m line detected in the CRIRES (Figure 6.1) spectrum to carry out the spectro-astrometric analysis. A simple inspection reveals that the line profile appears broad and single peaked. The spectro-astrometric analysis shows a compact antisymmetric position-velocity (PV) pattern extending about $\sim$12 mas in size. This SA signature resembles that observed by Pontoppidan et al. (2008) which is interpreted as a Keplerian velocity field. If this were also the case in IRAS 17516−2525, the disk may show an expansion velocity as high as 40 km s^{-1}. However, an equatorial structure with this characteristics requires an enormous gravitational potential unlikely for the nature of the source studied. The existence of small bipolar lobes rising from the innermost regions of this source is the most suitable interpretation for this SA signature. We reckon that observations at other PAs and a detailed model-fitting are mandatory to corroborate the nature and properties of this structure.

SwSt 1 is a compact hydrogen deficient O-rich PN with a C-rich central star. Spectroscopic studies have found P-Cygni profiles in the C III $\lambda 4650$ Å and C IV $\lambda 5801$ Å lines, but these are not present in the Balmer Hα, Hβ, and Hδ lines (De Marco et al. 2001). The morphology of SwSt 1 is not fully resolved by the pre-COSTAR *HST* WF/PC images presented by De Marco et al. (2001), but they suggest the presence of a compact 2$''$ toroidal structure. In near IR K-band (Likkel et al. 2006) and far-UV (Sterling et al. 2005), it shows high iron abundances and inhomogeneities in the dust-to-gas ratio in different regions of the nebula. These inhomogeneities may be either due to asymmetries in
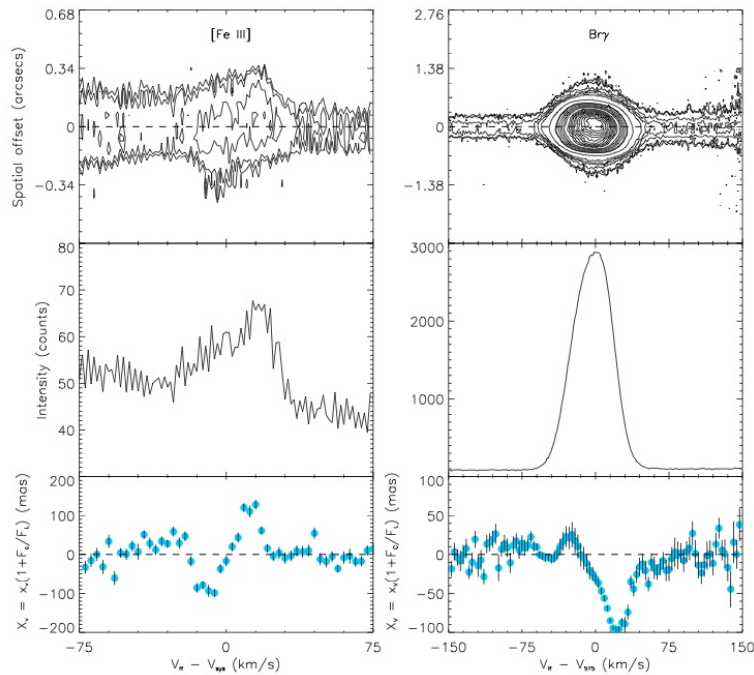
Figure 6.2 Spectrum (*top*), line profile (*middle*), and spectro-astrometric signature (*bottom*) of the [Fe III] $\lambda 2.14$ μm (*left*) and Brγ $\lambda 2.160$ μm (*right*) lines of SwSt 1. The systemic velocity has been assigned to the peak of the single-peaked profile of the Brγ line.

the nebula or small-scale clumping of nebular material (Sterling et al. 2005).

As we can see in Figure 6.2, the PV plot of the two lines studied here ([Fe III] $\lambda 2.145$ μm and Br$\gamma \lambda 2.160$ μm) show a certain degree of asymmetry, particularly the [Fe III] PV plot. After the spectro-astrometric analysis we have found small antisymmetric PV structures ~ 230 mas in size in the [Fe III] line and ~ 130 mas in the Brγ line. Besides the difference in size, there is an obvious difference in the shape of the signature, likely tracing distinct structures according to the material studied. The SA signature of the [Fe III] line is reminiscent of that of a Keplerian disk with an expansion velocity$\simeq 22$ km s^{-1}, as it may be suggested for the Brγ line of IRAS 17516$-$2525. The Brγ signature of SwSt 1 traces smaller features ~ 130 mas in size. This may be a projection effect in the sense that the Brγ structure may be larger if it were a pair of lobes showing a higher expansion velocity, $2 \times V_{\rm exp} \approx 50$ km s^{-1}. These may be interpreted as a pair of bipolar lobes bright in recombined hydrogen with a compact circumstellar disk. Assuming the geometry of the [Fe III] disk and the bipolar lobes orthogonal to this disk, the inclination angle of the disk can not be larger than 60° or the Keplerian velocity would become unreasonably high. This would still allow for the axis of the bipolar lobes to point towards the observer. For SwSt 1 this implies a physical structure of a broad disk and a pair of lobes similar to that reported for the proto-PN CRL 2688 (Sahai et al. 1998) or the young PN Hb 12 (Welch et al. 1999).

These results favour the scenario in which SwSt 1 is asymmetric (Sterling et al. 2005). The presence of [Fe III] (ionization potential of 30.65 eV) line emission in the dense, central regions of Mz 3

(Zhang & Liu 2002) and in NGC 2392 (Zhang et al. 2012) has been attributed to a binary central star in which the hot star accretes and ionizes the wind of its cool companion. The optical spectrum of SwSt 1 also shows [Fe III] and [Fe IV] lines whose ionization, particularly for the highest ion, is difficult to reconcile with the stellar effective temperature of its CS (40,000 K De Marco et al. 2001).

6.1.3.   Commissioning data summary

The spectro-astrometry technique using long-slit high-resolution spectra allows the resolution of small-sized structures in different astronomical objects. Inspired by these results, we have investigated the use of this technique in the search of structures at mas scales at the innermost regions of sources in the transition from the AGB to the PN phase. For this purpose, we have used CRIRES-VLT commissioning data of the proto-PN IRAS 17516−2525 and the young PN SwSt 1 to develop the methodology and the tools to perform the spectro-astrometric analysis to sources in this transition phase.

The preliminary results have been able to detect the presence of small-sized structures ∼130-230 mas in size in the [Fe III] and Brγ near-IR lines of SwSt 1, as well as a small-sized structure ∼12 mas in size in IRAS 17516−2525. These results are suggestive of the presence of small bipolar lobes and equatorial disk in SwSt 1, and a small bipolar lobes rising from the innermost regions of IRAS 17516−2525. Tailored spectro-astrometric observations with its respective calibrations obtained and different PAs, as well as a proper model fitting are mandatory to confirm the presence of these structures.

Remarkably, the spectro-astrometric analysis based on CRIRES-VLT commissioning data has been able to detect structures which are comparable in size to those resolved by MIDI-VLTI for Mz 3 and M 2-9 (∼30 mas, Chesneau et al. 2007; Lykou et al. 2011) reaching a radius of only 6 mas in the case of IRAS 17516-2525, and more compact than those detected in AFGL 915 with radio-interferometric observations at Plateau de Bure (Bujarrabal et al. 2005). Compared to MIDI-VLTI observations, CRIRES-VLT spectro-astrometry is more sensitive, it is not restricted by fixed baselines, and the data interpretation is less model dependent. Therefore, spectro-astrometry offers a very suitable technique for the search of small-sized disks and asymmetries in the short transition to the PN phase.

6.2.   Observations and spectro-astrometric analysis of the axisymmetric proto-PN AFGL 915

Encouraged by the promising results obtained with the CRIRES commissioning data, we have started a program devoted to observe extremely axisymmetric young PNe and proto-PNe in the search of the disks collimating such perplexing morphologies. The observations of the young PN Mz 3 ("The Ant Nebula"), the proto-PN AFGL 915 ("The Red Rectangle"), and the young PN M2-9 ("The Butterfly Nebula") were requested and executed as part of the programs 089.D-0768(A), 090.D-0761(A), and 091.D-0755(A) (P.I.: M.W. Blanco), respectively. Previous studies reporting the

existence of disks were considered as well for the selection of the sample. The spectral lines selected for the spectro-astrometric analysis were selected by the inspection of low-resolution near-IR spectrum, whenever these spectra were available, or according to the chemistry of the sources. We present in the following the preliminary results of the spectro-astrometric analysis of the proto-PN AFGL 915.

The C-O rich proto-PN AFGL 915 is in transition to the PN phase. This source exhibits a distinctive, extended ($\sim 1'$ in size) and axisymmetric X-shaped optical morphology along PA 11°. Its extended emission has a peculiar rectangular appearance due to several lines resembling equally spaced ladder rungs, crossing its symmetry axis, and giving the appearance responsible for the name of "The Red Rectangle" (Figure 6.3, Cohen et al. 1975; Cohen et al. 2004). This reflection nebula is associated with the low-mass post-AGB close binary system HD 44179 with an effective temperature of 7500 K (Waelkens et al. 1996; Men'shchikov et al. 2002).
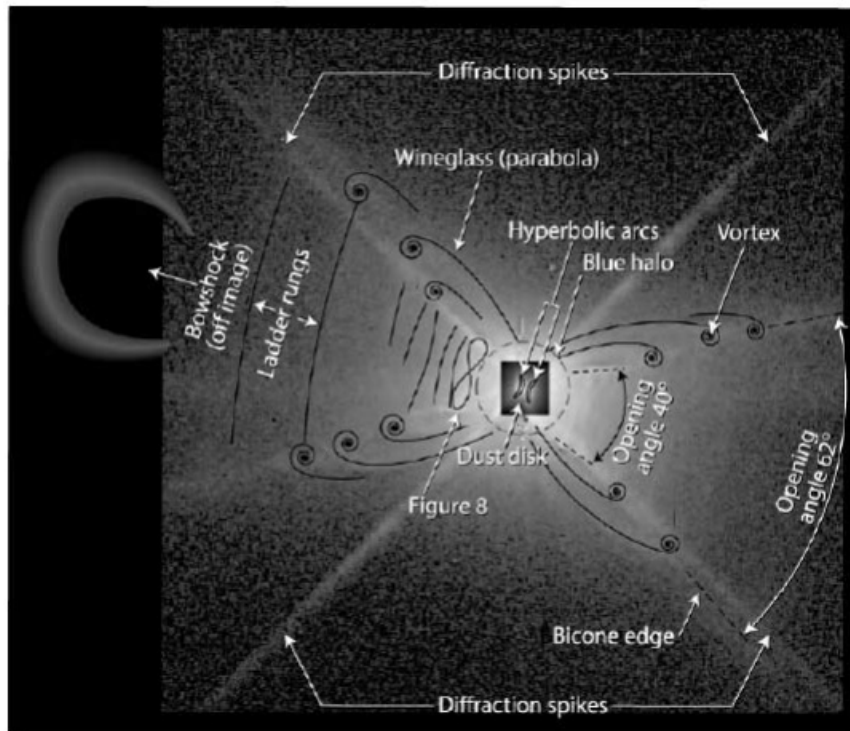

Figure 6.3 *HST* image of AFGL 915 showing all its morphological characteristics. East is up and north to the left (Cohen et al. 2004)

The low-resolution 2.3 to 42.5 μm *ISO* spectrum of AFGL 915 suggests that its core is surrounded by a thick circumbinary and massive disk of crystalline silicates (oxygen-rich dust) viewed nearly edge-on (Waters et al. 1998). The origin of this disk has been attributed either to mass-loss or mass-transfer during a common envelope phase of the progenitor binary system (Waelkens et al. 1996; Men'shchikov et al. 2002). It has been concluded that this dusty disk must be in slow Keplerian rotation ($v =1$ km s^{-1}). The existence of a gravitationally bound long-lived disk in AFGL 915 was firstly proposed by Jura et al. (1995) and barely resolved afterwards by
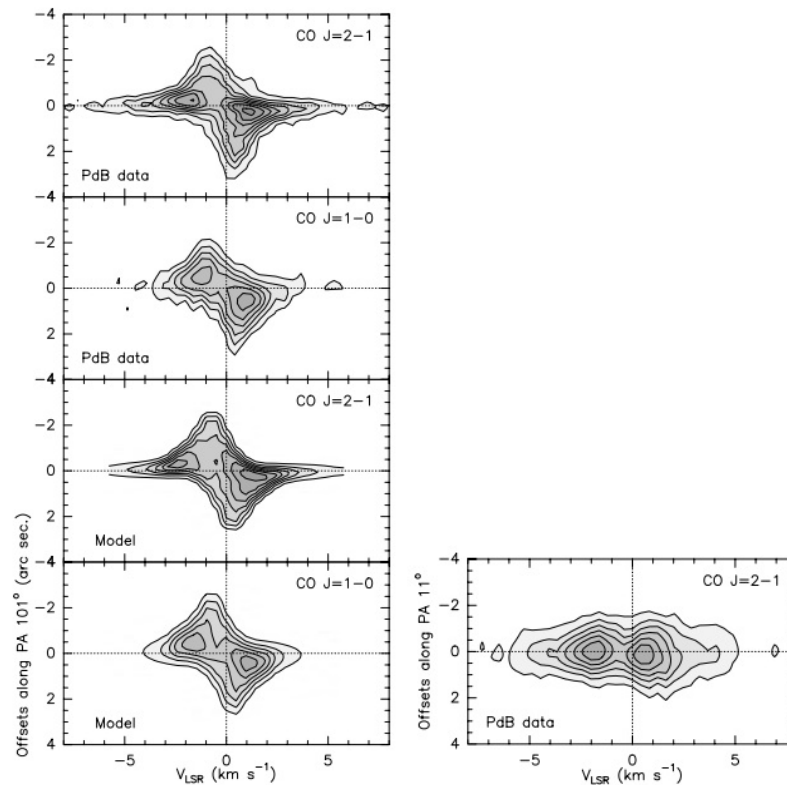
Figure 6.4 (*Left*) Observed and modeled position-velocity diagrams of AFGL 915 along PA 101°. (*Right*) Position-velocity diagram along PA 11°(Bujarrabal et al. 2005)

single-dish CO radio-observations (Bujarrabal et al. 2003). Finally, the existence of a gaseous CO Keplerian disk has been revealed by interferometric radio-observations (PdBI and ALMA, Bujarrabal et al. 2005; Bujarrabal et al. 2013). Interestingly, the high-quality ALMA observations of AFGL 915 additionally revealed the presence of a bipolar component along PA 11° with a moderate velocity of $\lesssim 5$ km s^{-1} and with a tendency to decrease its velocity towards the innermost central regions.

This subsection is structured as follows. First, we will make a brief outline of the properties of the disk previously detected with radio-observations (§6.2.1). The observations and data reduction are described in §6.2.2 and the preliminary results are presented and discussed in §6.2.3.

6.2.1.   Properties of the outermost Keplerian rotating CO disk of AFGL 915

According to the results of the CO J=2-1 and J=1-0 lines (Figure 6.4, Bujarrabal et al. 2005; Bujarrabal et al. 2013), the disk is in stable Keplerian rotation at its innermost regions ($V=\pm 6$ km s^{-1}) and extends up to 1″5 along PA=101°, resulting in a disk with $R_{out}=2.7\times10^{16}$ cm for a distance of 790 pc. They also suggest that the rotation velocity and temperature (30 K< T <400 K) may increase towards the core as the thickness of the disk decreases. Regarding the position-velocity antisymmetric signature characteristic of disks in Keplerian rotation, as confirmed by observations and models of T

Tauri stars, Bujarrabal et al. (2005) reports certain degree of asymmetry between the blue- and the red-shifted velocities, being the blue-shifted velocities smaller (in absolute value) than the red-shifted ones for the two PAs observed (11° and 101°). This effect has been attributed to absorption by the outermost disks parts, and implies the presence of a slow expansion component, whose velocity diminishes from the center to the edge of the CO disk (from 1.6 to 0 $km\,s^{-1}$). All these parameters observed and modelled by Bujarrabal et al. (2005) are representative of the outermost CO rotating disk, not of the innermost disk whose existence has been claimed necessary to describe the shaping of the complex morphology observed in AFGL 915 (Men'shchikov et al. 2002; Cohen et al. 2004). Observations at even more higher spatial resolution are most needed to completely characterize the disk at the core of AFGL 915.

6.2.2. Observations and data reduction
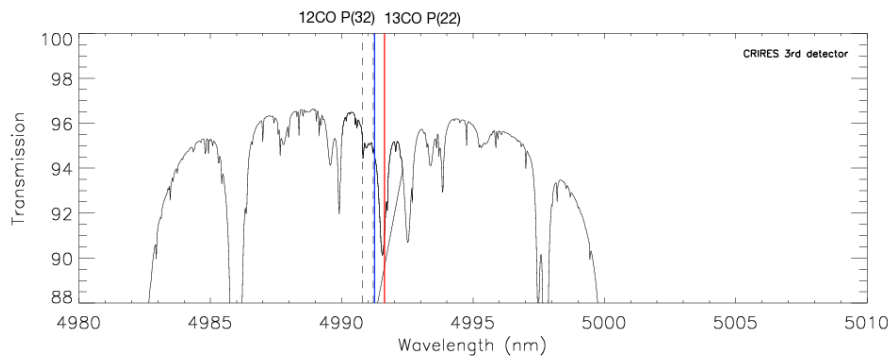
Figure 6.5 Atmospheric transmission spectrum of the full wavelength range covered by the 3rd CRIRES-VLT detector. The vacuum wavelengths of the ^{12}CO and ^{13}CO lines are represented by the dashed line. The wavelengths of these CO lines detected during our observations are in solid lines.
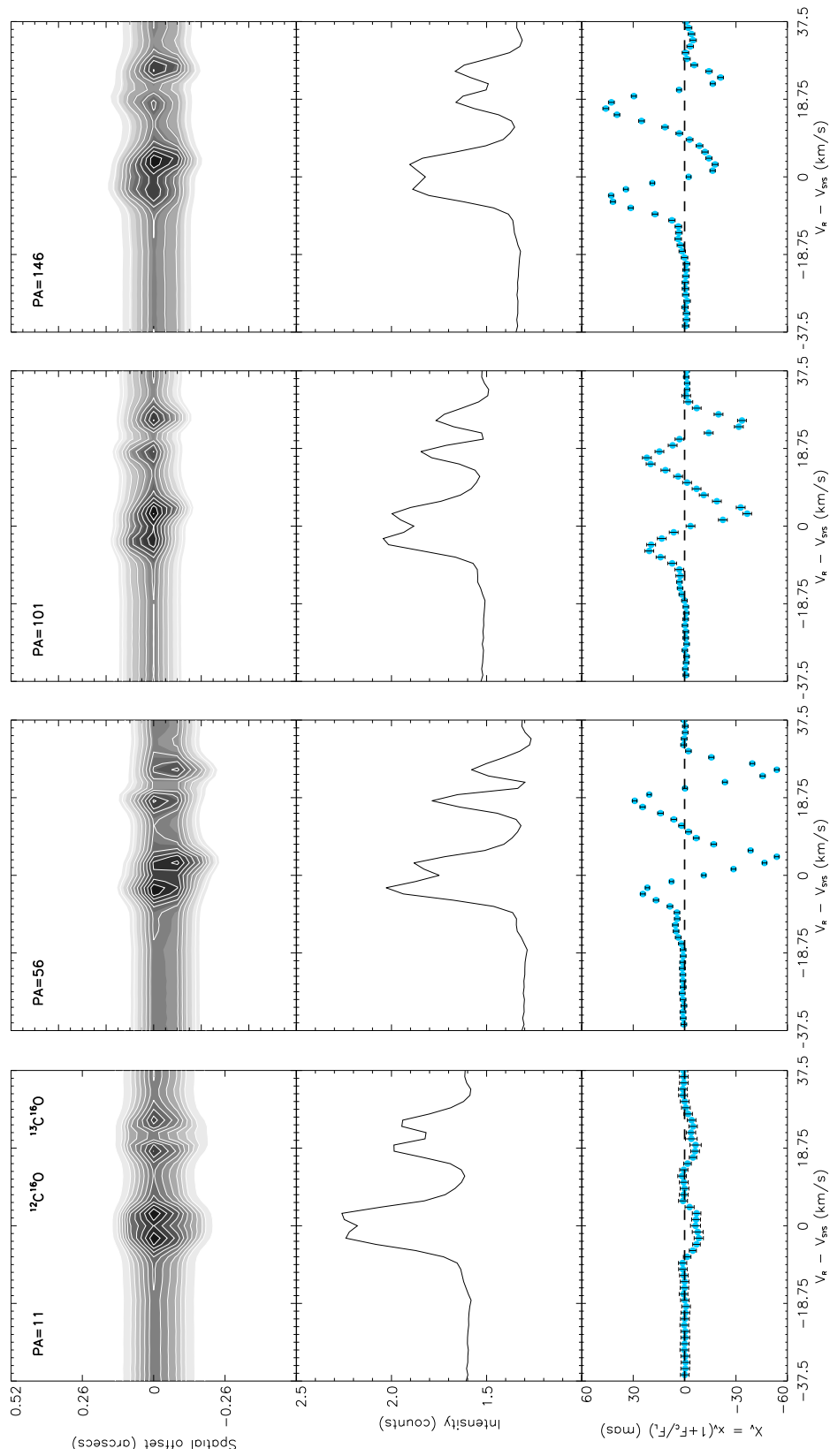
Figure 6.6 Spectro-astrometry of the parallel PAs of AFGL 915. The systemic velocity has been assigned to the minimum shown at the center of the double-peaked CO line profiles.
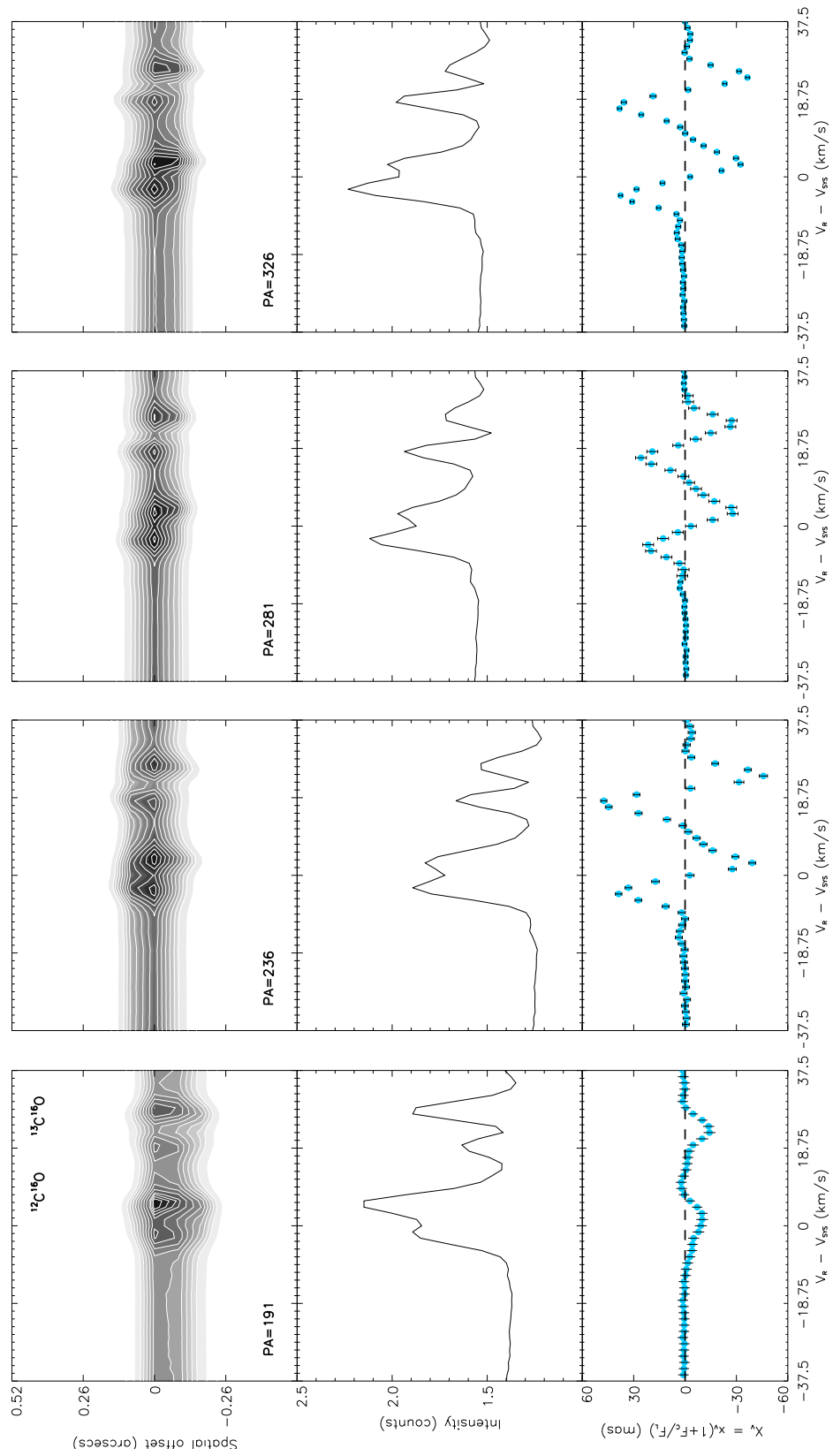
Figure 6.7 Spectro-astrometry of the anti-parallel PAs of AFGL 915. The systemic velocity has been assigned to the minimum shown at the center of the double-peaked CO line profiles.

CRIRES-VLT long-slit high-resolution spectra of the ro-vibrational CO fundamental band ($J = 1 - 0$) at 4.99μm of AFLG 915 have been obtained on December 26, 2012 (Program 090.D-0761(A), P.I. M.W. Blanco). The $0\rlap{.}''2$ slit was used with the AO loop closed. The spectro-astrometry template was used to observe four PAs (11°, 56°, 101°, and 146°) in conjunction with their respective anti-parallel PA (hereafter referred as "aPA"; 191°, 236°, 281°, and 326°) in order to detect possible PSF artifacts. Two nodding positions were obtained for each PA and its aPA with a nodding throw of $20''$ and a jittering of $2''$. The detector read-out mode was FowlerNsamp with a total exposure net time of 600 s for each PA and aPA acquired. Observations of the standard star HR 2502 were executed aiming to perform a telluric correction[1]. The atmospheric transmission for the wavelength range covered by the 3rd CRIRES-VLT detector is shown in the Figure 6.5. This transmission was previously considered, during the preparation of the observations (phase2), to determine the wavelength setting used (grating order 11, reference wavelength 4990.8 nm). Figure 6.5 also allows us to corroborate that the CO fundamental band at 4990.8 nm has not been severely affected by telluric absorption

The data were reduced using Gasgano to correct bad-pixels and flat field, perform the sky subtraction, and combine both A and B nodding positions for all the PAs and aPAs. The sky lines were removed using IRAF by the interpolation of the flux along the spatial direction. No wavelength calibration was performed and the continuum misalignment was corrected by a self-developed IDL program that traces the spectrum and rectifies it along the spatial direction. The spectro-astrometric analysis was performed as described in §2.4.3.

6.2.3.   Preliminarily results: detection of a Keplerian equatorial structure at mas scales

The CRIRES-VLT spectro-astrometric observations have detected the emission of the ^{12}C ^{16}O P(32) J=1-0 fundamental band at 4.9908 μm as well as the emission of the ^{13}C ^{16}O P(22) J=1-0 at 4.9912 μm isotope. We have centered our analysis on the brighter ^{12}C ^{16}O emission line (from now referred as "CO" line). Therefore, all the offsets hereafter mentioned and the further discussion correspond to this CO line. All of the aPAs originally have shown a position-velocity spectrum inverted respect to its respective PA, proving that the signatures hereafter analysed are real. For the analysis, all the aPAs have been inverted along the spatial axis. The extent of the offsets detected with our spectro-astrometric analysis of each pair of PA and its respective aPA will be used to set lower and upper limits for the extents detected in the spectro-astrometric signatures presented in the following. Figures 6.6 and 6.7 show the position-velocity (P-V) diagrams, line profiles, and offsets obtained through the spectro-astrometric analysis for all the PAs and aPAs of AFGL 915, respectively.

---

[1]The observations of the standard star carried out during this observing program were not used to perform telluric correction, since this spectrum lacked the required signal to be used to correct the science spectrum. The telluric correction is not mandatory in the spectro-astrometric analysis as performed by Pontoppidan et al. (2008, 2011), however, preventing telluric absorption is important and can be performed also by observations of the same PA and aPA, with the same instrumental setup, and executed in different dates (see Pontoppidan et al. (2008)).

Position-velocity diagrams. The P-V diagram of each PA and its respective aPA (first row) without SA analysis has resolved two spectral components for the CO line, with a total extent of $\sim0.\!\!''3$ for all the PAs. An antisymmetric P-V[2] field is shown for all the PAs, except for the PA 11° and its respective aPA at 191°. All the antisymmetric P-V reveal asymmetries in the blue-shifted velocities, being less extended than the red-shifted velocities.

Line profiles. The line profiles (second row) reveal a double-peaked profile. The intensity among all the PAs and aPAs has no strong variations but present asymmetries in some of them. The blue-shifted peak of the aPAs 191°is less intense than the red peak. Whereas for PA 56°, PA 101° and the rest of aPAs the blue-shifted peak is more intense. As for the double-peaked line profiles of PA 11°and 146°, the line profiles are fairly symmetric.

Spectro-astrometric signatures. The spectro-astrometric results are in the third row of the Figures 6.6 and 6.7. We note the increase and variation of the spatial extent of the SA signature as long as we move from 11° to 146° (from $\lesssim$10 mas up to $\gtrsim$50 mas). An antisymmetric P-V signature is observed more in detail in all the PAs, except from PA 11° and aPA 191°, with blue- and red-shifted velocities shifted to negative spatial values with regard to the stellar continuum. The asymmetries between the blue- and the red-shifted velocities are more notorious after the SA analysis. The maximum offset extent is detected at PA 56°(60 mas) in the red-shifted velocity. Meanwhile, for its respective aPA (236°) the spatial extent reaches 40 mas. Contrary to the PA 56°, this signature is the most symmetric detected. Remarkably, PA 146° also presents a large extent up to $\sim$40 mas, however, like the 56° and 236° PAs, there is a discrepancy between the symmetry of both signatures detected, being the aPA 326° signature considerably more symmetric than the 146° signature.

Geometry of the spectro-astrometric signatures. The inspection of the line profiles and their corresponding SA signatures indicates that they resemble Keplerian sources, since they display double-peaked line profiles in conjunction with an antisymmetric P-V at all PAs, two widely accepted characteristics of this kind of sources. The radial velocity of this structure is $\sim$5 $\mathrm{km\,s^{-1}}$. These antisymmetric P-V are consistent with those previously found using PdBI interferometric CO data (Bujarrabal et al. 2005), providing further support to the existence of a Keplerian rotating disk. Our preliminary analysis may be representative of the innermost CO disk.

Bujarrabal et al. (2005) has suggested the existence of temperature and velocity gradients along the CO Keplerian disk. Both the temperature and velocity are supposed to be higher towards the innermost regions. Our measurements report a velocity consistent with the rotation velocity previously reported. The excitation temperature of the ^{12}CO line at 4.99 μm is of $300-400$ K (Waters et al. 1998), in concordance with the calculations of Bujarrabal et al. (2005), who predicted gas temperatures of 400 K towards the innermost disk.

---

[2]Antisymmetric P-V field refers to the typical spectral signature of a disk in Keplerian rotation, named in this manner because either the blue-shifted and the red-shifted velocities are symmetric, but inverted one with respect to the other (see Weintraub et al. 1989).
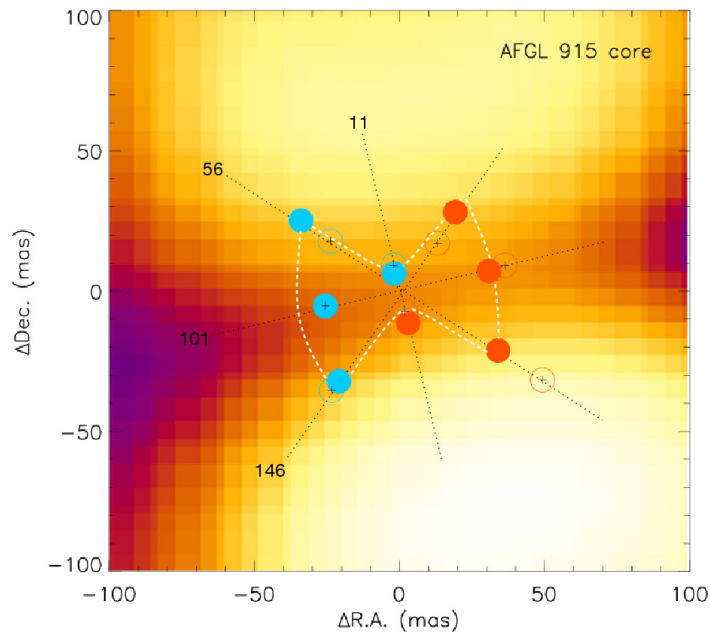
Figure 6.8 Sketch of the innermost thick torus-like structure traced by the spatial offsets measured in the spectro-astrometric analysis for the PAs (circles with a "+" in their center) and aPAs (filled circles). Blue and red colors represent the blue- and red- shifted velocities. The offsets are overimposed in an H-band image of AFGL 915 adapted from Men'shchikov et al. (1998).

We have investigated the orientation and the geometry of the CO gaseous Keplerian-like disk structure detected in our SA analysis of AFGL 915 (Figure 6.8). The geometry of this innermost disk, revealed by the Figure 6.8, might be interpreted as a tilted and thick torus-like innermost structure with a total extent in the range of ∼80 mas and 100 mas. The waist along 101° can be interpreted as a projection affect on this torus: along the edges, the line of sight goes across a thick column of material, whereas across the center the light path is smaller. Considering the differences in the extents of the SA signatures, the radius of this equatorial structure ranges between 40 and 50 mas. The NE regions of the disk is moving towards the observer with velocities ∼5 km s^{-1}, whereas the SW regions recedes from us. Our results reveal a remarkable thick geometry and the size of this thick torus-like structure are in good agreement with the one theoretically predicted at the innermost regions of AFGL 915 by Men'shchikov et al. (2002) (Figure 6.9). Nevertheless, this model is based in dust continuum radiative transfer and it is not demonstrated that dust and CO are coupled.

As modeled by Men'shchikov et al. (2002), the equatorial thick-disk resembles a torus. However, this model implies a massive, self-gravitating and slowly evolving thick torus, contrary to the flat disk geometry generally used to explain the shaping of an axisymmetric PN. Furthermore, the radiative transfer modeling of the molecular gas in the innermost disk of AFGL 915 (Bujarrabal & Alcolea 2013) is reminiscent of the geometry predicted by Men'shchikov et al. (2002) (Figure 6.9).

Assuming a distance of 719 pc, the results of the studies of Bujarrabal & Alcolea (2013) and Men'shchikov et al. (2002) have concluded that this equatorial structure in AFGL 915 has the following properties (Figure 6.9):

- High density at the innermost regions of the torus that drops by 5 orders of magnitude at 100 AU (150 mas). Beyond this point, in the outermost regions of the disk, the density profile becomes flatter.

- The velocity field is Keplerian in the innermost regions of the disk, at a radius $\lesssim$560 AU ($<8.4\times10^{15}$ cm).

- The temperature of the dust grains is $T_d \sim$1000 K. As for the gaseous component, the temperature may be >200 K.

- As for the thickness (height) of the torus, Bujarrabal et al. (2013) reports a value of $\sim$430 AU (6.5×10^{15} cm), whereas Men'shchikov et al. (2002) predict a thickness of $\sim$130 mas (85 AU).

From our SA preliminary analysis, we infer that the CO thick torus-like found has an outer radius $r_{out} \approx$35 AU ($\sim5.3\times10^{14}$ cm, 50 mas) and a thickness $\sim$43 AU ($\sim6.4\times10^{14}$ cm, 60 mas). Apparently our SA measurements are mapping inner regions of the disk investigated by Bujarrabal et al. (2013) and Men'shchikov et al. (2002). This is in agreement with the prediction of a temperature gradient in the disk, as the CO lines observed in this study are more sensitive to the hotest regions.

According to Men'shchikov et al. (2002) the disk has been launched by the close binary system and the cavities have been produced by a fast bipolar flow that has carved in the AGB envelope the fascinating morphology of AFGL 915. Regarding to its progenitor binary system, it is composed by a white dwarf and an AGB primary companion of M$_*$=0.57 $M_\odot$, L_*=6$\times10^3$ in which unstable mass-loss gives rise to a common envelope phase.

The existence of disks as shaping agent of axisymmetric PNe are necessary, but whether they are in expansion or rotating, or which are their components, are under debate. Since the first clear evidence of a Keplerian disk around a proto-PN (Bujarrabal et al. 2003; Bujarrabal et al. 2005), the search of this type of disks has increased. De Ruyter et al. (2006) has found strong evidences of Keplerian rotating passive disks in a sample of 51 post-AGB stars whose SEDs present strong IR excess. Meanwhile, Bujarrabal et al. (2013) has presented a sample of post-AGB stars, in which strong evidences of rotating disks has been found. These studies have a common ingredient: a close binary system as progenitor of these sources, which is a plausible scenario to achieve the required angular momentum to collimate and thus to shape axisymmetric PNe (Huarte-Espinosa et al. 2013; Tocknell et al. 2013). In the De Ruyter et al. (2006) study, the results found are likely Keplerian passive disks, while Bujarrabal et al. (2013) suggests the presence of reaccretion to setup these Keplerian disks of the post-AGB sources investigated.
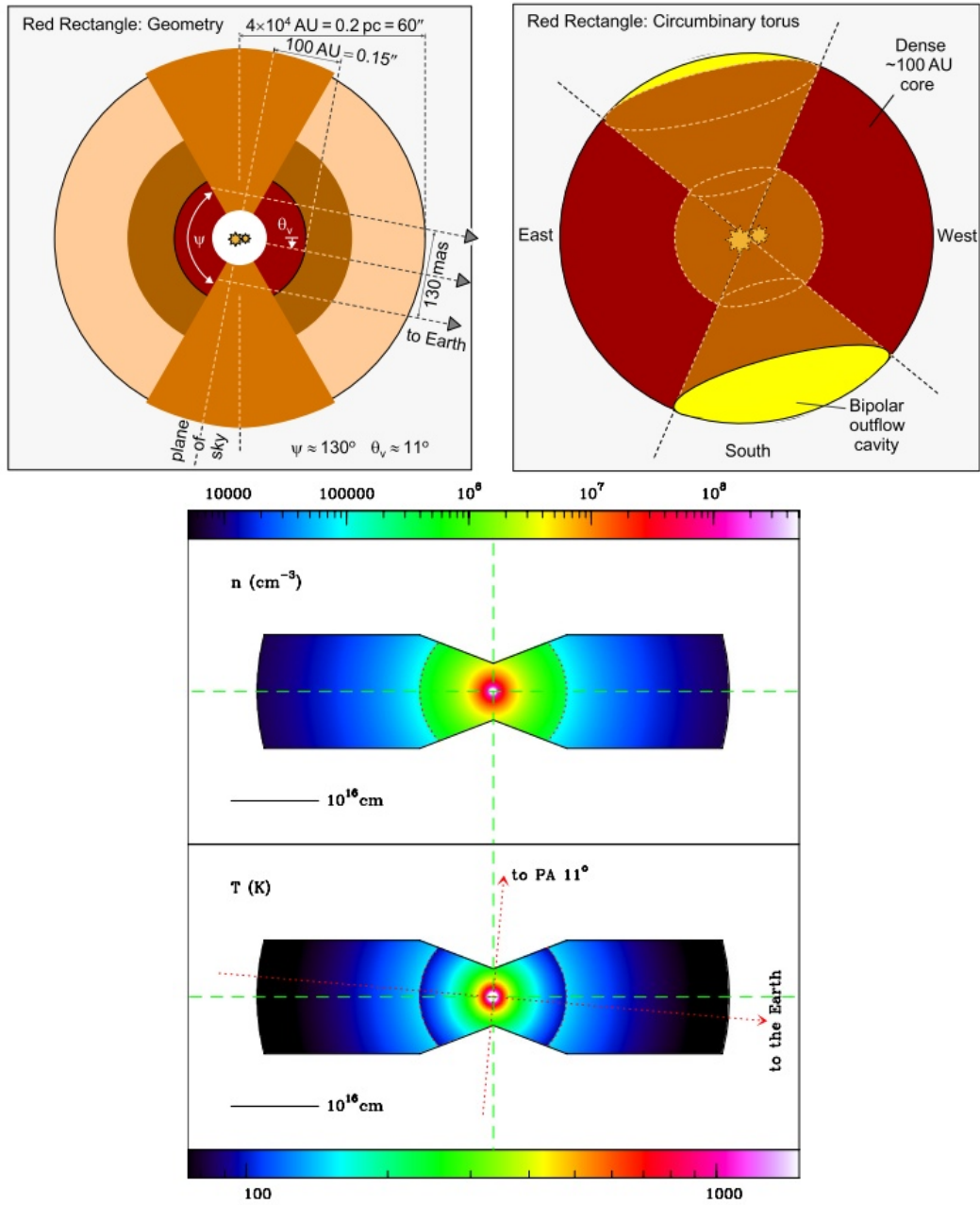
Figure 6.9 (*Upper*) The innermost small-sized torus theoretically predicted by Men'shchikov et al. (2002). (*Bottom*) Modeling of the density and temperature distribution of the molecular gas in the CO disk of AFGL 915 (Bujarrabal & Alcolea 2013).

The preliminary SA analysis presented in this thesis likely provides the first observational evidence of an innermost gaseous thick torus able to collimate a bipolar PN. According to Men'shchikov et al. (2002), this disk is slowly accreting material. Assembling the theoretical models with the observational evidences collected over the last years for AFGL 915, a fascinating bipolar proto-PNe is being sculpted by the interaction of two close binaries experiencing a common envelope phase (Waelkens et al. 1996; Men'shchikov et al. 2002). This scenario favours the formation of a compact innermost and dense torus composed by dust and gas, in Keplerian rotation, and undergoing slow accretion. Furthermore, this scenario is in agreement with the models which claim the common envelope phase as one of the possibilities to launch a disk and high velocity jets (Mastrodemos & Morris 1999; De Marco 2009), giving rise to an axisymmetric PN.

6.2.4. Summary of the spectro-astrometric analysis of AFGL 915

The shaping agent of AFGL 915 has at least three equatorial components along PA 101°: an outermost massive disk of crystalline silicates in slow Keplerian rotation as was revealed by the *ISO* spectrum; an inner expanding and rotating gaseous CO Keplerian disk with a trend to increase its velocity and temperature towards the innermost regions, as the thickness decreases; and an innermost dusty and massive torus which likely has a gaseous CO component also in form of thick torus in slow Keplerian rotation. The geometry of the preliminary spectro-astrometric results is in concordance with previous radiative transfer models of the innermost thick disk at the center of this proto-PN.

Our spectro-astrometric observations reveals in the case of AFGL 915 that circumstellar disks around AGB stars are large structures that extend from an inner radius of 5.3×10^{14} cm (~ 35 AU) up to 2.7×10^{16} cm (~ 1800 AU).

The presence of these components (a binary system and an accreting disk) represents a plausible scenario to form a bipolar PN. Our preliminary spectro-astrometric analysis, in conjunction with the radiative transfer modeling and the CO radio observations performed in other studies may complete the scenario of an equatorial thick disk, composed by dust and gas, in Keplerian rotation and, likely, accreting material in a self-gravitating massive innermost toroidal component.

Finally, we have proven the feasibility of the use of CRIRES-VLT high-resolution spectra using observations devoted solely to perform a spectro-astrometric analysis in the search of disks at the innermost regions of PNe. A full implementation of this technique in this field will require a proper model fitting to the results obtained by means of spectro-astrometry.

Bibliography

Bailey, J. 1998. Detection of pre-main-sequence binaries using spectro-astrometry, MNRAS, 301, 161

Balick, B., & Frank, A. 2002. Shapes and Shaping of Planetary Nebulae, A&AR, 40, 439

Bujarrabal, V., Neri, R., Alcolea, J., & Kahane, C. 2003. Detection of an orbiting gas disk in the Red Rectangle, A&A, 409, 573

Bujarrabal, V., Castro-Carrizo, A., Alcolea, J., & Neri, R. 2005. The orbiting gas disk in the Red Rectangle, 441, 1031

Bujarrabal, V., Alcolea, J., Van Winckel, H., Santander-Garcia, M., & Castro-Carrizo, A. 2013, Extended rotating disks around post-AGB stars, arXiv:1307.1975

Bujarrabal, V., & Alcolea, J. 2013, A&A. Warm gas in the rotating disk of the Red Rectangle: accurate models of molecular line emission, 552, A116

Chesneau, O., Lykou, F., Balick, B., et al. 2007. A silicate disk in the heart of the Ant, 473, L29

Coffey, D., Bacciotti, F., Podio, L., & Nisini, B. 2010. Hydrogen Permitted Lines in the First Near-IR Spectra of Th 28 Microjet: Accretion or Ejection Tracers?, ApJ, 719, 505

Cohen, M., Anderson, C. M., Cowley, A., et al. 1975. The peculiar object HD 44179 "The red rectangle", ApJ, 196, 179

Cohen, M., Van Winckel, H., Bond, H. E., & Gull, T. R. 2004. Hubble Space Telescope Imaging of HD 44179, The Red Rectangle, AJ, 127, 2362

De Marco, O., Crowther, P. A., Barlow, M. J., Clayton, G. C., & de Koter, A. 2001. SwSt 1: an O-rich planetary nebula around a C-rich central star, MNRAS, 328, 527

De Marco, O. 2009. The Origin and Shaping of Planetary Nebulae: Putting the Binary Hypothesis to the Test, PASP, 121, 316

de Ruyter, S., van Winckel, H., Maas, T., et al. 2006. Keplerian discs around post-AGB stars: a common phenomenon?, A&A, 448, 641

García-Segura, G., López, J. A., & Franco, J. 2005. Magnetically Driven Winds from Post-Asymptotic Giant Branch Stars: Solutions for High-Speed Winds and Extreme Collimation, ApJ, 618, 919

Huarte-Espinosa, M., Carroll-Nellenback, J., Nordhaus, J., Frank, A., & Blackman, E. G. 2013. The formation and evolution of wind-capture discs in binary systems, MNRAS, 433, 295

Jura, M., Balm, S. P., & Kahane, C. 1995. A Long-lived Disk around the Red Rectangle?, ApJ, 453, 721

Lagadec, E., Verhoelst, T., Mékarnia, D., et al. 2011. A mid-infrared imaging catalogue of post-asymptotic giant branch stars, MNRAS, 417, 32

Likkel, L., Dinerstein, H. L., Lester, D. F., Kindt, A., & Bartig, K. 2006. A Spectrophotometric Survey of K-Band Emission Lines in Planetary Nebulae, AJ, 131, 1515

Lykou, F., Chesneau, O., Zijlstra, A. A., et al. 2011. A disc inside the bipolar planetary nebula M2-9, A&A, 527, A105

Mastrodemos, N., & Morris, M. 1999. Bipolar Pre-Planetary Nebulae: Hydrodynamics of Dusty Winds in Binary Systems. II. Morphology of the Circumstellar Envelopes, ApJ, 523, 357

Miranda, L. F., Fernández, M., Alcalá, J. M., et al. 2000. High-resolution spectroscopy and broad-band imaging of the young planetary nebula K3-35, MNRAS, 311, 748

Miranda, L. F., Gómez, Y., Anglada, G., & Torrelles, J. M. 2001. Water-maser emission from a planetary nebula with a magnetized torus, Nature, 414, 284

Men'shchikov, A. B., Balega, Y. Y., Osterbart, R., & Weigelt, G. 1998. High-resolution bispectrum speckle interferometry and two-dimensional radiative transfer modeling of the Red Rectangle, New Astronomy, 3, 601

Men'shchikov, A. B., Schertl, D., Tuthill, P. G., Weigelt, G., & Yungelson, L. R. 2002. Properties of the close binary and circumbinary torus of the Red Rectangle, A&A, 393, 867

Pontoppidan, K. M., Blake, G. A., van Dishoeck, E. F., et al. 2008. Spectroastrometric Imaging of Molecular Gas within Protoplanetary Disk Gaps, ApJ, 684, 1323

Pontoppidan, K. M., Blake, G. A., & Smette, A. 2011. The Structure and Dynamics of Molecular Gas in Planet-forming Zones: A CRIRES Spectro-astrometric Survey, ApJ, 733, 84

Ramos-Larios, G., Guerrero, M. A., Suárez, O., Miranda, L. F., & Gómez, J. F. 2009. Searching for heavily obscured post-AGB stars and planetary nebulae. I. IRAS candidates with 2MASS PSC counterparts, A&A, 501, 1207

Ramos-Larios, G., Guerrero, M. A., Suárez, O., Miranda, L. F., & Gómez, J. F. 2012. Searching for heavily obscured post-AGB stars and planetary nebulae. II. Near-IR observations of IRAS sources, A&A, 545, A20

Sahai, R., Hines, D. C., Kastner, J. H., et al. 1998. The Structure of the Prototype Bipolar Protoplanetary Nebula CRL 2688 (Egg Nebula): Broadband, Polarimetric, and H 2 Line Imaging with NICMOS on the Hubble Space Telescope, ApJL, 492, L163

Sahai, R., & Trauger, J. T. 1998. Multipolar Bubbles and Jets in Low-Excitation Planetary Nebulae: Toward a New Understanding of the Formation and Shaping of Planetary Nebulae, AJ, 116, 1357

Sahai, R., Morris, M., Sánchez Contreras, C., & Claussen, M. 2007. Preplanetary Nebulae: A Hubble Space Telescope Imaging Survey and a New Morphological Classification System, AJ, 134, 2200

Sánchez Contreras, C., Sahai, R., Gil de Paz, A., & Goodrich, R. 2008. Echelle Long-Slit Optical Spectroscopy of Evolved Stars, ApJS, 179, 166

Soker, N. 1998. Magnetic field, dust and axisymmetrical mass loss on the asymptotic giant branch, MNRAS, 299, 1242

Sterling, N. C., Dinerstein, H. L., Bowers, C. W., & Redfield, S. 2005. The FUSE Spectrum of the Planetary Nebula SwSt 1: Evidence for Inhomogeneities in the Gas and Dust, ApJ, 625, 368

Suárez, O., Gómez, J. F., Miranda, L. F., et al. 2009. Water maser detections in southern candidate post-AGB stars and planetary nebulae, A&A, 505, 217

Suárez, O., Lagadec, E., Bendjoya, P., et al. 2011. Water fountains and H_2O-PNe as seen by VISIR/VLT, Asymmetric Planetary Nebulae 5 Conference, 7P

Takami, M., Bailey, J., Gledhill, T. M., Chrysostomou, A., & Hough, J. H. 2001. Circumstellar structure of RU Lupi down to au scales, MNRAS, 323, 177

Tocknell, J., De Marco, O., & Wardle, M. 2013. Constraints on Common Envelope Magnetic Fields from Observations of Jets in Planetary Nebulae, arXiv:1308.5027

Uscanga, L., Gómez, Y., Raga, A. C., et al. 2008. Kinematics of the H_2O masers at the centre of the planetary nebula K3-35, MNRAS, 390, 1127

Verhoelst, T., Waters, L. B. F. M., Verhoeff, A., et al. 2009. A dam around the Water Fountain Nebula?. The dust shell of IRAS16342-3814 spatially resolved with VISIR/VLT, A&A, 503, 837

Waelkens, C., Van Winckel, H., Waters, L. B. F. M., & Bakker, E. J. 1996. Variability and nature of the binary in the Red Rectangle nebula, A&A, 314, L17

Waters, L. B. F. M., Cami, J., de Jong, T., et al. 1998. An oxygen-rich dust disk surrounding an evolved star in the Red Rectangle, Nature, 391, 868

Whelan, E. T., Ray, T. P., Bacciotti, F., et al. 2005. A resolved outflow of matter from a brown dwarf, Nature, 435, 652

Whelan, E., & Garcia, P. 2008. Spectro-astrometry: The Method, its Limitations, and Applications, Jets from Young Stars II, 742, 123

Welch, C. A., Frank, A., Pipher, J. L., Forrest, W. J., & Woodward, C. E. 1999. [Fe II] Bubbles in the Young Planetary Nebula Hubble 12, ApJL, 522, L69

Weintraub, D. A., Zuckerman, B., & Masson, C. R. 1989. Measurements of Keplerian rotation of the gas in the circumbinary disk around T Tauri, ApJ, 344, 915

Zhang, Y., & Liu, X.-W. 2002. A spectroscopic study of the bipolar planetary nebula Mz 3, MNRAS, 337, 499

Zhang, Y., Fang, X., Chau, W., et al. 2012. [Fe iii] lines in the planetary nebula NGC 2392, ApJ, 754, 28

7

Conclusions and future work

The subject of this thesis has been to perform an observational study of the complex and not yet well understood shaping process of asymmetric PNe, beautiful remnants of low- and intermediate-mass stars. Although the envelopes of the AGB progenitor stars are spherical, nearly 80 % of the PNe are asymmetric. Since the youngest PNe and those sources in transition to this phase are quite compact and often embedded in dusty environments, the observation of these sources is challenging and the use of high-resolution techniques at wavelength ranges able to peer through thick dust envelopes is crucial.

In this regard, we have used CRIRES-VLT and VISIR-VLT, two VLT instruments operating in the near- and mid-IR, taking advantage of their quality and high-resolution data. Strong IR emitters in transition to the PN phase (post-AGB sources and proto-PNe), as well as young PNe have conformed the samples used in the three different observational studies presented in this thesis. These studies have disclosed morphological and physical characteristics and have provided important complementary results to these evolutionary phases. The morphological and physical characteristics of heavily obscured post-AGB sources have been studied. We have also linked the morphological characteristics between different spectral ranges, from the optical to radio wavelengths, in the young water maser emitter PN K 3-35. Finally, we have implemented for the first time the high-resolution spectro-astrometry technique in the study of compact structures at the innermost regions of proto-PNe and PNe. We summarize these results in the following paragraphs.

High-resolution imaging

Since the onset of asymmetries in PNe takes place at some point between the late AGB and the post-AGB phases, we have performed high-resolution VISIR-VLT observations of a sample of four heavily obscured post-AGB stars and PN candidates. Three sources in our sample (IRAS 15534−5422, IRAS 17009−4154, and IRAS 18454+0001) can be classified as young PNe, whereas only a preliminary classification as a post-AGB source is possible for IRAS 18229−1127. The high-angular resolution mid-IR images in the N-band PAH1 ($\lambda 8.54 \mu$m), SiC ($\lambda 11.85 \mu$m), and [Ne II] ($\lambda 12.82 \mu$m) filters as

well as Q1 ($\lambda17.65\mu$m) have enabled us to investigate the characteristics of the extended emission of the sources in our sample. Deconvolution techniques have been used to improve the images resolution. Two different algorithms have been used to deconvolve the images, Richardson-Lucy and maximum likelihood, and we have selected the best images to enhance the morphologies resolved by VISIR-VLT.

These images were used to investigate the spatial variations of the physical conditions of the sample taking advantage of the high-spatial resolution achieved by VISIR-VLT. We have built temperature (color) and optical depth maps using the N-band and the Q1 images of the sources. These temperature and optical depth maps, in conjunction with the images, provide evidence of asymmetry in the three sources classified as young PNe. IRAS 15534−5422 resembles a bipolar PN with a prominent equatorial dusty ring. IRAS 17009−4154 is likely elliptical or slightly bipolar, and also presents evidence of a warmer toroidal inner structure. As for the compact young PN IRAS 18454−0001, our high-angular resolution study has revealed an inner dusty torus surrounded by an ionized spherical shell, as well as hotter ionized regions perpendicular to the torus. The post-AGB candidate IRAS 18229−1127 has a detached rhomboidal-like envelope; the presence of a detached envelope is in concordance with an object in an early post-AGB phase. The use of temperature and optical depth maps has demonstrated its utility in this study, revealing morphological components and the spatial distribution of their physical conditions. In comparison to previous works that have built this type of maps, the use of the mid-IR high-resolution data provided by VISIR-VLT has been crucial to disclose structures in detail of the previously unresolved sample.

Our imaging study has confirmed that asymmetry is present in heavily obscured post-AGB stars and young PNe but, unlike previous studies focused on these evolutionary phases, no extreme axisymmetric morphologies are found. These previous studies may be biased towards the brightest mid-IR and optical sources, missing critical early phases of the post-AGB evolution of the most massive progenitors. Although based on a small sample, our study may be disclosing important clues to the onset of asymmetry in massive progenitors of PNe. Further studies of the most obscured post-AGB sources must be pursued in the future.

On the other hand, multiwavelength studies of PNe have shown to be important since the morphological characteristics of PNe may present dramatic changes from a given spectral range to another one. This is the case of the extremely young PN K 3-35, a water maser emitter object, whose optical and radio-continuum morphologies have revealed substantial differences. In contrast with the optical features of K 3-35, bright bipolar lobes and a dark equatorial lane, the radio-continuum morphology reveals a bright core and the precessing jets responsible of its point-symmetric morphology.

We have acquired broad- and narrow-band NICS and TNG near-IR images, as well as VISIR-VLT N-band mid-IR images of this PN to investigate its morphology at these wavelengths. We have used these data to describe the structural components of K 3-35 in the near-IR K-band and in the mid-IR N-band and a comparison with the optical and radio-continuum morphologies has been made. The SWS *ISO* spectrum of K 3-35 has also been used to investigate the nature of its mid-IR emission.

The VISIR-VLT images were deconvolved using the Richardson-Lucy algorithm to enhance the details of the mid-IR morphology. We have found a close correspondence among the near-IR broad- and narrow-band images with the optical appearance of this source, tracing the bright tips of the precessing jet and the point symmetric knots. Remarkably, faint emission at the core is detected in the K_s band. The mid-IR images are dominated by a very bright core. The spectral properties of this core indicate that its mid-IR emission is produced by warm dust. Emission of the precessing jet is detected in the broad-band SiC filter and this emission becomes more prominent in the [S IV] image. We report H_2 emission spatially coincident with the tips of the precessing jet. The molecules, such H_2 and the water maser innermost ring previously detected, must be shielded by the dust. Considering that the PN phase in which the strong UV radiation has started in K 3-35, we suggest the presence of a dusty cocoon enclosing the ionized material in the core of this source.

The [S IV] image has revealed a perfect match with the radio-continuum morphology, implying that this morphological component of K 3-35 in the mid-IR is mostly contributed by ionized gas. The jet has been faintly traced by the broad SiC filter, although does not resemble the morphology traced by ionized gas, suggesting an additional dust contribution in the jet, considerably less abundant than at the core. This high-velocity jet must swept the dust from the core, giving rise to the faint contribution of dust detected by the VISIR-VLT images. The presence of H_2 emission in the knots of K 3-35 may be shock excited. However, spectral information in the near- and mid-IR is mandatory to verify the nature of the H_2 emission as well as the mid-IR emission of the jet observed in K 3-35.

High resolution spectro-astrometry

Spectral and interferometric observations yield the high-resolution necessary to study the shaping mechanism of PNe. Long-baseline interferometric studies in radio and in the IR have revealed valuable information to further understand and to parametrize disks at the innermost regions of axisymmetric PNe. The mid-IR has the major contribution of thermal emission from C- and O-rich dust, as well as warm atomic and molecular gas. It has been proven that this gaseous and dust emission perform an important role in the sculpting process of the most extreme axisymmetric PNe. For these reasons, we have applied for the first time the high-resolution spectro-astrometry technique to the search of disks and compact structures at the innermost regions of PNe. This technique has proven to be able to resolve protoplanetary disks at mas scales in the near-IR. We have chosen CRIRES-VLT, whose spectral coverage ranges from 1 to 5 μm, represents a prolific spectral range in which atomic and molecular emission of gas can be detected, as well as silicates and PAHs.

We have used CRIRES-VLT commissioning data to develop the methodology and the software tools to perform the spectro-astrometric analysis. The sources used in this exploratory program were the proto-PN IRAS 17516−2525 and the young PN SwSt 1. The observations of these sources, selected according to its evolutionary phase, were not specifically acquired to perform spectro-

astrometry, however, they were used to set the basis of the spectro-astrometric study. Both sources were not resolved in previous studies, thus, their morphological characteristics were unknown or barely resolved. Surprisingly, the preliminary results disclosed small-sized structures at mas scales. These results are the first to provide evidences of important structural components of this two sources.

The preliminary results have been able to detect the presence of small-sized structures $\sim130-230$ mas in size in the [Fe III] and Brγ near-IR lines of SwSt 1, as well as a small-sized structure ~12 mas in size in IRAS 17516$-$2525. These results suggest the presence of small bipolar lobes and an equatorial disk in SwSt 1, and small bipolar lobes arising from the innermost regions of IRAS 17516$-$2525. Tailored spectro-astrometric observations with its respective calibrations obtained at different PAs, as well as a proper model fitting are mandatory to confirm the presence of these structures.

The second phase of the implementation of the high-resolution spectro-astrometry technique consisted in the acquisition of near-IR long-slit CRIRES-VLT data devoted solely to perform this analysis. We have selected three representative sources of extreme axysimmetric morphology in PNe: the proto-PN AFGL 915 ("The Red Rectangle"), and two young PNe named M2-9 and Mz 3 ("The Butterfly Nebula" and "The Ant Nebula", respectively). This sample was carefully selected based on their previous high-resolution interferometric studies in which equatorial disks with different characteristics were found. In this thesis, we present the preliminary results of the spectro-astrometric analysis of the proto-PN AFGL 915.

The observation strategy implemented consist in the observation of several PAs and their respective complementary PA (antiparallel PA) to detect possible PSF artifacts induced by the detector. We have observed four PAs for AFGL 915, according to its symmetry axis, and their four antiparallel PAs (aPAs). These CRIRES-VLT observations were taken using the smallest slit aperture ($0.''2$) and using the AO system to guarantee the best spectral-resolution offered by this instrument. The observation of the CO fundamental band at $\lambda4.99\mu$m was selected to investigate the molecular gas and its possible relation with the CO Keplerian disk found at the equator of AFGL 915 using interferometric radio observations.

The position-velocity diagrams of the ^{12}C^{16}O line obtained with CRIRES-VLT resemble the spectra previously reported for this source. In addition, a double-peak line profile has been found for all the PAs and aPAs. The spectro-astrometric analysis has revealed an antisymmetric P-V signature, i.e., a Keplerian-like spectro-astrometric signature, whose extent presents variations from ~10 mas up to 60 mas. These results are consistent with the existence of an outer CO Keplerian disk. Our analysis may be indicative of the innermost CO Keplerian thick torus in slow rotation ($v \leq 5$ km s^{-1}) predicted by the interferometric studies. It is also in concordance with the detailed radiative transfer modelling previously performed for AFGL 915, in which the common envelope binary progenitor of this source gives rise to the massive and accreting toroidal innermost structure of ~100 mas.

Remarkably, the spectro-astrometric analysis based on CRIRES-VLT commissioning data has

been able to detect structures which are comparable in size to those resolved by MIDI-VLTI for Mz 3 and M 2-9 ($\sim$30 mas), reaching a radius of only 6 mas in the case of IRAS 17516-2525. Compared to MIDI-VLTI observations, CRIRES-VLT spectro-astrometry is more sensitive and it is not restricted by fixed baselines Detailed model fitting is mandatory to complete and fully assess the validity of the spectro-astrometrical signatures and the subsequent toroidal geometry revealed in our study for AFGL 915. Finally, we conclude that high-resolution spectro-astrometry offers a very suitable and promising technique for the search of small-sized disks and asymmetric components in the short transition to the PN phase.

Future work and perspectives

The results presented in this thesis have been obtained through the exploration of different high-resolution observational techniques and have complemented previous studies with valuable information in the near- and mid-IR. In regard to the imaging studies, we have enhanced structural components taking advantage of the high-resolution provided by VISIR-VLT and using deconvolution algorithms. However, other techniques that allows the reconstruction of images may be pursued in future studies focused in this complex transition to PNe.

As for the spectro-astrometric technique, we plan to complete the exploratory program with two young PNe, Mz 3 and M2-9, both representative of axisymmetric morphology. The data processing and analysis of these sources is in progress. Moreover, an adequate model fitting must be implemented to draw firm conclusions about the geometry and properties of the structures disclosed by this high-resolution technique. This model fitting will be implemented for the spectro-astrometric analysis of AFGL 915.

Encouraged by the results obtained so far, we aim to perform a survey using CRIRES-VLT and VISIR-VLT high-resolution spectro-astrometry in the search for the shaping agents of asymmetric PNe. Among these agents we expect to find binary progenitors, gaseous and dusty disks and/or torii, and jets.

.